

NACA RM L53G15

THIS DOCUMENT AND EACH AND EVERY  
PAGE HEREIN IS HEREBY RECLASSIFIED

FROM Conf TO Unclass

AS PER LETTER DATED 10/1/89

5-17-89 (U)

**NACA**

# RESEARCH MEMORANDUM

INVESTIGATION OF A RELATED SERIES OF  
TURBINE-BLADE PROFILES IN CASCADE

By James C. Dunavant and John R. Erwin

Langley Aeronautical Laboratory  
Langley Field, Va.

LANGLEY, TEXAS

CLASSIFIED DOCUMENT

This material contains information affecting the defense of the United States within the meaning of the espionage laws, Title 18, U.S.C., Sec. 793, 794, the transmission or revelation of which in any manner to an unauthorized person is prohibited by law.

**NATIONAL ADVISORY COMMITTEE  
FOR AERONAUTICS**

WASHINGTON

December 7, 1953

RM-L53G15

## NATIONAL ADVISORY COMMITTEE FOR AERONAUTICS

## RESEARCH MEMORANDUM

INVESTIGATION OF A RELATED SERIES OF  
TURBINE-BLADE PROFILES IN CASCADE

By James C. Dunavant and John R. Erwin

## SUMMARY

An application of airfoil design methods was used to design series of related turbine-blade profiles to satisfy the conditions of inlet flow angle and turning angle encountered in the usual range of turbine operation. A series of blade profiles applicable to most turbine blading requirements and a secondary series with particular reference to impulse conditions were designed. Five blade sections from these series ranging in mean-line turning angles from  $65^{\circ}$  to  $120^{\circ}$  were tested in low-speed cascade tunnels. From low-speed test results optimum blade angles of attack were selected at each test condition. The induced angle and the deviation angle of the flow were determined from the low-speed data. If these angles are known for the solidity and inlet angle of an application, the necessary camber is specified. A method of predicting high-speed pressure distributions from low-speed cascade test results is presented to extend the usefulness of the low-speed data. Sample high-speed tests of two of the five blade sections were made at Mach numbers up to the critical value. The results indicated satisfactory flow conditions in all of the blade passages tested.

## INTRODUCTION

Current methods of selecting turbine blade sections are based largely on empirical rules derived from experience with steam and gas turbines. In many applications satisfactory results have been obtained but no systematic method of designing suitable turbine blade sections has been published. In the case of closely spaced, highly cambered blades such as are encountered in turbine practice, the theoretical determination of the blade shapes is a difficult problem. A number of theoretical methods of varying degrees of approximation have appeared (for example, refs. 1 to 5).

For isolated airfoils it is possible by theoretical means to derive the pressure or velocity distribution about a given profile. On the basis of this theory a simple procedure has been developed (ref. 6) in which the theoretically determined basic thickness distribution and mean camber line are superimposed to determine the shape of the isolated profile corresponding to any desired pressure distribution.

The purpose of present investigation was to determine a related blade series that would have satisfactory aerodynamic performance throughout the ranges of inlet angle and turning angle encountered in current aircraft gas turbine practice. In this work, the same procedure used in the isolated-airfoil case of superimposing a thickness distribution on a mean camber line has been followed. By this method, an infinite number of blade profiles covering a wide range of cambers can be designed. The basic thickness distribution and the shape of the camber line for blade series were determined by cut-and-try procedures involving tests in a low-speed cascade tunnel and graphical flow studies with the aid of a wire-mesh plotting device (ref. 7).

In order to verify the performance of blade series developed by this method, five profiles designed for widely differing turbine operating conditions were tested in cascade tunnels. Two of the profiles were investigated at speeds up to the critical; however, choking flows were not obtained. From low-speed test results, optimum blade operating conditions were selected at each test condition. These data are used as a basis of a method which is presented for determining blading configuration for given design values of turning angle and inlet air angle.

#### SYMBOLS

A	flow area
c	blade chord
$C_p$	pressure coefficient, $\frac{P - P_m}{q_m}$
$C_{p0}$	pressure coefficient at low speeds
$C_{l_0}$	camber, expressed as design lift coefficient of isolated airfoil
$C_{D1}$	coefficient of total force parallel to mean velocity

$C_{w1}$	wake momentum difference coefficient
$F_c$	ratio of wake force coefficient to integrated total-pressure loss in wake
$M$	Mach number
$ML$	mean-line length
$p$	pressure
$P_R$	resultant pressure coefficient; difference between local upper- and lower-surface pressure coefficients
$q$	dynamic pressure, $\frac{1}{2}\rho V^2$
$s$	tangential spacing between blades
$S$	pressure coefficient, $\frac{p_0 - p}{q_1}$
$t$	blade thickness
$V$	velocity
$w$	wake width
$x$	chordwise distance from blade leading edge
$y$	perpendicular distance from blade chord line
$\alpha$	angle of attack; angle between entering flow direction and chord
$\beta$	air angle measured from axial (see fig. 1)
$\gamma$	ratio of specific heats
$\theta$	turning angle
$\rho$	density
$\sigma$	solidity, chord spacing ratio, $c/s$
$\Delta\theta_{\text{deviation}}$	angle between leaving flow direction and trailing-edge mean-line direction
$\Delta\theta_{\text{induced}}$	change in direction of the stagnation streamline at the leading edge

L/D	ratio of blade forces perpendicular to mean velocity and forces parallel to mean velocity
t/c	maximum thickness, percent chord
Subscripts:	
1	upstream of blade row, undisturbed stream
2	downstream of blade row
c	camber
m	mean passage
o	stagnation
t	thickness distribution
w	wake
cr	critical, condition at first attainment of sonic velocity on blade surface

## BLADE SECTION DESIGN

### General Design Criteria

The same procedure used in the isolated-airfoil case of superimposing a thickness distribution on a mean camber line has been used to obtain turbine blade profiles. The development procedures used for airfoil mean lines and thickness distributions are given in references 6 and 8, respectively. Blade series were designed to have satisfactory aerodynamic performance throughout the ranges of inlet angle and turning angle encountered in current aircraft gas turbine practice. For the purpose of designing blade series, flow conditions were divided into two groups requiring different blade sections to approach optimum performance. One group corresponds roughly to a reaction turbine condition in which the flow is accelerated through the cascade; blades designed particularly for this condition are classified as the primary series. The other group corresponds roughly to an impulse turbine condition for which the entering and leaving velocities are nearly equal; blades designed particularly for this condition are classified as the secondary series. Two dimensionally, the reaction condition occurs when the turning angle is greater than twice the inlet flow angle and the impulse condition occurs when the inlet and exit angles are equal.

Four criteria were believed to be desirable for turbine blade sections:

(a) Turbine blades should have low drag and no separation of the flow from the blade surface.

(b) Blade sections should have critical Mach numbers closely approaching the maximum values for the particular combination of inlet and turning angles to delay shock formation in the passage.

(c) The passage flow area should decrease from leading to trailing edge. The minimum area in the blade passage for a given blade spacing should be as large as possible without exceeding the leaving-flow area downstream of the passage.

(d) Whenever a penalty in over-all performance would not be incurred, a mean line and thickness distribution yielding nearly straight upper-surface trailing edges for all cambers is desirable since the leaving-flow direction for such sections is usually determined within close limits.

#### Primary Series

Figure 2 gives the theoretical maximum entering Mach number based on one-dimensional isentropic flow at choking flow for inlet angle and turning angle combinations. For blade sections having high reaction, and hence low maximum entering Mach number, highest critical Mach numbers will be obtained with blade sections having the aerodynamic loading concentrated in the low Mach number leading-edge regions rather than in the trailing-edge regions where the flow velocity is high. At high speeds, surface velocity distributions (for reaction conditions in particular) are modified by the effects of compressibility so that the loading in the trailing-edge region increases relative to the loading in the forward region. For these reasons, the flow can be turned quite rapidly in the forward region of the blade passage without exceeding the local velocity of sound. High aerodynamic loading of the blade mean line in this region is desirable to produce a given total lift or turning angle with the lowest maximum surface velocity and minimum losses. This also permits selection of a mean line and thickness distribution yielding nearly straight upper-surface trailing edges for all cambers.

With these considerations in view, blade sections of arbitrary mean line and thickness distribution for typical inlet- and turning-angle conditions were laid out and compared. Low-speed velocity distributions were obtained for the more promising sections by means of the wire-mesh plotting device (ref. 7) and the low-speed cascade tunnels. A method of extrapolating these low-speed velocity distributions to high-speed velocity distributions was developed in order that the high-speed pressure distributions

and critical Mach numbers of various sections could be compared. This method of extrapolating low-speed cascade tests results is given later. This process was used to select a single basic mean line and thickness-distribution shape for the primary series.

### Secondary Series

In the ideal impulse case, the critical entering Mach number would approach 1.0 for high solidities. However, at both low and high solidities practical blade thicknesses prevent the maximum critical Mach number from being closely approached because the average velocity through the passage necessarily remains high and large velocity differences across the passage are needed to produce the required lift. With a uniform average velocity through the passage, highest critical Mach numbers will be obtained by distributing the loading along the entire chord thus curving the mean line near the trailing edge. Therefore, the desire for straight trailing edges was compromised to distribute the loading more evenly along the chord and obtain higher critical Mach numbers.

A development similar to that of the primary series was carried out to obtain a secondary blade series more suitable for the particular requirements of impulse and low-turning blade operating conditions.

### Mean Lines

Figures 3 and 4 give ordinates of the basic mean-line shapes in terms of  $C_{l_0} = 1.0$ . The designation for these mean lines is given by the system used in reference 9. In the present development, the free-stream lift coefficient  $C_{l_0}$  is a meaningless parameter used only for convenience to relate the ordinates of figures 3 and 4 to the design value of turning angle and inlet angle. (See fig. 1.) The relation is

$$\theta_c = \theta + \Delta\theta_{\text{induced}} + \Delta\theta_{\text{deviation}} = \tan^{-1} C_{l_0} \left( \frac{dy_c}{dx_c} \right)_{0.5} - \tan^{-1} C_{l_0} \left( \frac{dy_c}{dx_c} \right)_{95}$$

where  $\left( \frac{dy_c}{dx_c} \right)_{0.5}$  and  $\left( \frac{dy_c}{dx_c} \right)_{95}$  are the slopes of the mean line at 0.5 percent chord and 95 percent chord for  $C_{l_0} = 1.0$ . All quantities in this relation are known except  $C_{l_0}$  and the values of  $\Delta\theta$ . A reasonable assumption for the values of  $\Delta\theta$  can be made on the basis of test results to be described later and thus  $C_{l_0}$  can be calculated by a simple

trial-and-error solution. The blade mean-line coordinates are obtained from the values of figures 3 or 4 by the following relation:

$$y_c = C_{l_o}(y_c)_{C_{l_o}=1.0}$$

### Thickness Distribution and Thickness

Thickness distribution coordinates for the blade series are tabulated in figures 3 and 4 for a 20-percent-chord maximum thickness and conversions to other maximum thicknesses are made by multiplying the ordinates of the uncambered airfoil section by the ratio of the desired thickness to the tabulated thickness. Position of the maximum thickness for the primary series is at 20 percent of the chord. For the secondary series the position of maximum thickness is shifted rearward to 40 percent of the chord near the position of the maximum blade passage area (where the flow has turned to axial). The value of maximum thickness for any particular blade configurations was selected so as to be consistent with the desires to have the area where choking will occur a maximum and to eliminate large flow area increases (diffusion) within the blade passages. Variation of the blade maximum thickness within these limits is deemed to have little effect upon the flow.

On ordinary airfoils where the camber is low, the thickness distribution is laid out on perpendiculars to the mean line above and below the mean line at stations distributed in proportion to the chord length. However, in the case of a highly cambered turbine blade section, the mean line may be as much as 30 percent greater in length than the chord line. In this case, the thickness is distributed along the curved mean line on perpendiculars stationed in proportion to the mean-line length. This method, illustrated in figure 5, was used on the blade sections of this paper.

The leading-edge radius varies as the square of the thickness ratio which is defined as  $t/ML$  in percent for the cambered airfoil. Therefore, the leading-edge radius for the cambered airfoil  $LER/ML$  is obtained from the leading-edge radius given in figures 3 or 4  $LER/c$  by the following relation:

$$\frac{LER}{ML} = \frac{LER}{c} \left( \frac{t/ML}{20} \right)^2$$

For the secondary series thickness distribution, the leading-edge radius determined from the thickness-distribution equations of reference 8 was unsuitable and an appropriate value (see fig. 4) was selected. The trailing-edge radius varies directly with thickness.



## TWO-DIMENSIONAL CASCADE TESTS OF BLADE SECTIONS

Limits for the range of turbine-blade operating conditions were determined by a study of many turbines used in aircraft engines. These limits are defined by the equation  $\theta = \beta_1 + 55^\circ \pm 20^\circ$  for values at  $\beta_1$  from  $0^\circ$  to  $65^\circ$ . Average values of solidity were chosen to be 1.5 and 1.8. The investigation was confined to these limits. Blade sections were tested over a range of angles of attack at several inlet angles to obtain the optimum angle of attack and turning. The optimum angle of attack was determined from the blade-surface pressure distribution at the leading edge and consideration of wake losses. The method of selection of this optimum value is discussed later.

## Blade-Section Models

The blade sections were cambered with mean lines having camber angles arbitrarily  $5^\circ$  greater than the desired turning angle. This overturning of the mean line was an allowance for the induced flow angle at the nose. The induced flow angle or turning of the flow ahead of the blade row in the direction opposite to the turning angle is caused by the circulation about the blade and is partially counteracted by the interference between blades. Previous cascade tests and flow plots had indicated  $5^\circ$  to be an average value of this angle. The  $60^\circ$  and  $75^\circ$  turning-angle sections were designed with maximum thicknesses of 10 percent of the chord and the  $90^\circ$  and  $105^\circ$  sections, with maximum thicknesses of 15 percent of the chord.

The blade section for the  $120^\circ$  turning condition was designed using the secondary series since turbine blades operating with turning angles as high as  $120^\circ$  necessarily would be impulse or very close to impulse. The mean-line turning of this section was  $120^\circ$ ; no allowance was made for induced flow angle since flow plots indicated this angle to be negligible at  $60^\circ$  inlet angle. Maximum thickness of this section was made 25 percent of the chord to prevent the passage from diverging excessively at the center. A small irregularity in the lower-surface shape occurred because of the extreme thickness of the section. This irregularity was removed by using a circular-arc fairing. These blade sections are shown in figure 6.

## Cascades Investigated

The following table presents the conditions at which tests were made:

Desired turning angle, $\theta$ , deg	Blade section camber angle, $\theta_c$ , deg	Solidity $\sigma = 1.5$ and inlet air angle $\beta_1$ of -				Solidity $\sigma = 1.8$ and inlet air angle $\beta_1$ of -											
		0°	15°	30°	45°	0°	10°	15°	20°	25°	30°	35°	40°	45°	60°		
60	65	a	a	a		a		a			a						
75	80	a	a	a		a	b	a,b	b	b	a,b	b					
90	95		a	a	a			a		b	a,b	b	b	a,b			
105	110			a	a						a			a			
120	120														a		

<sup>a</sup>Low-speed tests.

<sup>b</sup>High-speed tests.

Low-speed tests, identified by the letter a were conducted over a large range of angle of attack. High-speed tests, identified by the letter b were conducted at a single angle of attack or through a very narrow range of angle of attack.

### Low-Speed Tests

Description of equipment.- The test facilities used in this investigation were the Langley low-speed cascade tunnels described in reference 10. One major modification had been made in the larger cascade tunnel by reducing the test section width from 20 inches to 10 inches. All tests were made using solid walls in the test sections. Blade chords were 6 inches. The highest blade surface velocity attained in these tests was 206 feet per second.

Test Reynolds numbers.- As the pressure available from the blower was limited, the same dynamic pressure or Reynolds number could not be obtained at all test conditions due to the large variation in pressure drop across the blade row. Hence, the tests were run at near maximum output of the blower. Reynolds numbers based on the chord and upstream velocity showed wide variation with test conditions and in some cases were as low as 120,000 which is within the ordinary range of critical Reynolds numbers at which high losses occur in cascade. Low Reynolds numbers were obtained on blade configurations having large pressure drops across the blade row. Hence, the upstream velocity was the lowest velocity in the cascade and the flow velocity increased rapidly in the blade passage. The Reynolds number based on upstream velocity under such conditions is therefore of questionable value. By basing the Reynolds number on the average of the upstream and downstream velocities, a more suitable index is obtained. For this assumption, the range of Reynolds number for the low-speed tests was from 320,000 to 500,000.

Reduction of data.- Nondimensional force coefficients based on the upstream dynamic pressure  $q_1$  were calculated from pressure distribution, turning angle, and wake-survey data. The method used in calculating blade force coefficients is given in reference 11. Comparison of the force coefficient perpendicular to the chord calculated from turning-angle data and the force coefficient from the integrated pressure distribution was made as an accuracy check on the tests and these data agreed within 5 percent. The  $C_{W1}$  and  $C_{D1}$  values presented are, respectively, the wake momentum difference coefficient and the coefficient of the component of the total force on the blade parallel to the mean velocity. The ratio of forces perpendicular and parallel to the mean velocity  $L/D$  was calculated for blade comparison.

### High-Speed Tests

Description of equipment.- Tests were made of two of the blade sections in the 7-inch high-speed cascade tunnel at the Langley Laboratory. A diagrammatic sketch of the tunnel is shown in figure 7. The 40-inch-diameter duct is used as a settling chamber. Two screens are contained in this duct to insure uniform flow ahead of the tunnel inlet fairing. The tunnel upper and lower floors are attached to the inlet fairings. Both floors are adjustable in the vertical direction. The horizontal adjustment of the floor ends is made by telescoping the floor plates. The tunnel side walls consist of large circular assemblies which are rotated independently of the side-wall inlet fairing and the floors. Each side wall contains a protruding slot connected to a suction pump for removal of the boundary layer. The test section incorporating seven 4.2-inch-chord blades is located approximately  $7\frac{1}{2}$  inches downstream of the protruding slots. Boundary layer on the floors is bled off by discharging the flow between flexible floor extensions and the upper and lower blades to the atmosphere. Suction chambers connected to an exhaustor are installed to remove this flow when the upstream pressure is insufficient to discharge the flow to the atmosphere.

Due to limited blower pressure ratio, a diffuser was connected to the cascade downstream of the blades to increase the pressure drop available across the cascade. A straight aluminum plate was attached to the trailing edge of the lower blade and sealed at the blade trailing edge and at the walls. A second plate consisting of a 24-inch straight section followed by a diffuser section was connected to the trailing edge of the top blade. Linkages kept the straight sections parallel and provided a means of positioning the floors.

Total pressure and total temperature were measured upstream in the inlet duct. Static-pressure taps were located in the side walls between the protruding slot and the blade row. Flow angle upstream was measured

with a removable probe at three points on a line parallel to and just behind the slot. Downstream static-pressure taps were arranged in a row parallel to the blade row on the side wall and in rows parallel to the flow direction on the floors. A 17-tube total-pressure rake was inserted through a slot in the 24-inch straight section of the upper floor to measure the loss in total pressure caused by the center blade.

Test procedure.- The inlet air angle relative to the cascade of blades was set by rotating the circular side-wall plate containing the blade row. The angle of attack of the blades was set by means of an inclinometer.

Uniformity of upstream flow conditions was determined from three angular measurements with the removable yaw probe, upstream wall static pressure, and static pressures on the leading edges of the second, fourth, and sixth blades which contained special orifices for this purpose. Flow conditions upstream were altered by adjusting the floor positions and by controlling the boundary-layer bleed-off on the floors and walls. Downstream flow conditions were adjusted to obtain equal static pressure on the side walls and floors by changing the floor angle. The leaving-flow direction for a particular cascade configuration was assumed to be parallel to the floor direction when equal static pressures were obtained on the floors and walls. Insertion of the total-pressure rake into the flow caused changes in the blade-surface pressure distribution as well as in the upstream and downstream Mach numbers. Therefore, all test data, except for the total-pressure loss, were recorded with the rake removed. Loss measurements were made at identical blower speeds and tunnel settings even though rake interference caused differences in the static pressures on the walls and floors downstream.

Tests were made for a range of speeds including critical blade speed. Choking flows were not obtained due to limited blower pressure ratio. Average Reynolds numbers for the highest speeds calculated in the same manner as for the low-speed tests were between 1,200,000 and 1,500,000.

Reduction of data.- Normal-force coefficients were calculated from the integrated pressure distribution and from differences of the momentum and pressure upstream and downstream for each test. A comparison of these values made to determine testing accuracy showed a maximum discrepancy of 8 percent; generally, the discrepancy between values was much less than the maximum of 8 percent. An additional check was made to determine whether the boundary-layer build-up through the cascade was sufficient to prevent the tests from being considered two-dimensional. The two-dimensional mass flow through the blade passage at the center of the cascade was calculated from upstream conditions and compared with a similar mass flow calculated at the downstream rake position. This comparison showed the mass flow downstream to be between 3 percent less and 5 percent greater than the upstream flow. The wall boundary layer,

therefore, was small and the tests were concluded to be very nearly two-dimensional.

A wake force coefficient was calculated using the method given in reference 12 for determining drag-coefficient values. Additional assumptions were made in applying this method to a cascade in that the downstream conditions were assumed to be free-stream conditions and the static pressure at the rake was equal to the static pressure far downstream. Wake force coefficients were calculated by this method; however, values presented are based on the dynamic pressure upstream of the cascade; hence

$$C_{W1} = F_c \int_0^w \frac{p_{o1} - p_{o2}}{q_{1c}} dw$$

## DISCUSSION

### Turning Angles

Results of the low-speed tests are shown in figures 8 to 30. The turning angle increases in almost direct proportion to the angle of attack. In figure 11(f), however, the measured turning angle does not show a comparable increase for an increase in the angle of attack at leaving-flow angles near  $74^\circ$ . With high exit flow angles, the straight portion of the convex surface no longer forms a guided region at the trailing edge. The downstream shift of the straight trailing-edge portion relative to the adjacent blade, especially in the lower solidity tests, is evidently the cause for the turning-angle variation. From this, it may be expected that separation of the flow from the trailing surface will occur for leaving-flow angles greater than  $74^\circ$  but leaving-flow angles in the neighborhood of  $74^\circ$  may be considered the normal design limit. A nonlinear variation of  $\theta$  with  $\alpha$  is observed in figure 18(f) at low angles of attack. In this case, the lower surface velocity peak near the leading edge of the very highly cambered airfoil and the following increasing pressure gradient may have produced laminar separation over the concave surface since the wake forces show some increase at this condition. The turning angle decreases slightly at this condition because of the secondary boundary-layer flow along the wall from the high-pressure lower surface to low-pressure upper surface. The resulting thickened boundary layer on the upper surface results in a greater flow deviation from the mean-line direction.

The high-speed test results presented in figures 31 to 49 showed no significant change in turning angle with Mach number. Choking flows were not obtained so the changes in turning angle to be expected at supercritical

pressure ratios (ref. 13) were not investigated. Turning angles measured for the high-speed tests varied with angle of attack in a manner similar to the low-speed tests. Measured turning angles for the Mach number range tested were consistently between  $1^\circ$  and  $2^\circ$  greater than corresponding low-speed test measurements. Since no variation of turning angle with Mach number was observed, this discrepancy is not attributed to effects of varying Reynolds numbers. In the high-speed tunnel, the leaving flow is assumed to be parallel to the downstream floor plates. The upper-floor boundary layer is formed along a blade lower surface since the floor is a continuation of a blade lower surface just as the lower floor is a continuation of the upper surface of a blade. Hence, because of the different boundary layers, the flow between the downstream floors is not necessarily exactly parallel to the floors as was assumed in obtaining the turning angles presented. For subcritical pressure ratios the leaving-flow direction for turbine blading incorporating guidance is determined within close limits by the trailing-edge direction.

For convenience in determining the effect of blade shapes and inlet air angle on turning angle from low-speed test results, the deviation or leaving-flow angle relative to the mean-line direction at the 95-percent-chord station is plotted in figure 50 against blade camber angle and in figure 51 against leaving-flow angle. These figures present the variation of the deviation angle for a particular angle of attack selected as an optimum design condition. The method of selecting design angles is discussed in a subsequent section. In figures 50(a) and 51(a), the high value of deviation angle for the  $\theta_c = 110^\circ$  blade section at an inlet angle of  $45^\circ$  is believed to be a result of laminar separation on the lower surface. This point, therefore, is excluded in analyzing the deviation-angle variation. The deviation angle for this blade section is assumed to vary in a manner similar to that shown in figures 50(b) and 51(b) for the same blade section at a higher solidity. General trends indicated by figures 50 and 51 are increasing deviation angle with increasing inlet air angle for constant camber. The deviation angle increased with increasing blade camber for constant air inlet angle or constant exit flow angle. The low values of deviation angle indicate that the straight trailing edges satisfactorily guided the leaving flow.

#### Wake Losses

Low speed.- Trends of the variation of wake losses with changing blade conditions are indicated in the low-speed test results shown in figures 8 to 30. Wake measurements are presented as coefficients determined from losses based on the upstream dynamic pressure. Blade-section efficiency is indicated by the  $L/D$  values plotted. At high reaction conditions the large difference between the entering velocity on which the coefficients are based and the leaving velocity causes high drag and

lift coefficient values but the  $L/D$  value is relatively unaffected. Generally,  $L/D$  ratio increased with increasing camber for a constant inlet flow angle. The lower solidity tests produced higher  $L/D$  ratios since increased lift was obtained with only slightly higher drag values.

High speed.- Values of  $C_{W1}$  measured in the high-speed tunnel at very low speed agree with values measured in the low-speed tunnels within the accuracy of the testing apparatus. Wake momentum difference coefficients increased slightly with increasing Mach number up to critical speed. This, however, is not an indication of any deterioration of the flow because a wake momentum difference coefficient based on downstream rather than upstream dynamic pressure shows no significant change in value within the Mach number range investigated.

Wake losses do not indicate any strong effects of separation at speeds up to the critical speeds and from the standpoint of wake losses the blade series are considered satisfactory.

#### Surface Pressure Distributions

Low-speed tests.- The primary blade series has high curvature near the leading edge with nearly straight trailing edges. In tests of the primary blade shapes, the velocities along the straight, unloaded trailing-edge portions were only slightly greater than the leaving-flow velocities indicated by the dash at 100-percent chord on pressure distributions. For the operating condition of large velocity increases across the blade row, the trailing-edge surface velocity, although only slightly greater than the leaving-flow velocity, was the maximum blade surface velocity. Typical examples of this condition are shown in figures 22, 25, and 28. For operating conditions producing little or no velocity increase across the blade row, the highly loaded leading edge and the relatively high entering velocity caused upper-surface velocities near the leading edge to be far greater than the leaving velocity as seen in figures 10, 13, and 16.

In the low-speed tests, detrimental effects due to high velocities near the upper surface leading edge were not evident. No separation of the flow from the upper surface was detected in these tests for normal operating conditions. On the lower surface high velocities occurred near the leading edge of highly cambered blades at low angles of attack. The steep positive pressure gradients following the velocity peaks sometimes caused laminar separation of the flow from the lower surface. For example, the dashed pressure distribution of figure 29(a) shows the resulting separated region just behind the nose on the lower surface. This separation resulted in a reverse flow region in the blade passage near the lower surface. Secondary boundary-layer flow along the wall resulted in a thickened boundary layer on the blade upper surface and, hence, a lower turning angle. Increasing the stream turbulence by inserting a 1/2-inch mesh

screen upstream of the blade row greatly reduced the extent of the separated region. This method was used to obtain the tests shown in figures 17, 18, 29, and 30. The constant-pressure region typical of laminar separation is not detectable on these pressure-distribution plots nor was any flow reversal indicated in the surveys made in the blade passage with a small tuft. However, in the low angle-of-attack tests of figures 18 and 30, the drag values are higher than at higher turning angles.

Pressure distributions from tests of the highly cambered secondary blade section are shown in figure 30. More uniform distribution of the aerodynamic loading (fig. 5) along the chord resulted in a blade shape having a curved trailing edge and nearly uniform pressure along the upper surface at test conditions producing negligible velocity increase across the blade row. More nearly ideal surface velocities than for the reaction blade series are obtained for this particular condition in that higher entering Mach numbers are expected before sonic velocity occurs on the blade surface. Also, higher flows would be obtainable before choking occurs since the curved trailing edge allows larger minimum areas for equal leaving-flow angles.

High-speed tests.— The blade-surface pressure distributions measured during the high-speed tests were similar in shape to the low-speed distributions although the pressure coefficient  $S$  increased with increasing speed, especially for the higher velocity regions. Hence, for reaction conditions the loading shifted rearward with increasing Mach number. Examples of this may be seen in figures 33, 34, 42, and 43. Radical changes in the pressure distribution occurred as blade surface speeds exceeded sonic speed and shocks formed in the passage. In figure 46(b), the effect of a shock on the pressure distribution can be seen as the pressure coefficient decreases abruptly in the region near the 20-percent-chord station. At most test conditions, sonic velocity was exceeded only slightly due to the limited blower pressure ratio.

As in the low-speed tests, separation was not observed for these blade series within the range of conditions in which the blades would be expected to operate. In this respect, therefore, the blade series are considered satisfactory.

#### Critical Mach Numbers

Entering Mach numbers are limited by choking of the blade passage; however, losses in blading can become significant before choking occurs. Limiting entering Mach numbers based on losses cannot be established from the high-speed tests since the test velocities were limited by the available air supply. Entering Mach numbers in excess of critical were obtained without excessive wake forces in high-speed tests such as those of figures 38, 40, and 42. These tests did not cover the range of



discharge Mach numbers of sonic and above, and blade operating characteristics at these speeds are unknown.

Representative test values of critical speeds are given in figure 52. Critical Mach numbers calculated by the method of applying compressibility effects to low-speed pressure distributions given in a subsequent section are shown in figure 52 to differ little from test values. Critical Mach numbers approach the theoretical maximum Mach number for the cascade combination when operating in a reaction condition. However, as impulse conditions are approached, maximum Mach number increases more rapidly than the critical Mach number. Theoretically, at an impulse condition the flow could be diffused and turned with infinitely thin blade sections to yield critical Mach numbers equal to 1.0. Practically, however, the amount of diffusion possible is limited and the blade thickness must be necessarily large; hence, critical Mach numbers at impulse conditions are much less than the maximum. The critical Mach number for a secondary-series blade designed specifically for impulse conditions with uniform loading along the chord is higher than that of the primary blade section, however, as can be seen in figure 52. In order to estimate the critical speed of the secondary blade, compressibility effects were applied to the pressure distribution obtained from the wire-mesh flow plot of this blade section.

Critical Mach numbers near maximum were obtained at reaction conditions. However, for impulse conditions blade sections with straight trailing edges have lower critical Mach numbers than blade sections with camber in the trailing-edge region. Therefore, with respect to the critical Mach number the blade series also may be considered satisfactory.

#### Application of Compressibility Corrections to Low-Speed Tests

Data can be obtained from low-speed cascade tests with a minimum of equipment, time, and computation. The data are of value for direct use and for comparing different blade sections intended to accomplish a given task. In most turbomachines, however, the blades operate at high speeds so the effects resulting from the compressibility of the flow must be considered. This is particularly true of aircraft-engine turbine blading, for the velocities leaving the blades are usually near sonic. A method is required, therefore, for correcting low-speed cascade pressure distributions for the first-order effects of compressibility in order to estimate the high-speed pressure distribution. No rigorous theoretical method of accomplishing this correction is available.

The semi-empirical procedure about to be described is derived from an approximate method used to estimate compressibility effects for isolated airfoils. The Prandtl-Glauert theory for thin airfoils in a free stream leads to a formula relating the pressure coefficient  $C_p$  at a stream Mach number  $M_1$  to the incompressible pressure coefficient  $C_{p0}$

$$C_p = \frac{C_{p0}}{\sqrt{1 - M_1^2}} \quad (1)$$

In the present method, it is arbitrarily assumed that this formula can be used to compute the compressible pressure coefficient at a station in the turbine blade cascade from the low-speed value at that station by replacing  $M_1$  with a mean value taken across the passage at the station in question. The mean stream Mach number  $M_m$  is determined from known values of the passage area  $A_m$ , the entering stream tube area  $A_1$ , and the entering Mach number  $M_1$  from the one-dimensional isentropic flow relationship

$$\left(\frac{A_m}{A_1}\right)^2 = \frac{M_1^2 \left(1 + \frac{\gamma-1}{2} M_m^2\right)^{\frac{\gamma+1}{\gamma-1}}}{M_m^2 \left(1 + \frac{\gamma-1}{2} M_1^2\right)} \quad (2)$$

The pressure coefficients  $C_p$  and  $C_{p0}$  are also based on mean passage condition obtained from the areas  $A_1$  and  $A_m$ .

As the potential flow in the two-dimensional passage is perpendicular to an equipotential line across the passage at any station, the effective flow area  $A_m$  will be determined by the length of this line. Such a line may be approximated with fair accuracy by a circular arc which is perpendicular to both passage boundaries. The correctness of this assumption of area was checked on flow plots made with the wire-mesh-flow plotting device described in reference 7. No exact construction can be given for these circular arcs since the position and hence the slope of one end of the arc is not known. To facilitate the determination of a suitable arc, a transparent template consisting of a series of arcs of varying radii was made. This method is illustrated in figure 53. Equal arc lengths on the template were marked so that passage width could be read directly on the template after selecting the proper arc. A planchette, a small square of transparent plastic having two lines at right angles and a scale of inches inscribed on it facilitates selecting the appropriate arc and reading the corresponding arc length.

Typical results of this method of extrapolation of low-speed data are compared in figure 54 with the equivalent high-speed pressure distribution obtained in cascade tests. Good agreement of pressures is noted in this case for the entire blade surface. Critical entering Mach numbers obtained by means of this extrapolation show good agreement with test results as shown in figure 52. At Mach numbers greater than critical the method cannot be used rearward of the shock location. In cases where the flow pattern is altered by viscous effects at high speeds, the method will obviously not give correct predictions.

### Selection of Design Camber

The results of the low-speed tests at constant inlet air angle permit the selection of design blade operating conditions. Interpolation of results between blade shapes and test conditions is made possible by the geometric similarity of the mean camber lines. Thus, by determining the optimum angle of attack at each inlet air angle and solidity the blade camber is specified for a desired turning angle at any inlet air angle. To obtain design blade cambers for other conditions, an interpolation between both inlet air angle and turning-angle conditions can be made.

The upper-surface velocity in the trailing-edge region has been observed to be consistently slightly higher than the leaving-flow velocity. Since the leaving-flow velocity will be a fixed value for a given design, then the surface velocity in the trailing-edge region is also fixed leaving only the flow in the leading-edge region a variable. Hence, in selecting the optimum angle of attack at each test condition of air inlet angle and solidity, the criterion used was the flow at the leading edge of the airfoil. The effect of circulation around the blade causes a turning of the airstream in the direction of the blade lift just ahead of the leading edge; this change in direction of the stagnation streamline at the leading edge is referred to as "induced flow angle"  $\Delta\theta_{\text{induced}}$ .

The value of the induced angle was obtained experimentally for the blade shapes tested in the low-speed cascade tunnel. Measurements were made by using closely spaced surface pressure orifices near the blade leading edge. In effect, the blade was rotated until a pressure equal to full total pressure was obtained at the orifice located at the end of the mean line and the orifices on either side indicated equal pressure drop. The absolute accuracy of such a measurement as this is low and is estimated to be only within  $\pm 3^\circ$  since it depends on the accurate positioning of the pressure orifices.

The resulting induced angle values are shown plotted in figures 55 and 56. The most apparent trend was the decrease of induced angle with increasing inlet angle. The variation with solidity was of smaller magnitude and almost constant over the entire test range. The induced angle is largest at low inlet air angles where the interference of other airfoils in the cascades is least. For the purposes of camber selection a mean value of the induced angle is presented as a function of only the inlet air angle and the solidity as shown in figures 55 and 56. By overcambering blade sections by the value of the induced angle, the effects of the induced flow are taken into account. Thus, total blade camber or mean-line turning angle will be the sum of the turning angle, induced angle, and the angle of flow deviation from the mean line exiting angle interpolated from figure 50 or 51. Design angle of attack of the section will

be the mean-line slope:  $\tan^{-1} C_{l_0} \left( \frac{dy_c}{dx} \right) - \Delta\theta_{\text{induced}}$   
 $\alpha = 0.5, C_{l_0} = 1.0$


## SUMMARY OF RESULTS

The investigation conducted to obtain related turbine blade profiles for conditions of inlet-flow angle and turning angle encountered in the usual range of aircraft gas turbine operation yielded two series of airfoil-type blades. A primary series was developed for reaction conditions and a secondary series was selected to produce more nearly optimum results at impulse and low-turning conditions.

Relating blade sections by this design procedure allows interpolation of blade test results and design of blade sections with greater certainty of flow conditions within the blade passage. A simple design procedure is given whereby blade profiles from these series can be readily obtained for any design condition in the range of current interest. Satisfactory blade performance is indicated by the cascade tests of five blade sections from these series for widely varying conditions which produced the following results:

1. Separation was not observed for the blade series within the range of conditions in which the blades would be expected to operate.
2. Guiding the flow by means of straight trailing-edge portions is effective in maintaining a fixed turning angle up to critical speed.
3. Near-maximum critical Mach numbers were obtained at reaction conditions. However, for low reaction conditions blade sections with straight trailing edges have lower critical Mach numbers than blades with camber in the trailing-edge region.
4. A semi-empirical method for extrapolating low-speed pressure distributions was found to produce results which were in good agreement with high Mach number tests. The method cannot be used in cases where the flow pattern is altered by viscous effects or shocks.

Langley Aeronautical Laboratory,  
National Advisory Committee for Aeronautics,  
Langley Field, Va., July 14, 1953.



## REFERENCES

1. Mutterperl, William: A Solution of the Direct and Inverse Problems for Arbitrary Cascades of Airfoils. NACA WR L-81, 1944. (Formerly NACA ARR L4K22b.)
2. Goldstein, Arthur W., and Jerison, Meyer: Isolated and Cascade Airfoils With Prescribed Velocity Distribution. NACA Rep. 869, 1947.
3. Weinig, F.: Flow Patterns of a Compressible Gas Through Turbine Cascades When Shock Waves Are Avoided. Tech. Rep. No. F-TR-2141-ND, Air Materiel Command, U.S. Air Force, May 1947.
4. Alpert, Sumner: Design Method for Two-Dimensional Channels for Compressible Flow With Application to High-Solidity Cascades. NACA TN 1931, 1949.
5. Costello, George R.: Method of Designing Cascade Blades With Prescribed Velocity Distributions in Compressible Potential Flows. NACA Rep. 978, 1950.
6. Abbott, Ira H., Von Doenhoff, Albert E., and Stivers, Louis S., Jr.: Summary of Airfoil Data. NACA Rep. 824, 1945. (Supersedes NACA WR L-560.)
7. Westphal, Willard R., and Dunavant, James C.: Application of the Wire-Mesh Plotting Device to Incompressible Cascade Flows. NACA TN 2095, 1950.
8. Stack, John, and Von Doenhoff, Albert E.: Tests of 16 Related Airfoils at High Speeds. NACA Rep. 492, 1934.
9. Erwin, John R., and Yacobi, Laura A.: Method of Estimating the Incompressible-Flow Pressure Distribution of Compressor Blade Sections at Design Angle of Attack. NACA RM L53F17, 1953.
10. Erwin, John R., and Emery, James C.: Effect of Tunnel Configuration and Testing Technique on Cascade Performance. NACA Rep. 1016, 1951. (Supersedes NACA TN 2028.)
11. Herrig, L., Joseph, Emery, James C., and Erwin, John R.: Systematic Two-Dimensional Cascade Tests of NACA 65-Series Compressor Blades at Low Speeds. NACA RM L51G31, 1951.
12. Heaslet, Max A.: Theoretical Investigation of Methods for Computing Drag From Wake Surveys at High Subsonic Speeds. NACA WR W-1, 1945. (Formerly NACA ARR 5C21.)

13. Hauser, Cavour H., Plohr, Henry W., and Sonder, Gerhard: Study of Flow Conditions and Deflection Angle at Exit of Two-Dimensional Cascade of Turbine Rotor Blades at Critical and Supercritical Pressure Ratios. NACA RM E9K25, 1950.

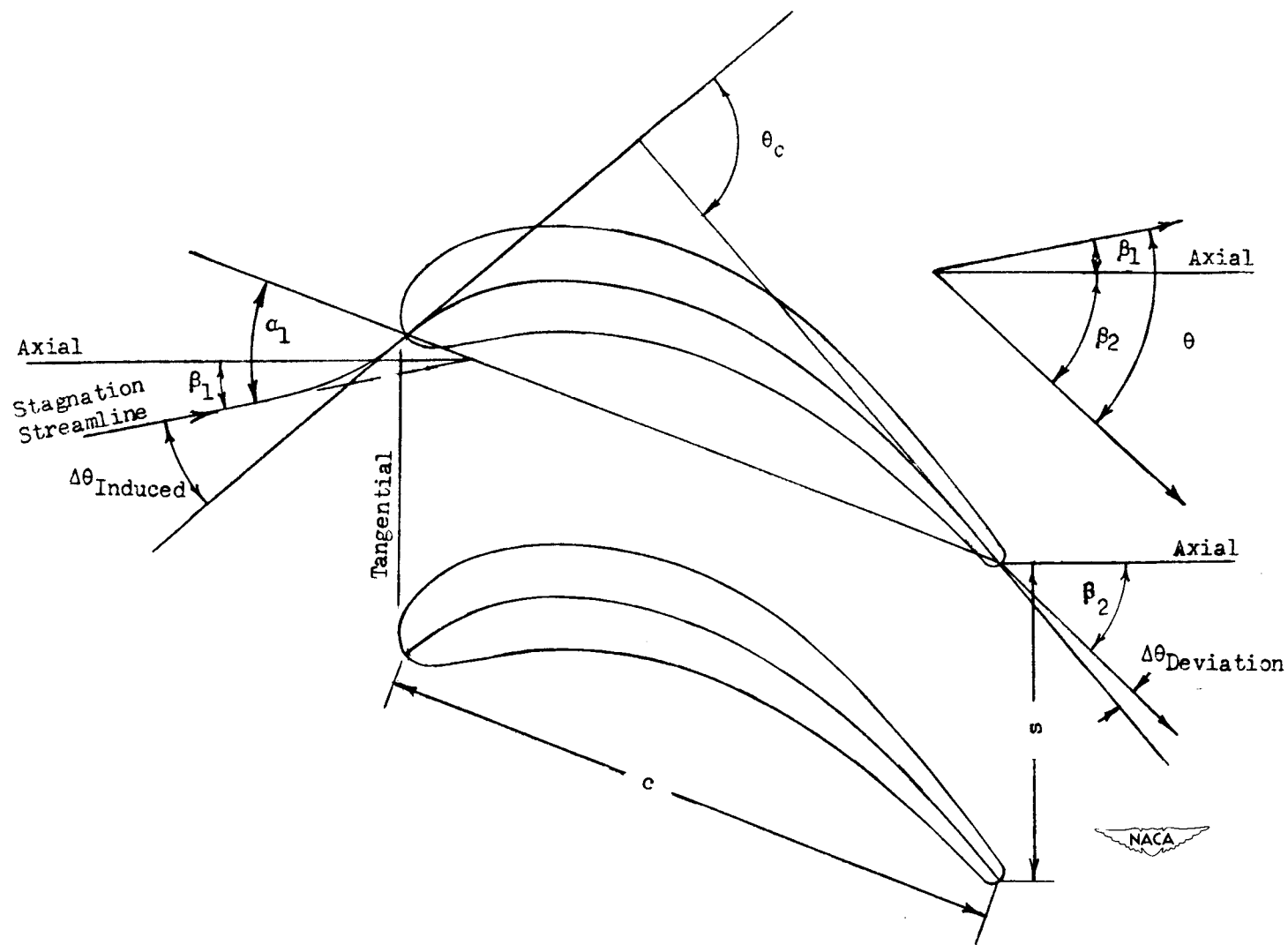


Figure 1.- Turbine cascade notation.

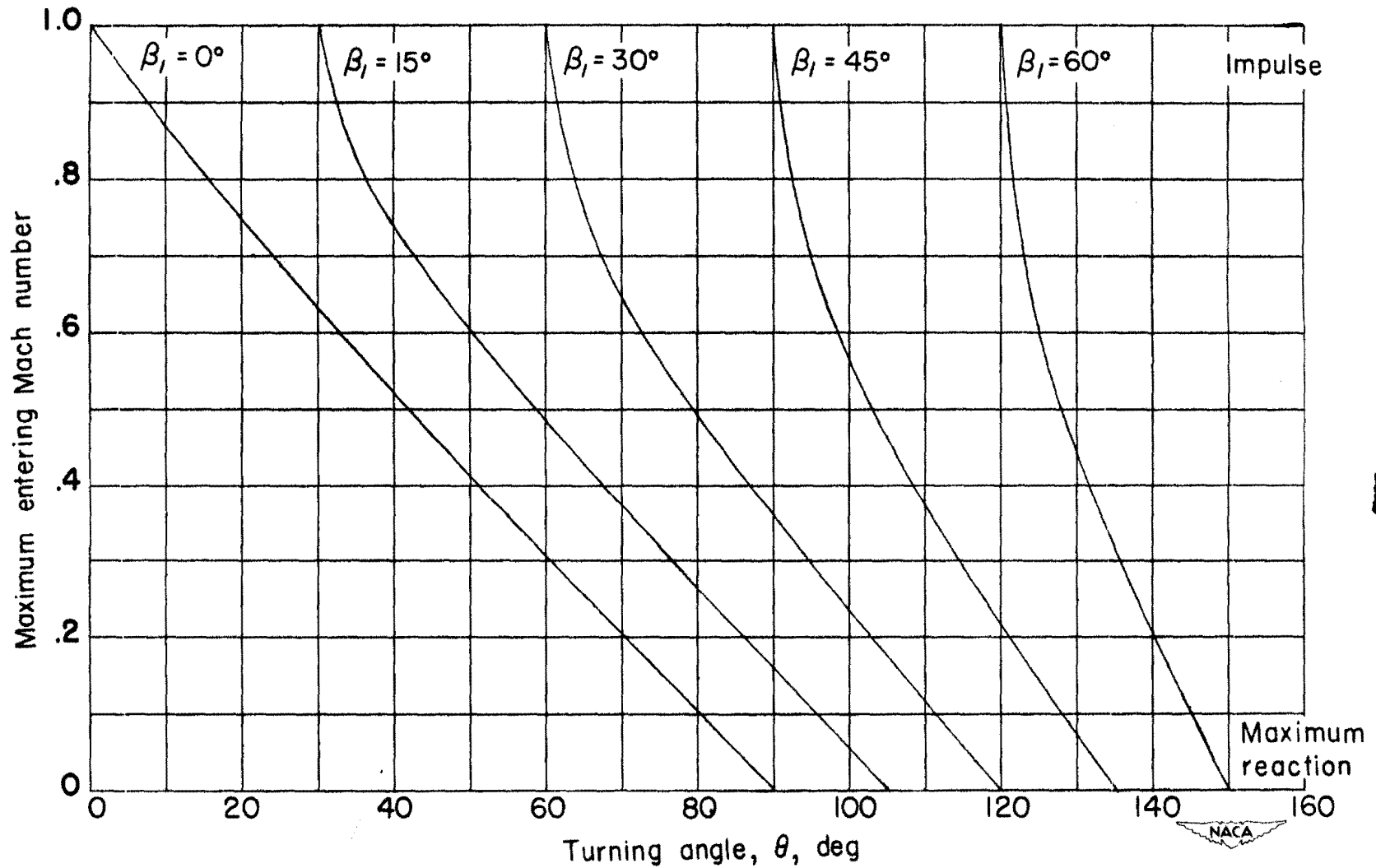
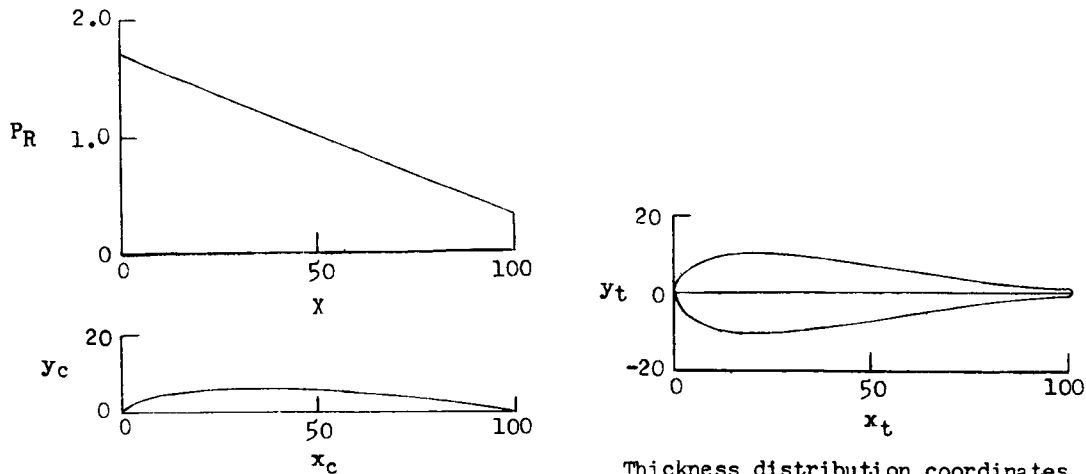


Figure 2.- Maximum entering Mach number for cascade combinations of inlet angle and turning angle.



A<sub>3</sub>K<sub>7</sub> mean-line coordinatesfor  $C_{l_0} = 1.0$ 

$x_c$	$y_c$
0	0
0.5	0.397
1.25	0.836
2.5	1.428
5.0	2.359
10	3.689
15	4.597
20	5.217
25	5.623
30	5.852
35	5.936
40	5.897
45	5.753
50	5.516
55	5.200
60	4.814
65	4.367
70	3.870
75	3.328
80	2.746
85	2.133
90	1.485
95	0.801
100	0

$$\left(\frac{dy_c}{dx_c}\right)_{0.5} = 0.6574$$

$$\left(\frac{dy_c}{dx_c}\right)_{95} = -0.1602$$

Thickness distribution coordinates  
 $t/c = 20$  percent(Stations and ordinates given  
in percent of chord)

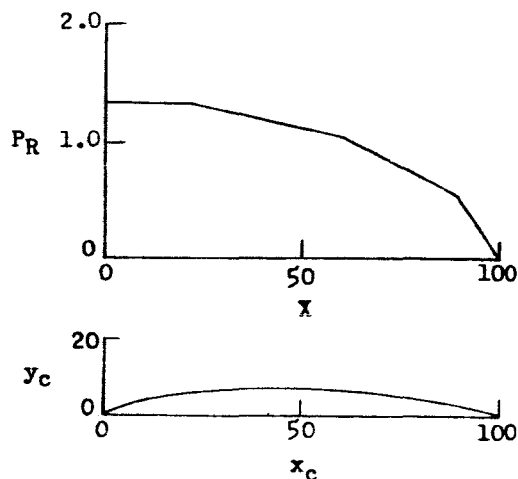
$x_t$	$y_t$
0	0
1.25	3.469
2.5	4.972
5.0	6.918
10	9.007
15	9.827
20	10.000
25	9.899
30	9.613
35	9.106
40	8.594
45	7.913
50	7.152
55	6.339
60	5.500
65	4.661
70	3.848
75	3.087
80	2.406
85	1.830
90	1.387
95	1.101
100	0

$$LER/c = 4.407$$

$$TER/c = 1.000$$



Figure 3.- A<sub>3</sub>K<sub>7</sub> mean line, and thickness distribution, and coordinates for primary turbine-blade series. For mean-line designation system, see reference 9.

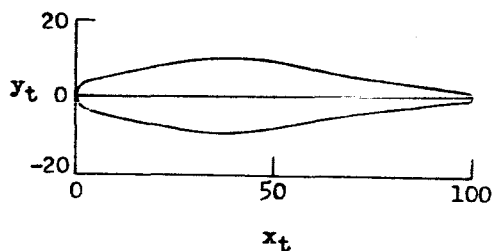


$B_1E_1I_1$  mean-line coordinates  
for  $C_{lp} = 1.0$

$x_c$	$y_c$
0	0
0.5	0.336
1.25	0.718
2.5	1.253
5.0	2.128
10	3.480
15	4.506
20	5.291
25	5.862
30	6.261
35	6.514
40	6.642
45	6.652
50	6.551
55	6.342
60	6.016
65	5.551
70	4.983
75	4.332
80	3.680
85	2.824
90	1.953
95	0.948
100	0

$$\left(\frac{dy_c}{dx_c}\right)_{0.5} = 0.5657$$

$$\left(\frac{dy_c}{dx_c}\right)_{95} = -0.2017$$



Thickness distribution coordinates  
 $t/c = 20$  percent

(Stations and ordinates given  
in percent of chord)

$x_t$	$y_t$
0	0
1.25	2.583
2.5	3.282
5.0	4.041
10	5.007
15	5.952
20	6.995
25	8.063
30	9.025
35	9.727
40	10.000
45	9.725
50	9.009
55	8.016
60	6.908
65	5.848
70	5.000
75	4.312
80	3.624
85	2.936
90	2.248
95	1.560
100	0

$$LER/c = 3.300$$

$$TER/c = 1.000$$



Figure 4.-  $B_1E_1I_1$  mean line, and thickness distribution, and coordinates for secondary turbine-blade series. For mean-line designation system, see reference 9.

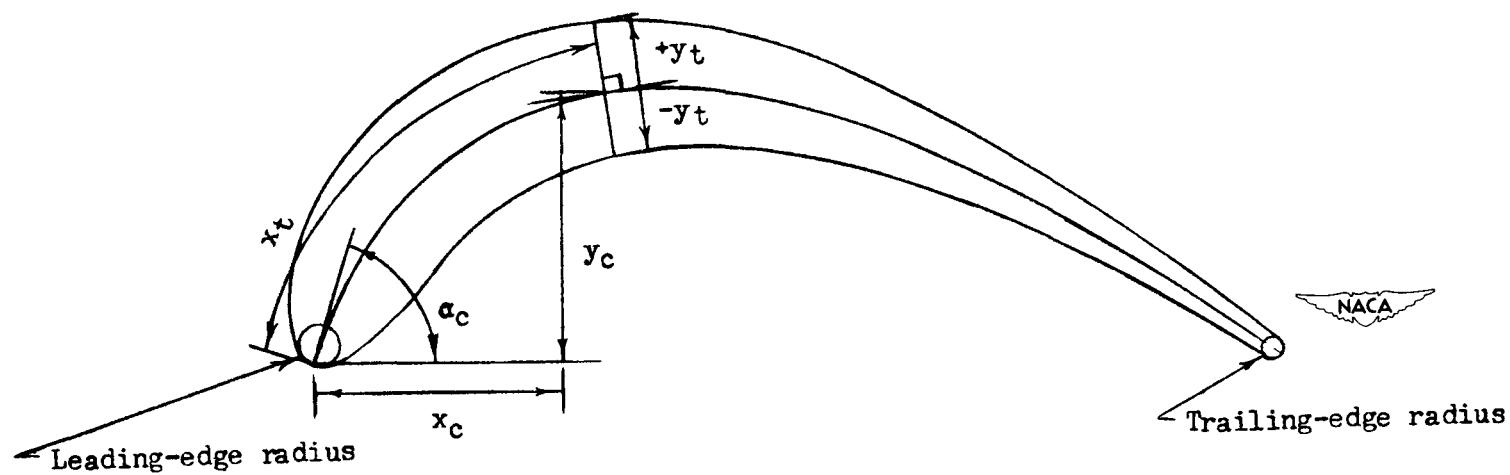
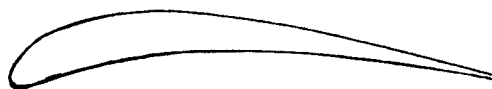


Figure 5.- Method of blade construction.



Primary turbine blade section,  $\theta_c = 65^\circ$ ,  $t/c = 10$  percent



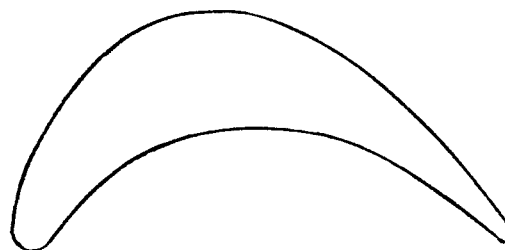
Primary turbine blade section,  $\theta_c = 80^\circ$ ,  $t/c = 10$  percent



Primary turbine blade section,  $\theta_c = 95^\circ$ ,  $t/c = 15$  percent



Primary turbine blade section,  $\theta_c = 110^\circ$ ,  $t/c = 15$  percent



Secondary turbine blade section,  $\theta_c = 120^\circ$ ,  $t/c = 25$  percent

Figure 6.- Profiles of the five blade sections tested.

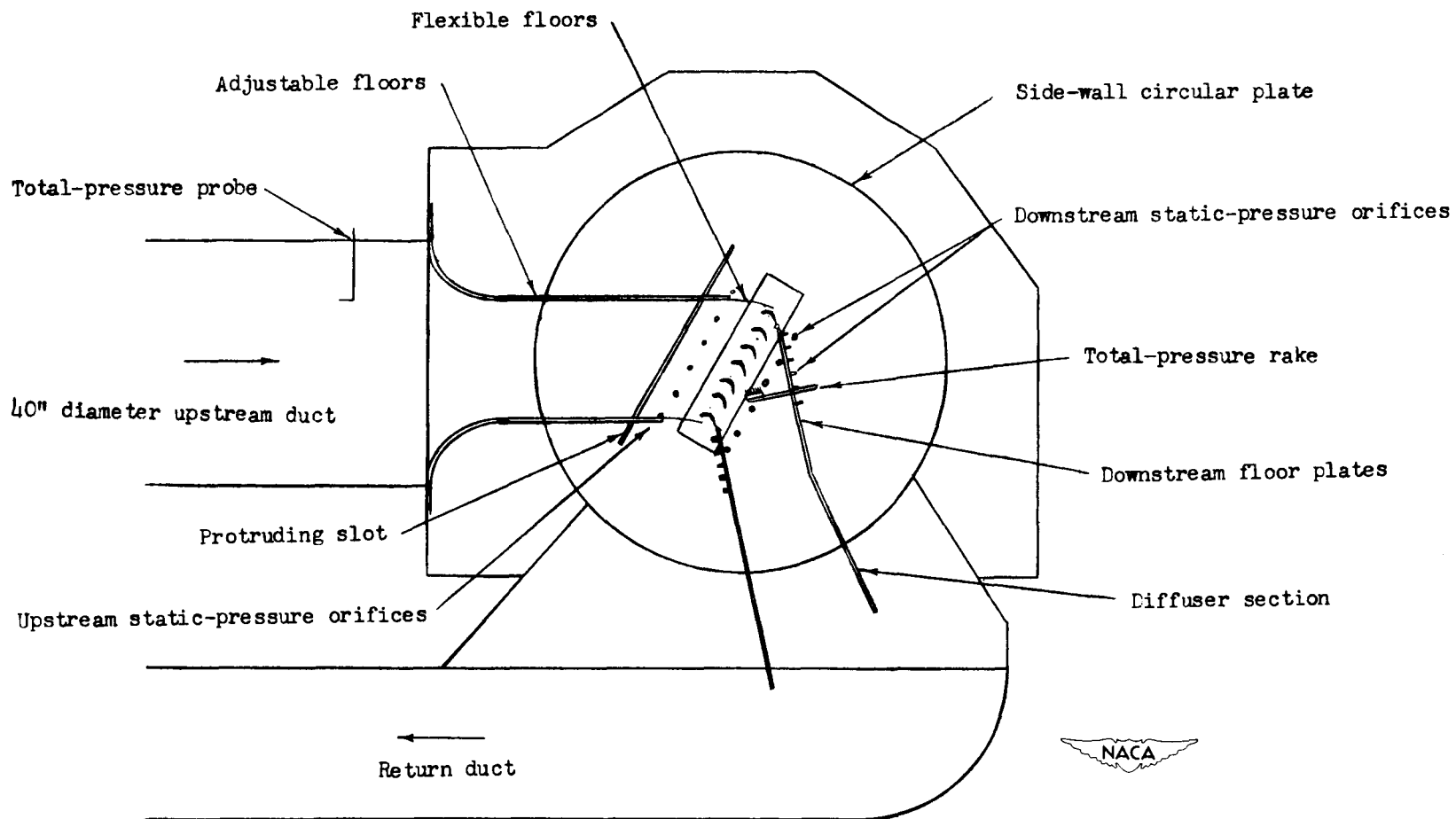


Figure 7.- Cross-sectional view through high-speed cascade tunnel.

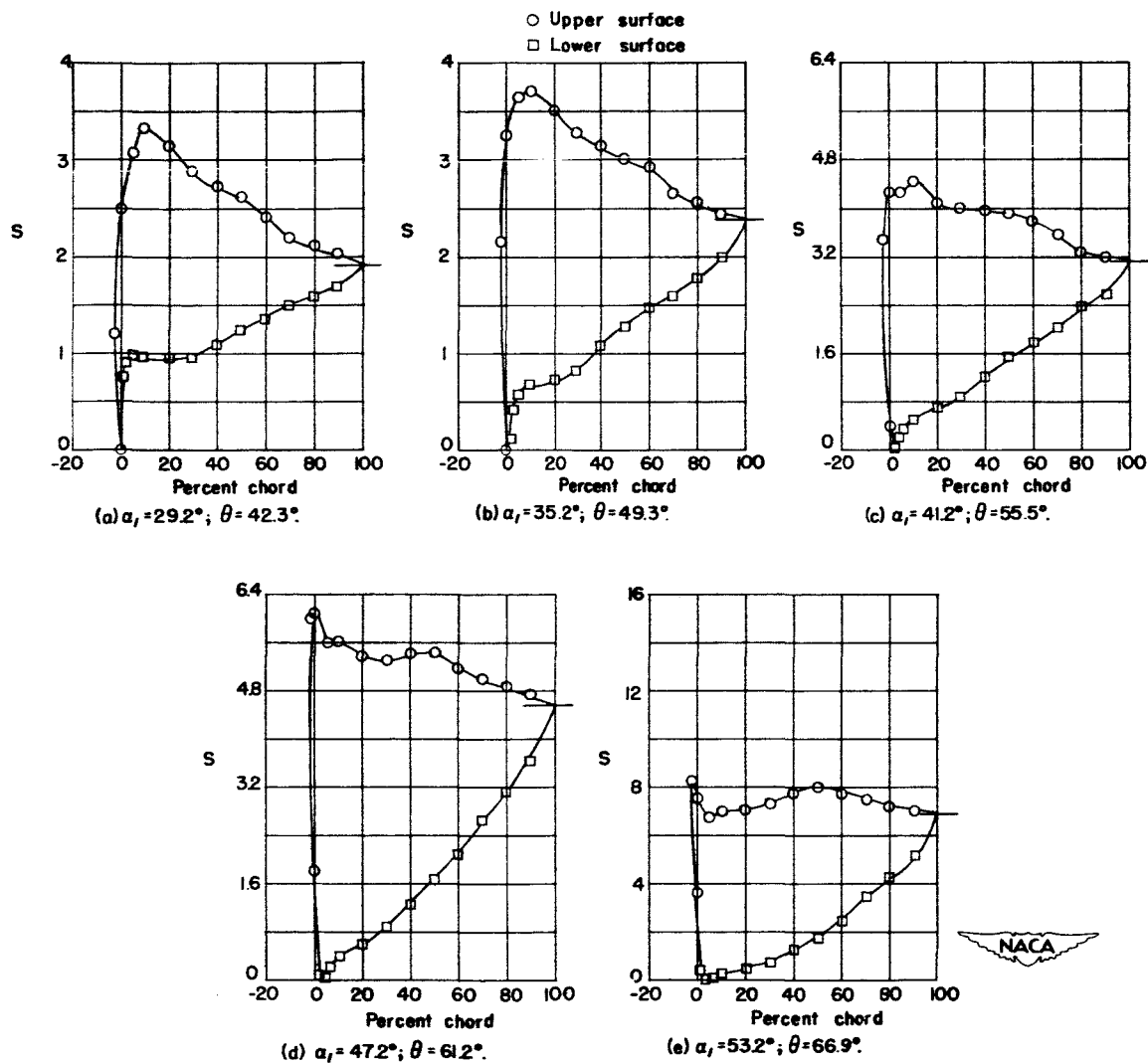
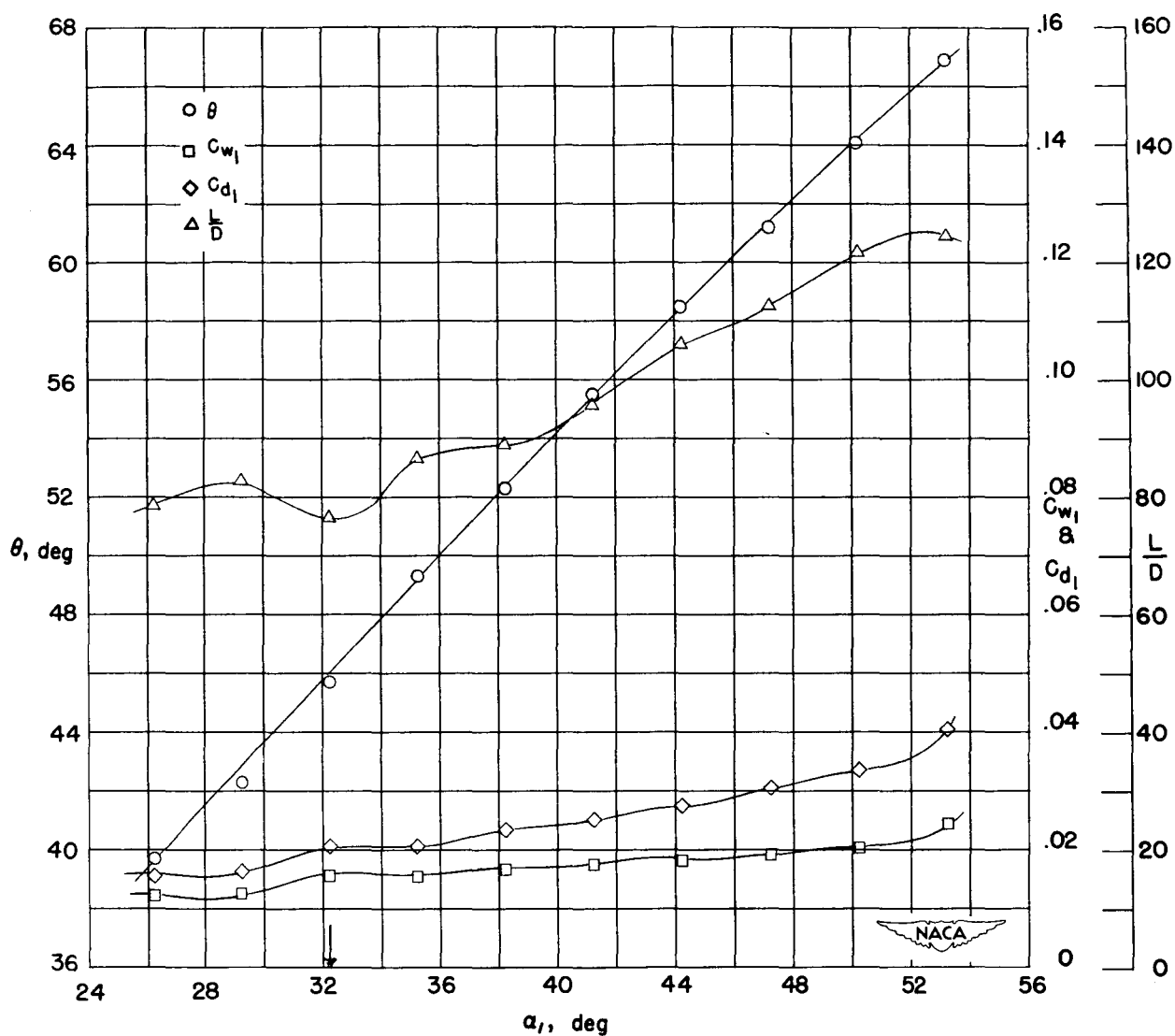


Figure 8.- Low-speed pressure distributions and section characteristics for the cascade combinations  $\beta_1 = 0^\circ$ ,  $\sigma = 1.5$ ,  $\theta_c = 65^\circ$ .



(f) Section characteristics; arrow shows design angle of attack.

Figure 8.- Concluded.

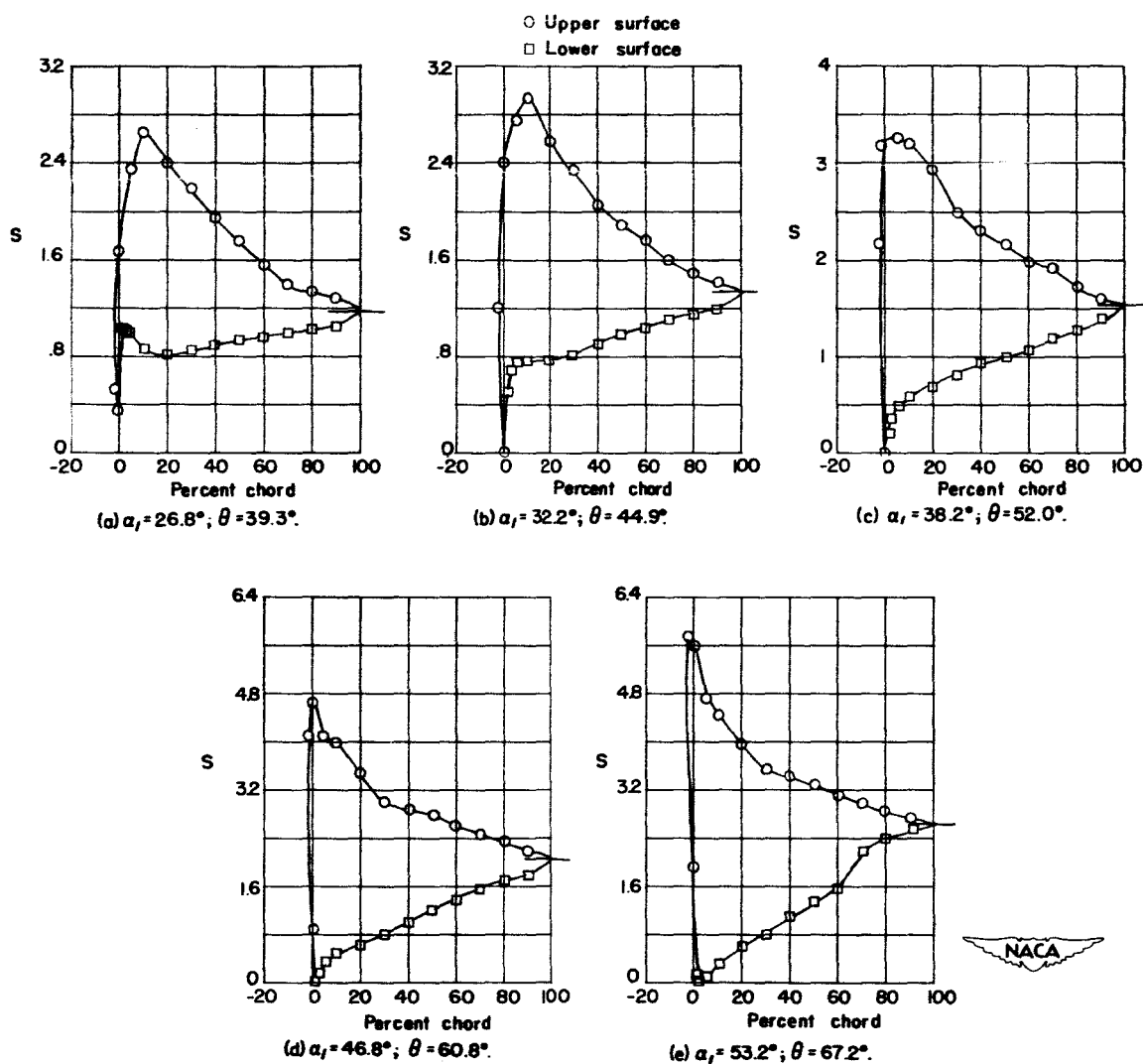
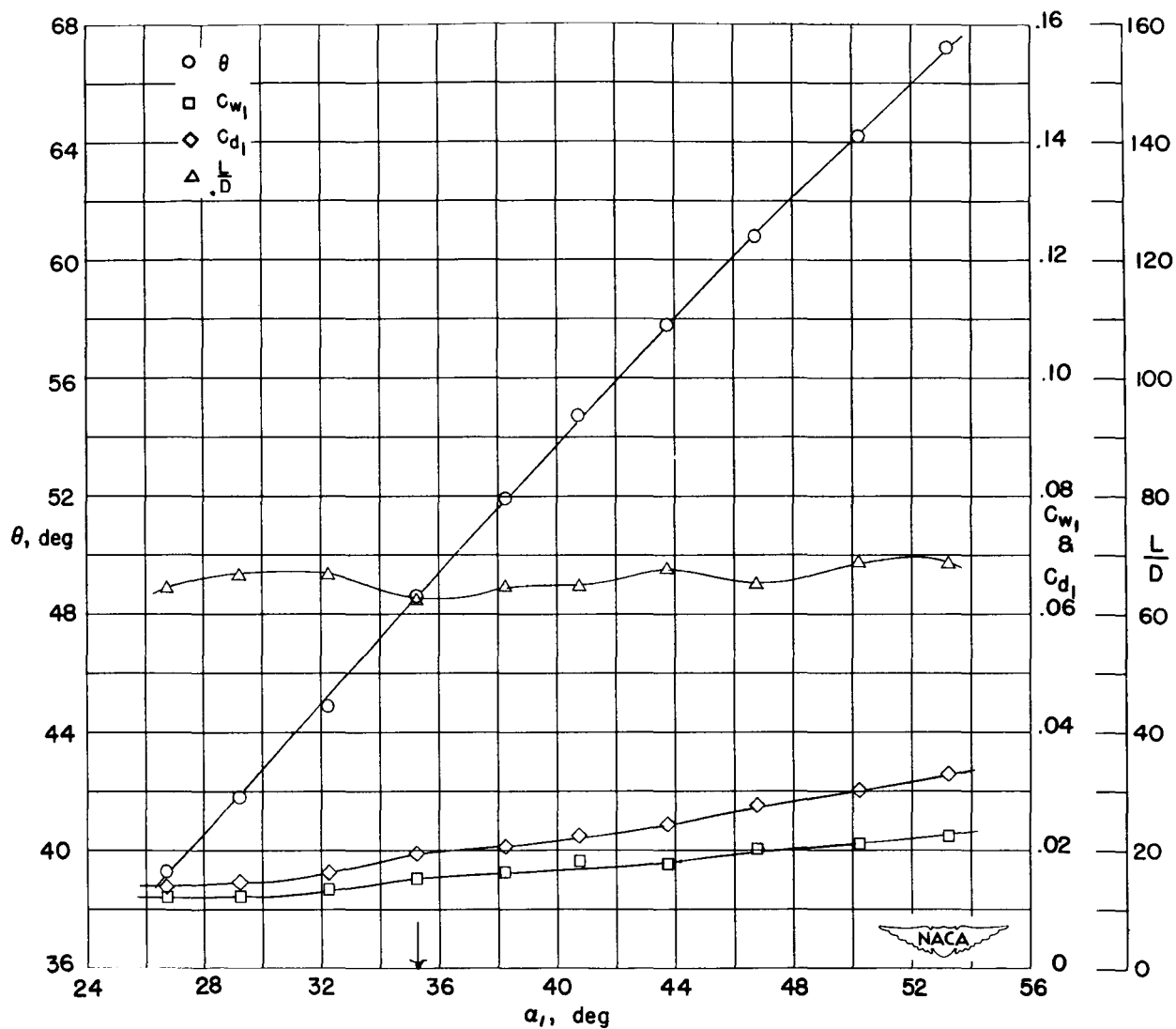


Figure 9.- Low-speed pressure distributions and section characteristics for the cascade combinations  $\beta_1 = 15^\circ$ ,  $\sigma = 1.5$ ,  $\theta_c = 65^\circ$ .





(f) Section characteristics; arrow shows design angle of attack.

Figure 9.- Concluded.

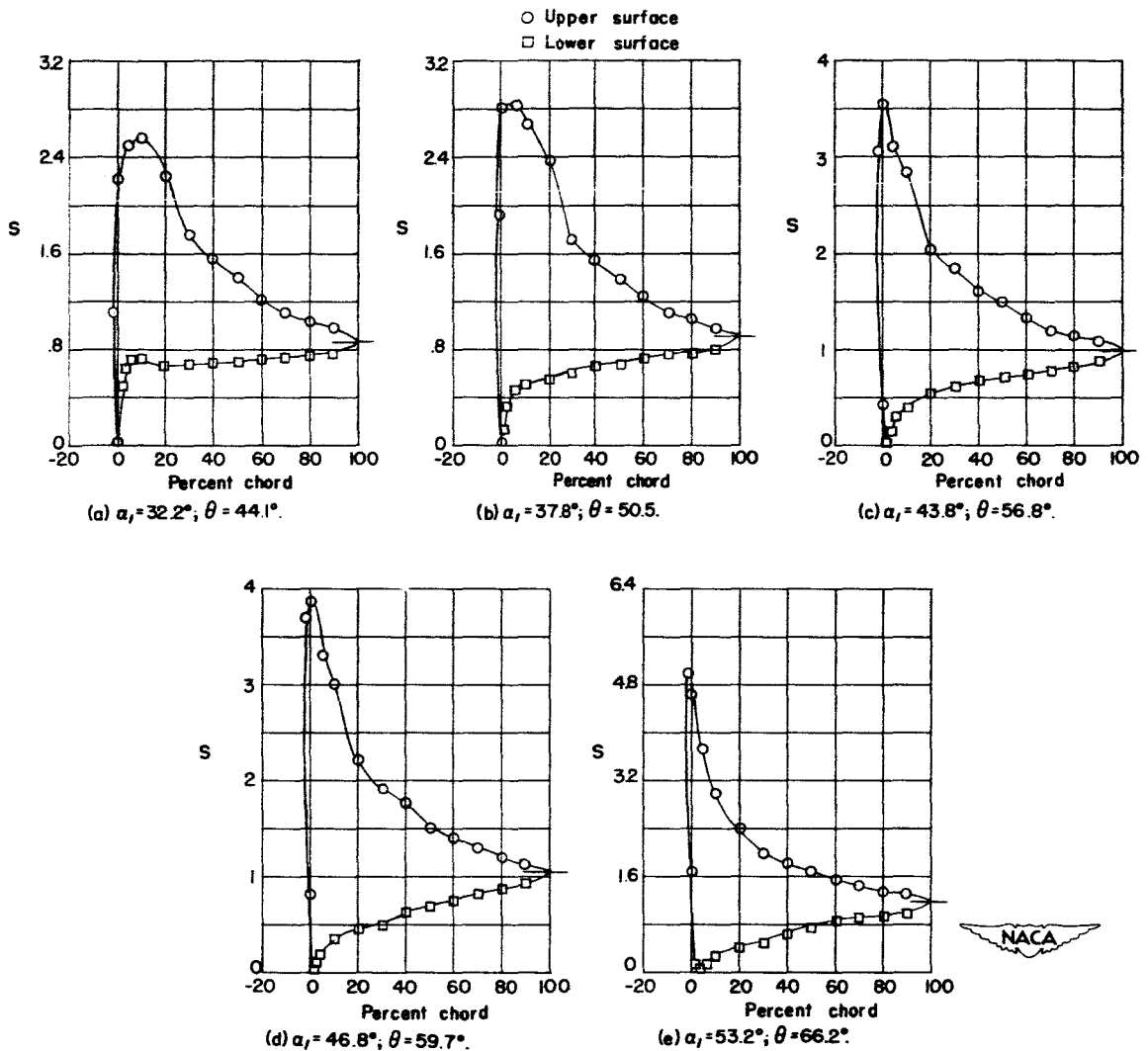
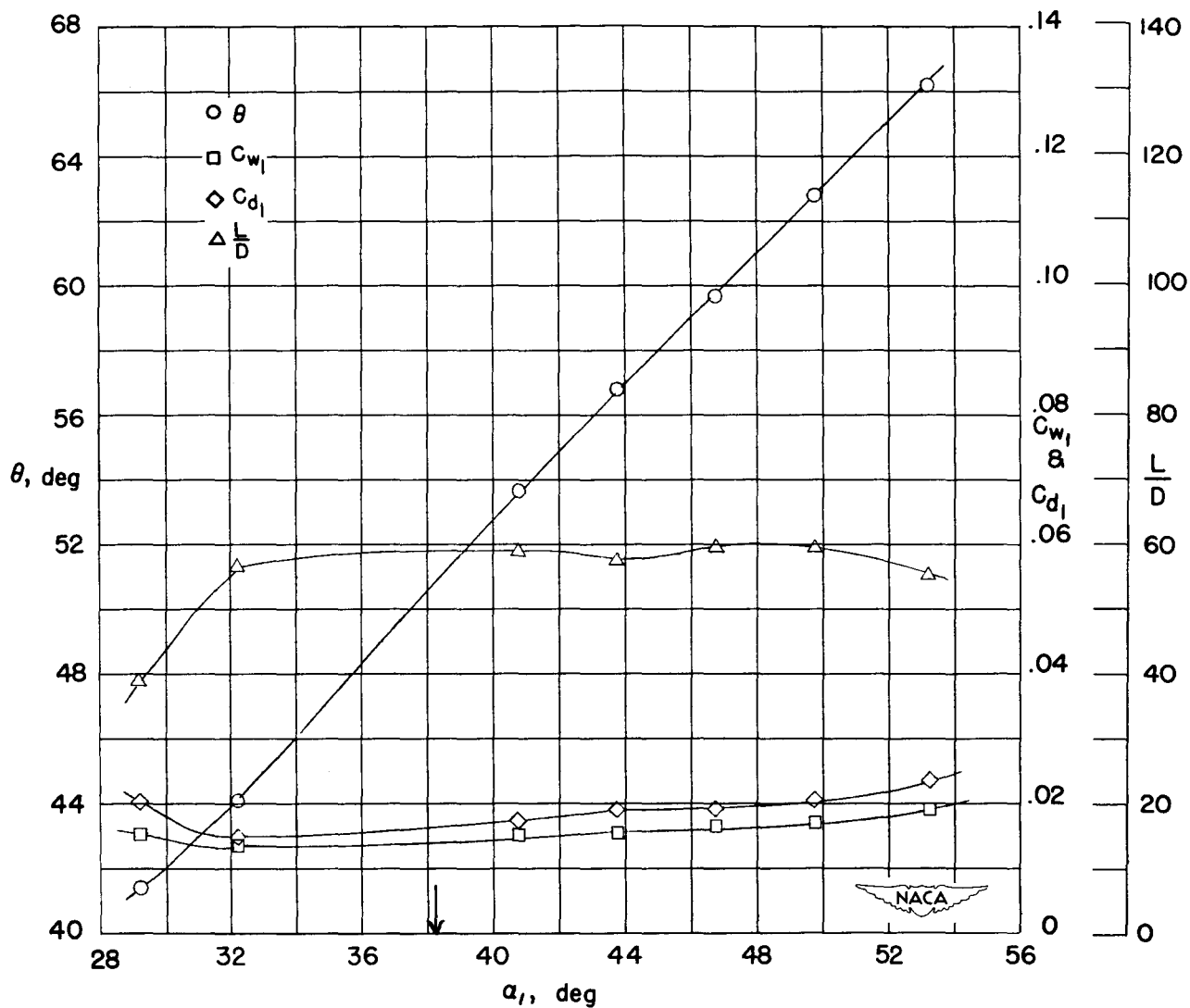


Figure 10.- Low-speed pressure distributions and section characteristics for the cascade combinations  $\beta_1 = 30^\circ$ ,  $\sigma = 1.5$ ,  $\theta_c = 65^\circ$ .



(f) Section characteristics; arrow shows design angle of attack.

Figure 10.- Concluded.

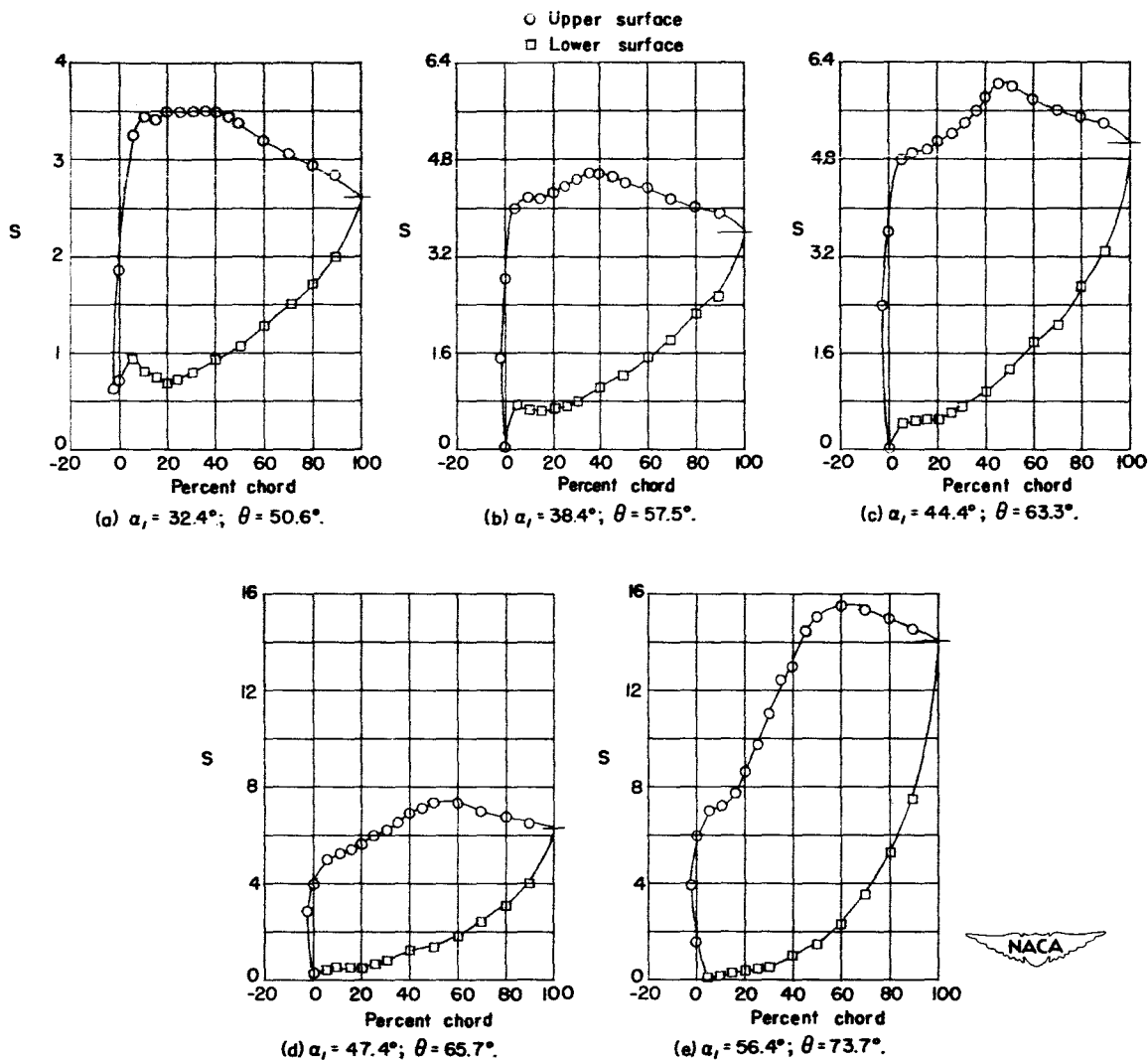
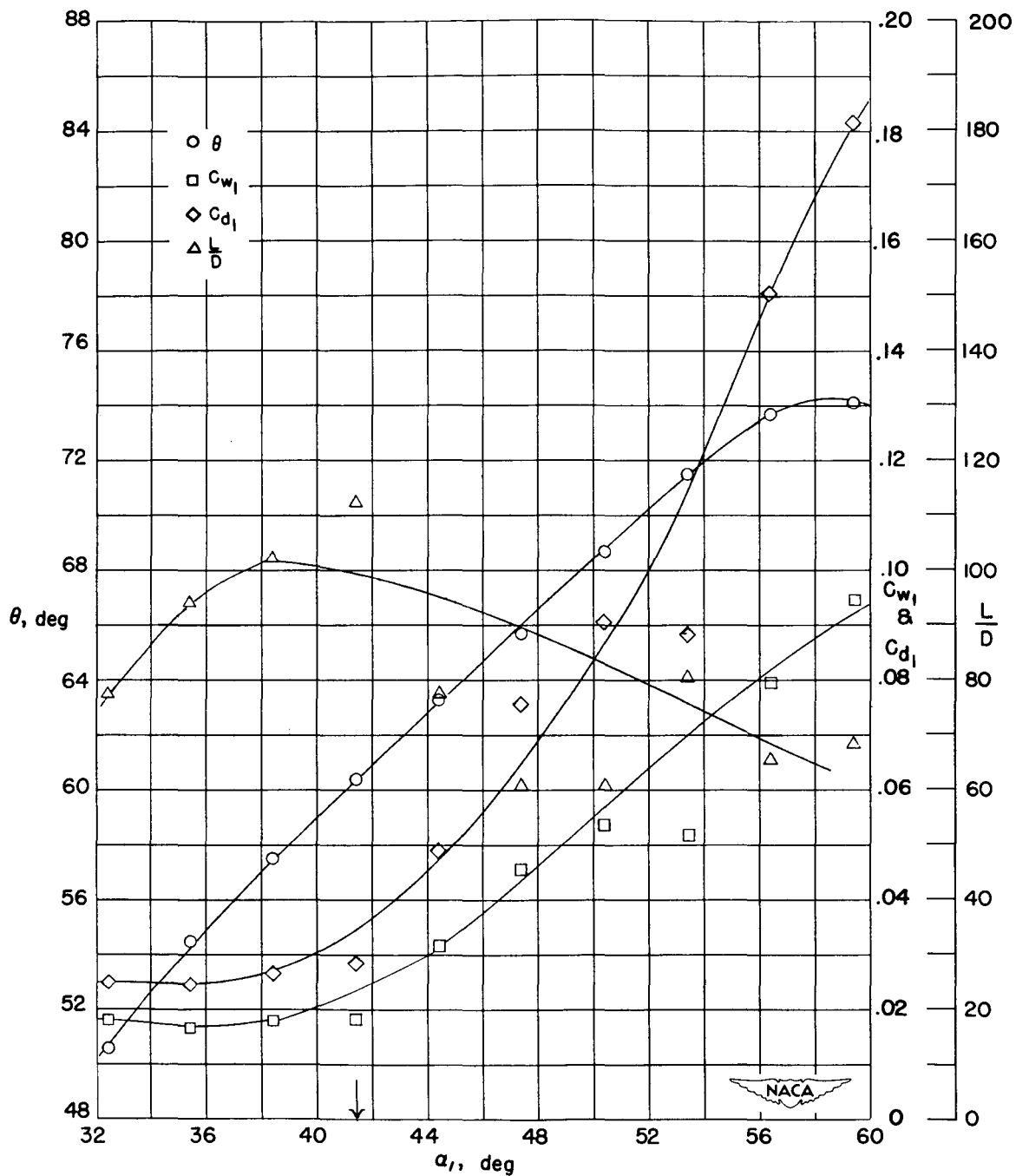


Figure 11.- Low-speed pressure distributions and section characteristics for the cascade combinations  $\beta_1 = 0^\circ$ ,  $\sigma = 1.5$ ,  $\theta_c = 80^\circ$ .



(f) Section characteristics; arrow shows design angle of attack.

Figure 11.- Concluded.

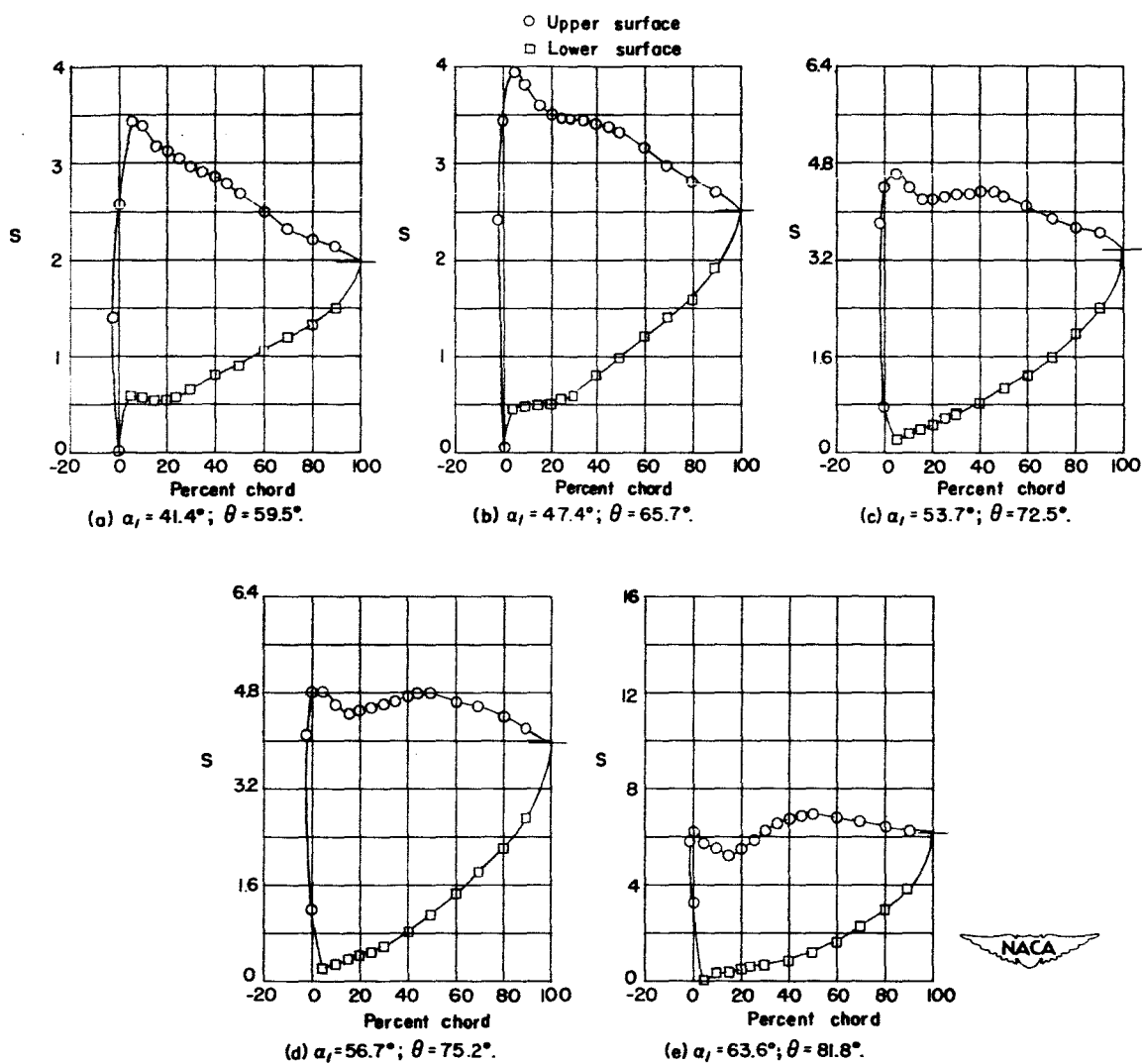
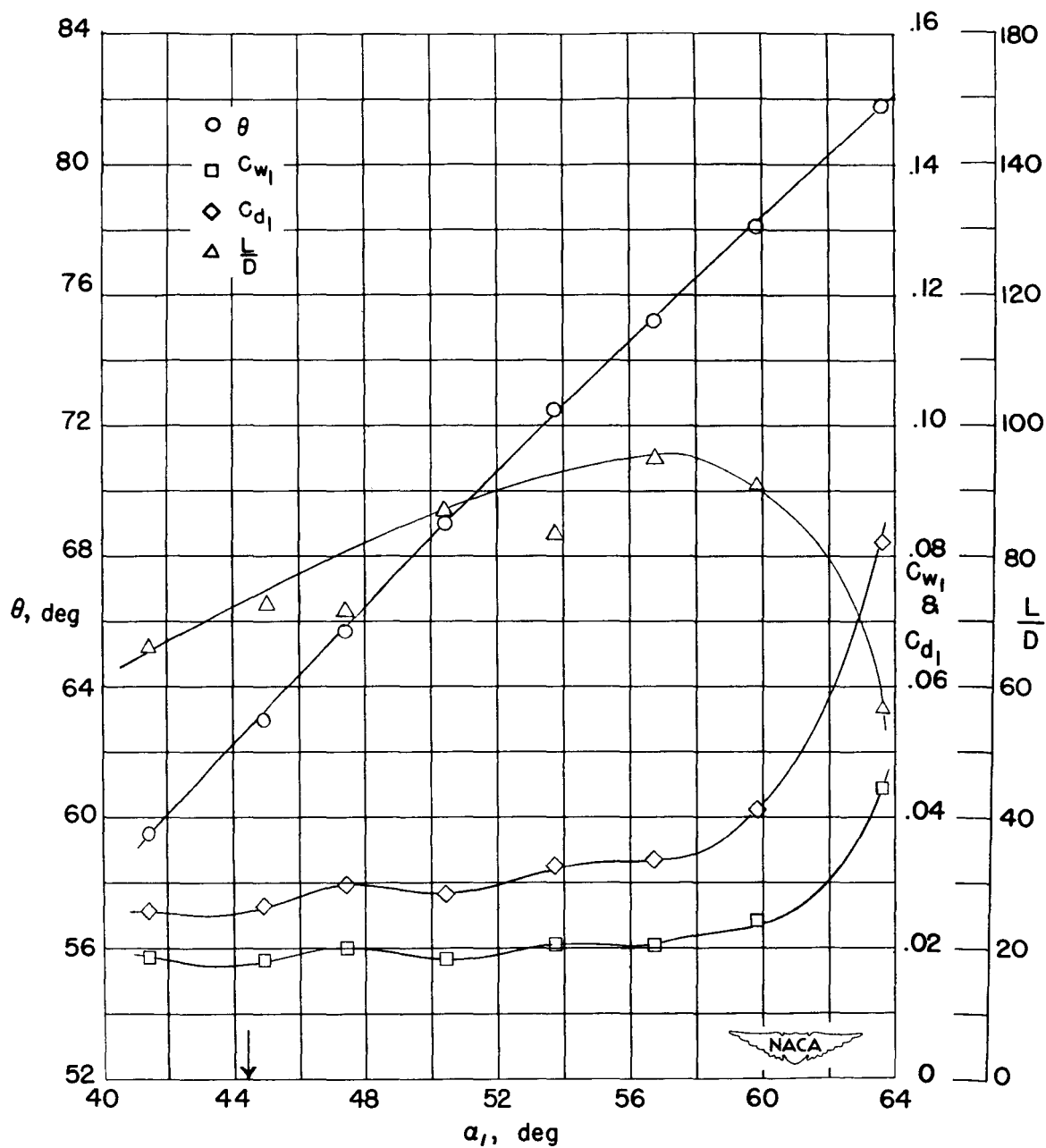


Figure 12.- Low-speed pressure distributions and section characteristics for the cascade combinations  $\beta_1 = 15^\circ$ ,  $\sigma = 1.5$ ,  $\theta_c = 80^\circ$ .



(f) Section characteristics; arrow shows design angle of attack.

Figure 12.- Concluded.

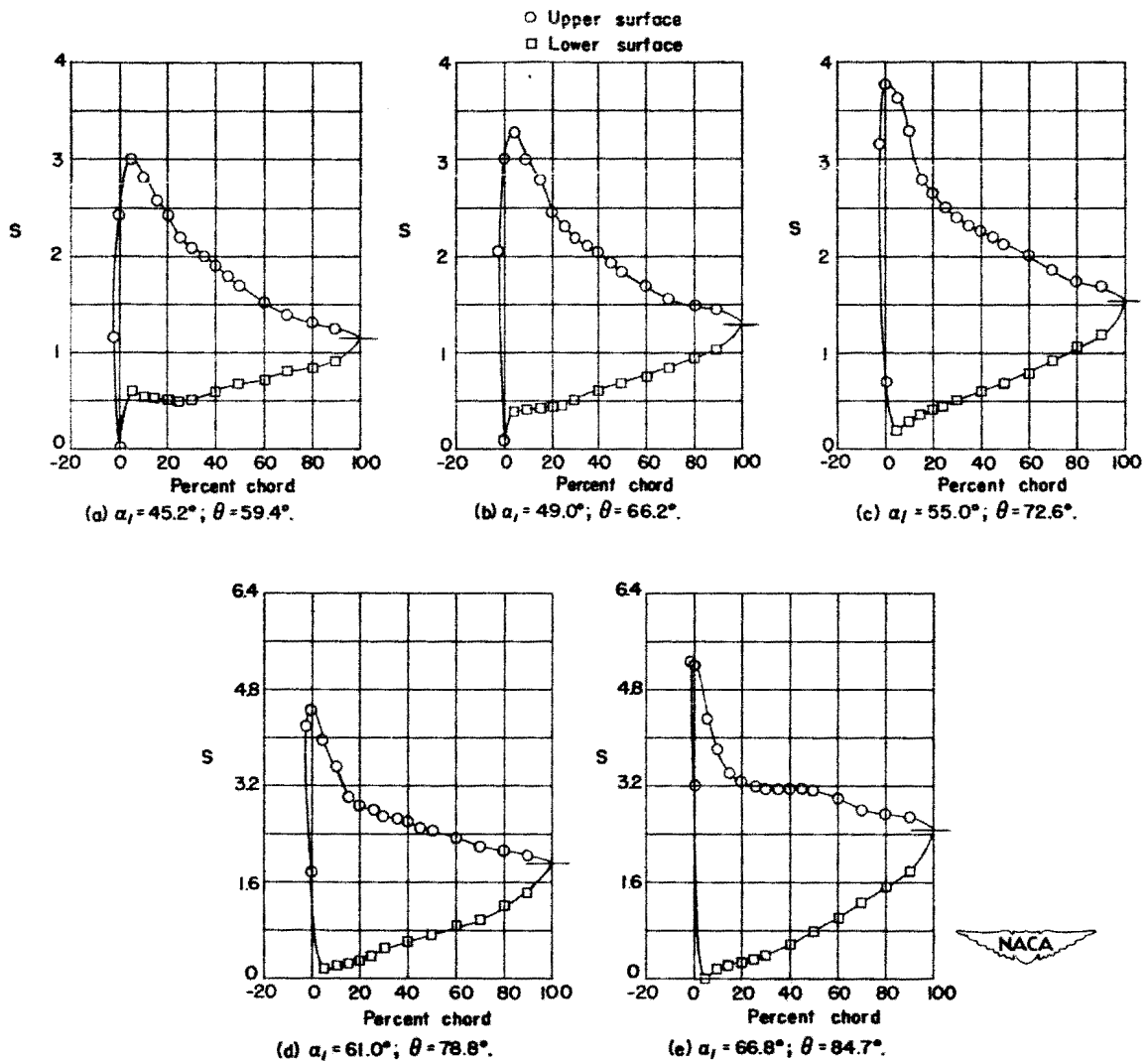
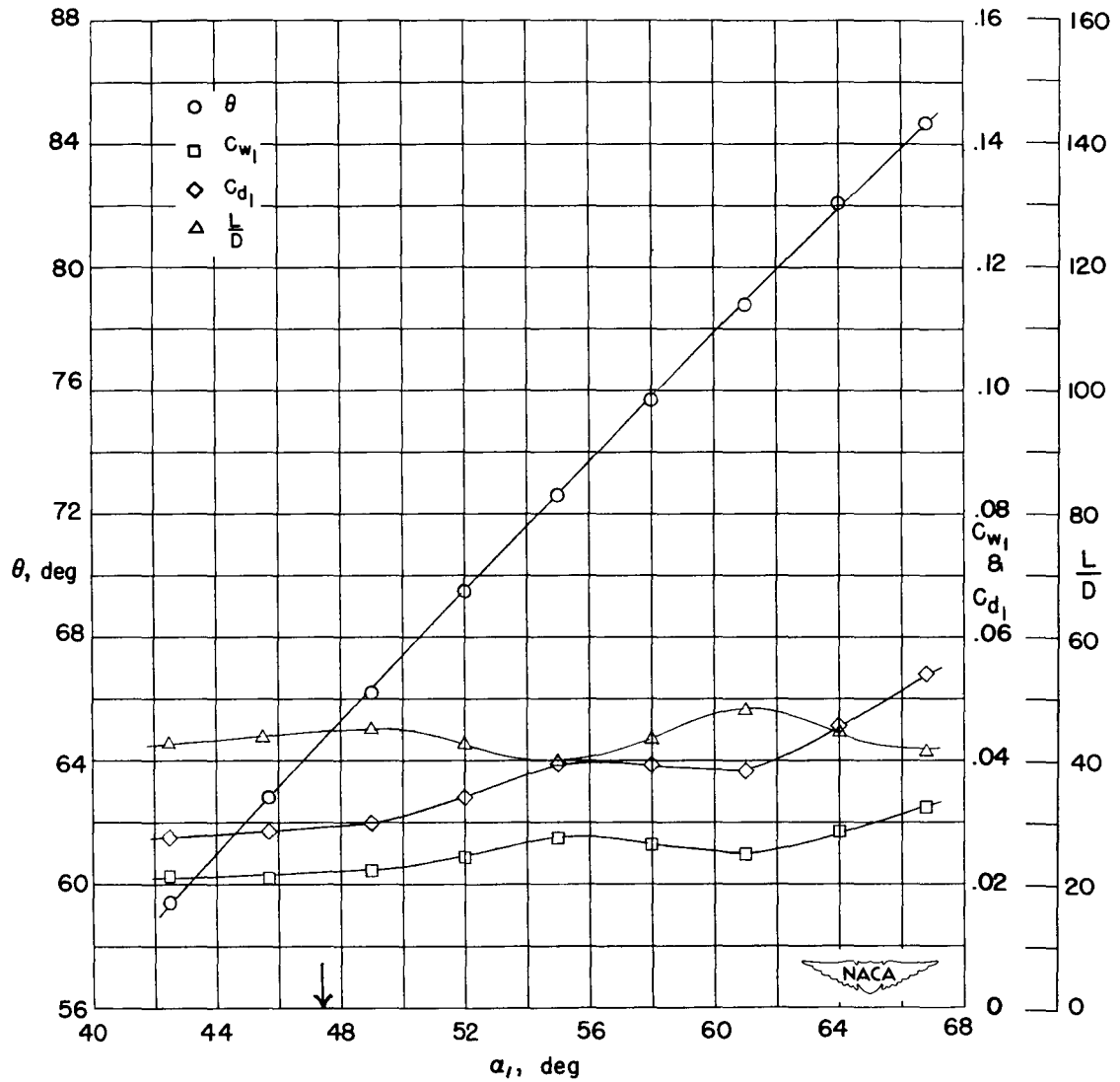


Figure 13.- Low-speed pressure distributions and section characteristics for the cascade combinations  $\beta_1 = 30^\circ$ ,  $\sigma = 1.5$ ,  $\theta_c = 80^\circ$ .





(f) Section characteristics; arrow shows design angle of attack.

Figure 13.- Concluded.

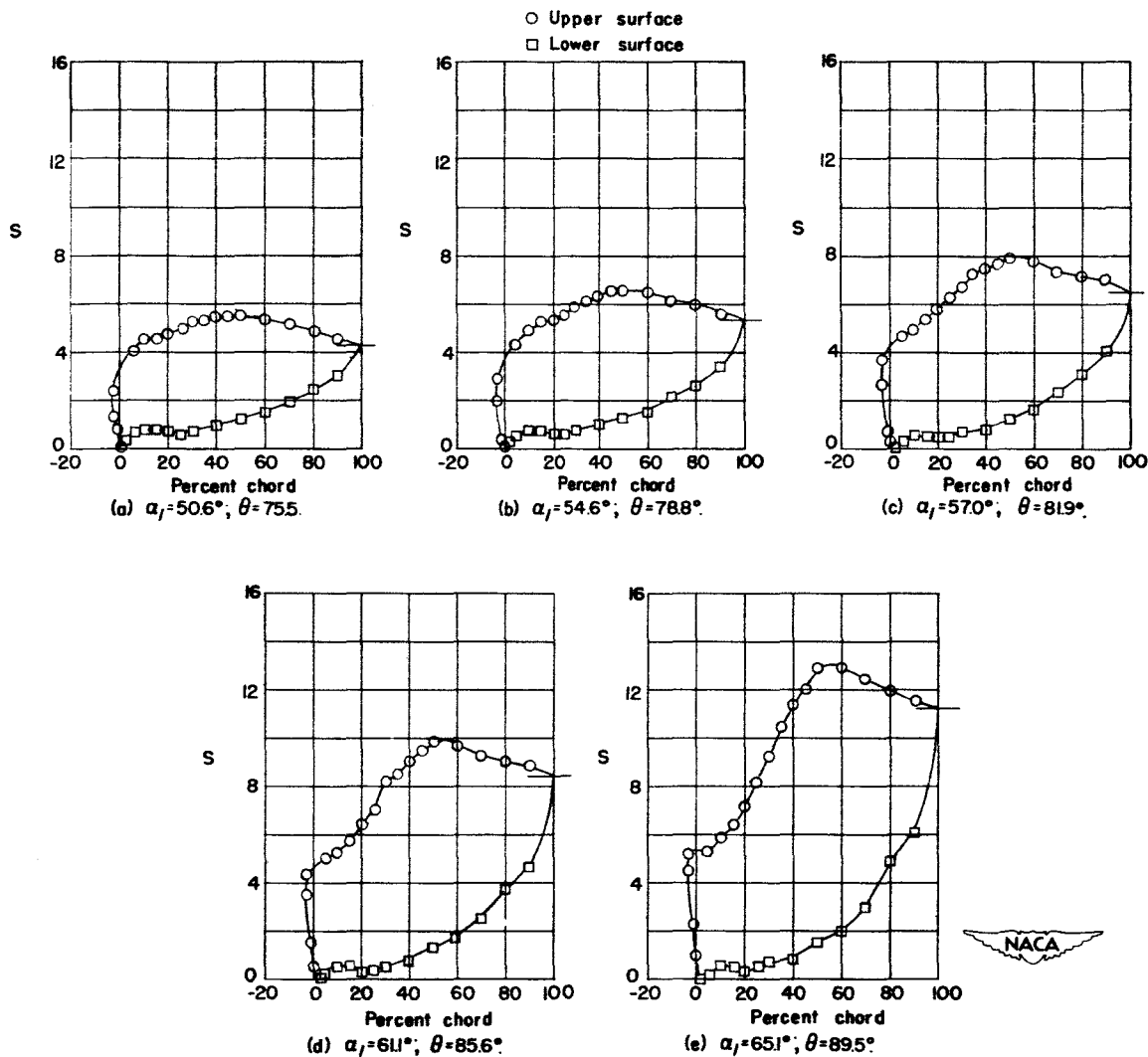
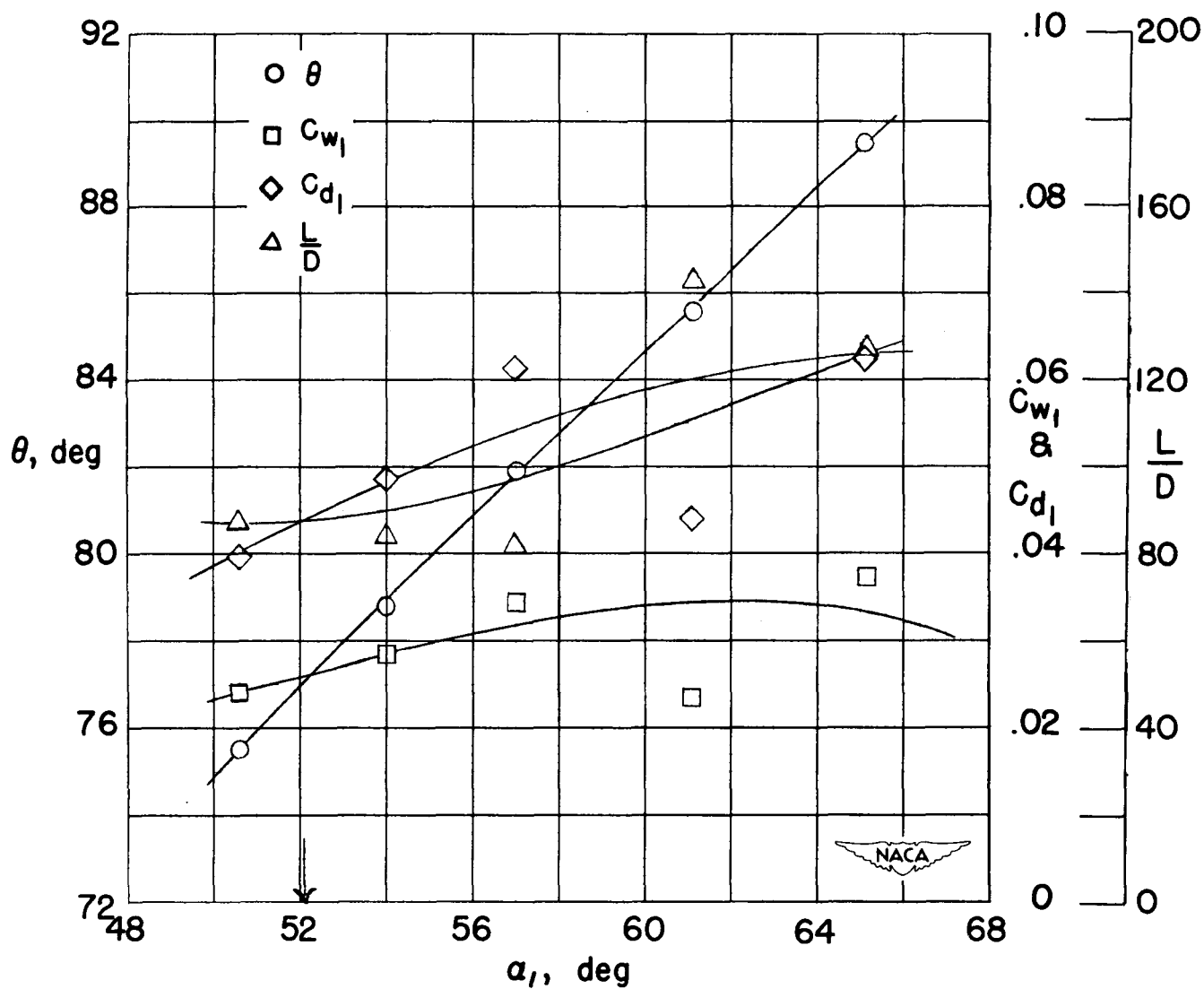


Figure 14.- Low-speed pressure distributions and section characteristics for the cascade combinations  $\beta_1 = 15^\circ$ ,  $\sigma = 1.5$ ,  $\theta_c = 95^\circ$ .



(f) Section characteristics; arrow shows design angle of attack.

Figure 14.- Concluded.

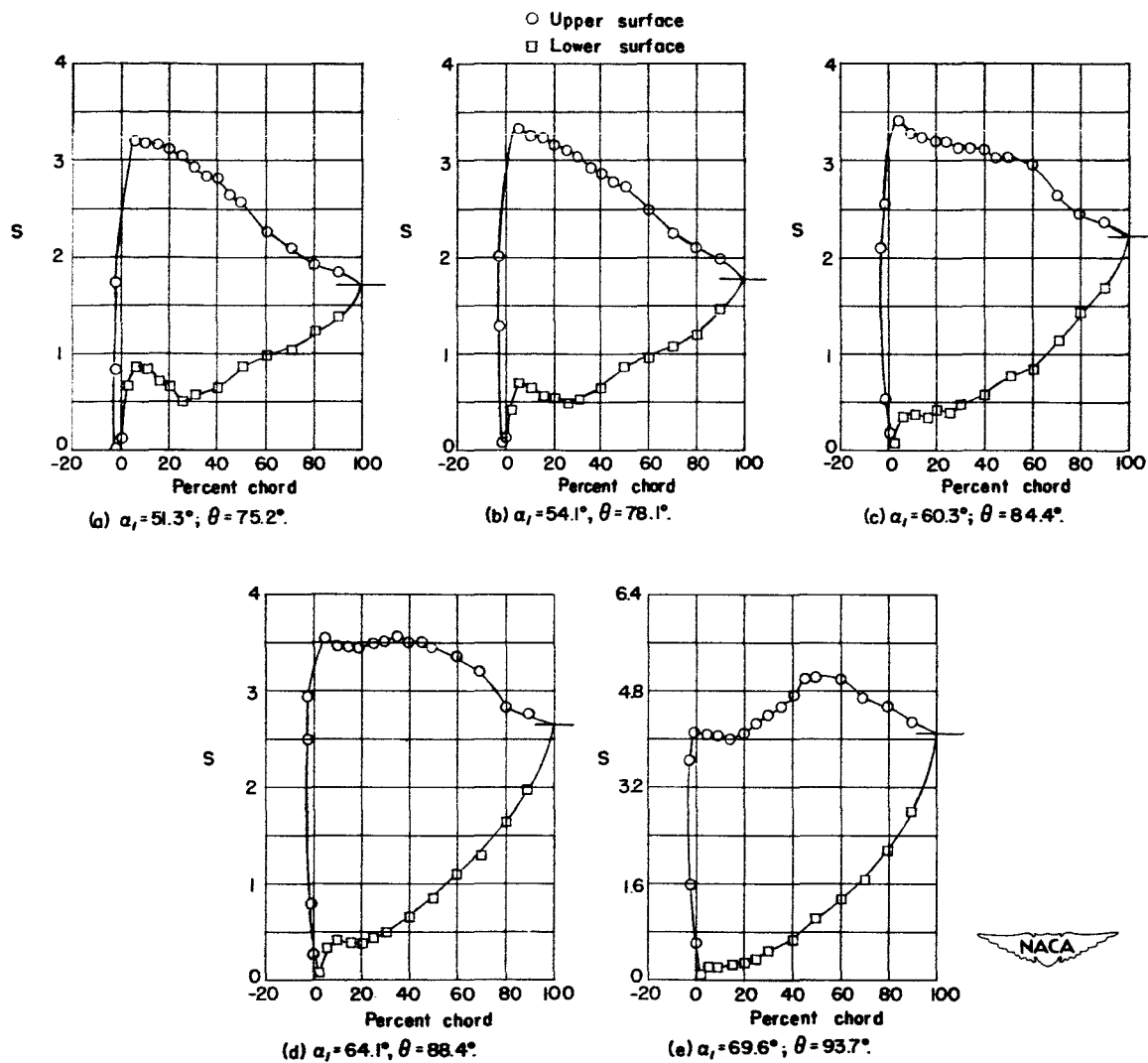
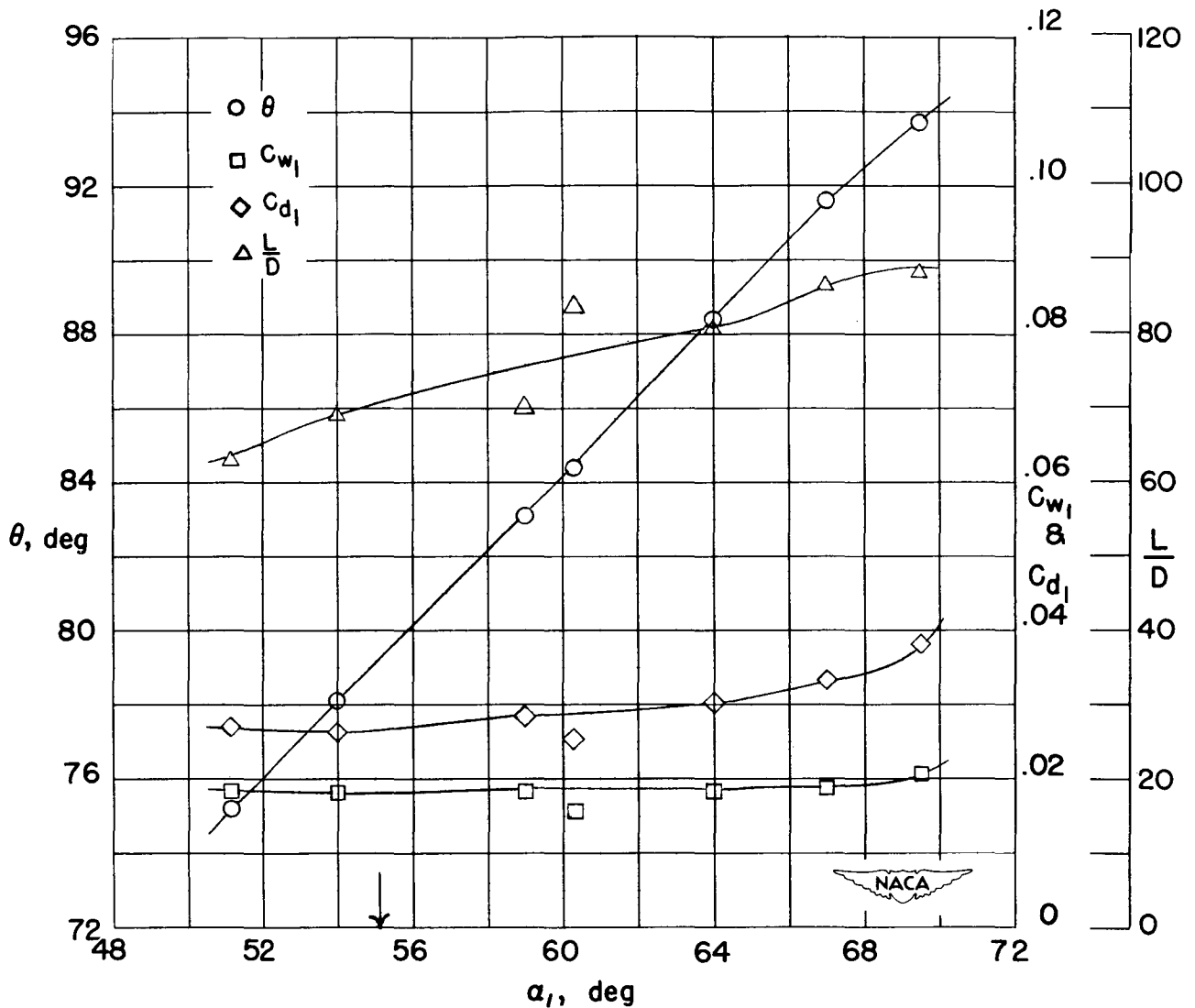


Figure 15.- Low-speed pressure distributions and section characteristics for the cascade combinations  $\beta_1 = 30^\circ$ ,  $\sigma = 1.5$ ,  $\theta_c = 95^\circ$ .



(f) Section characteristics; arrow shows design angle of attack.

Figure 15.- Concluded.

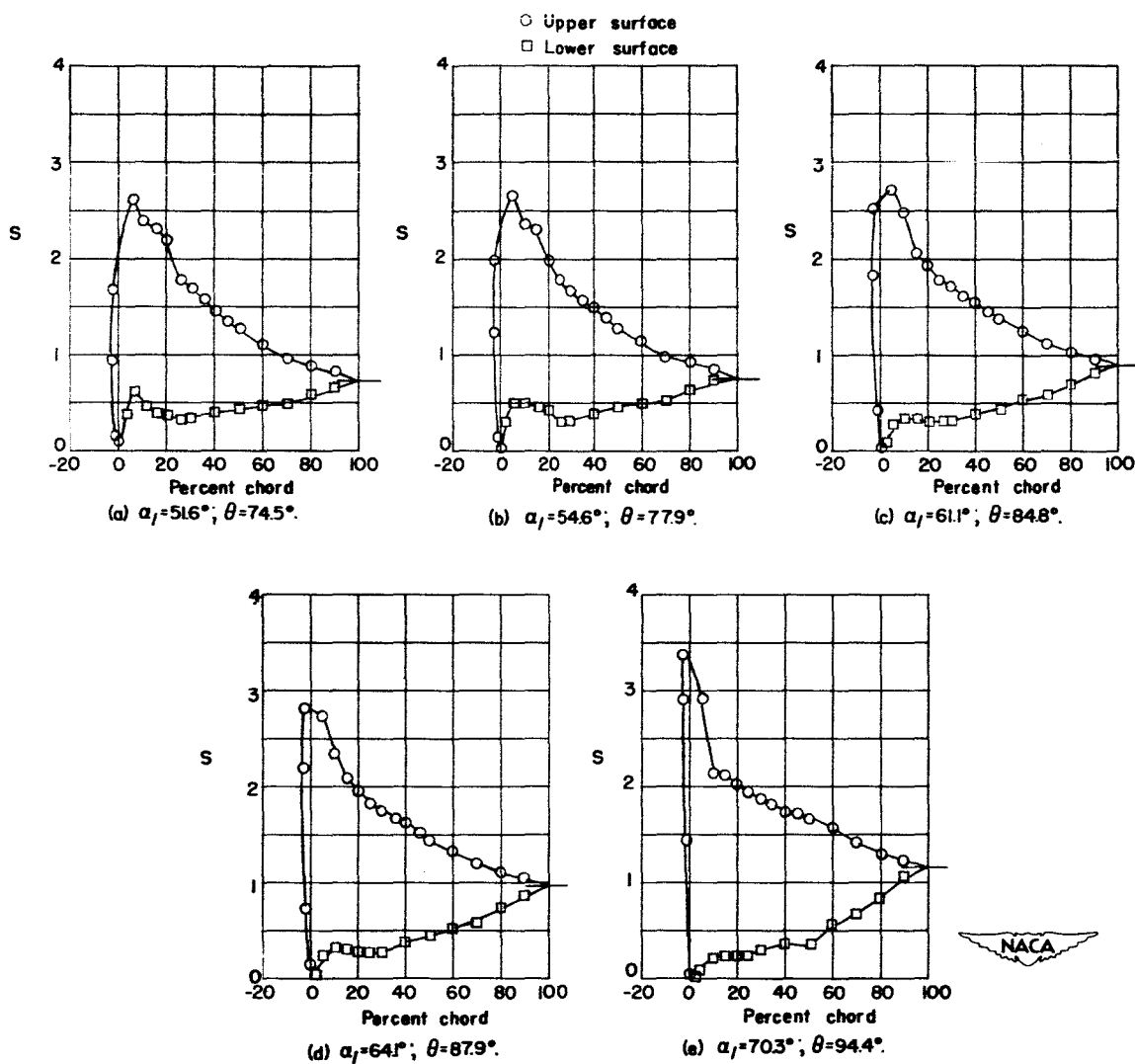
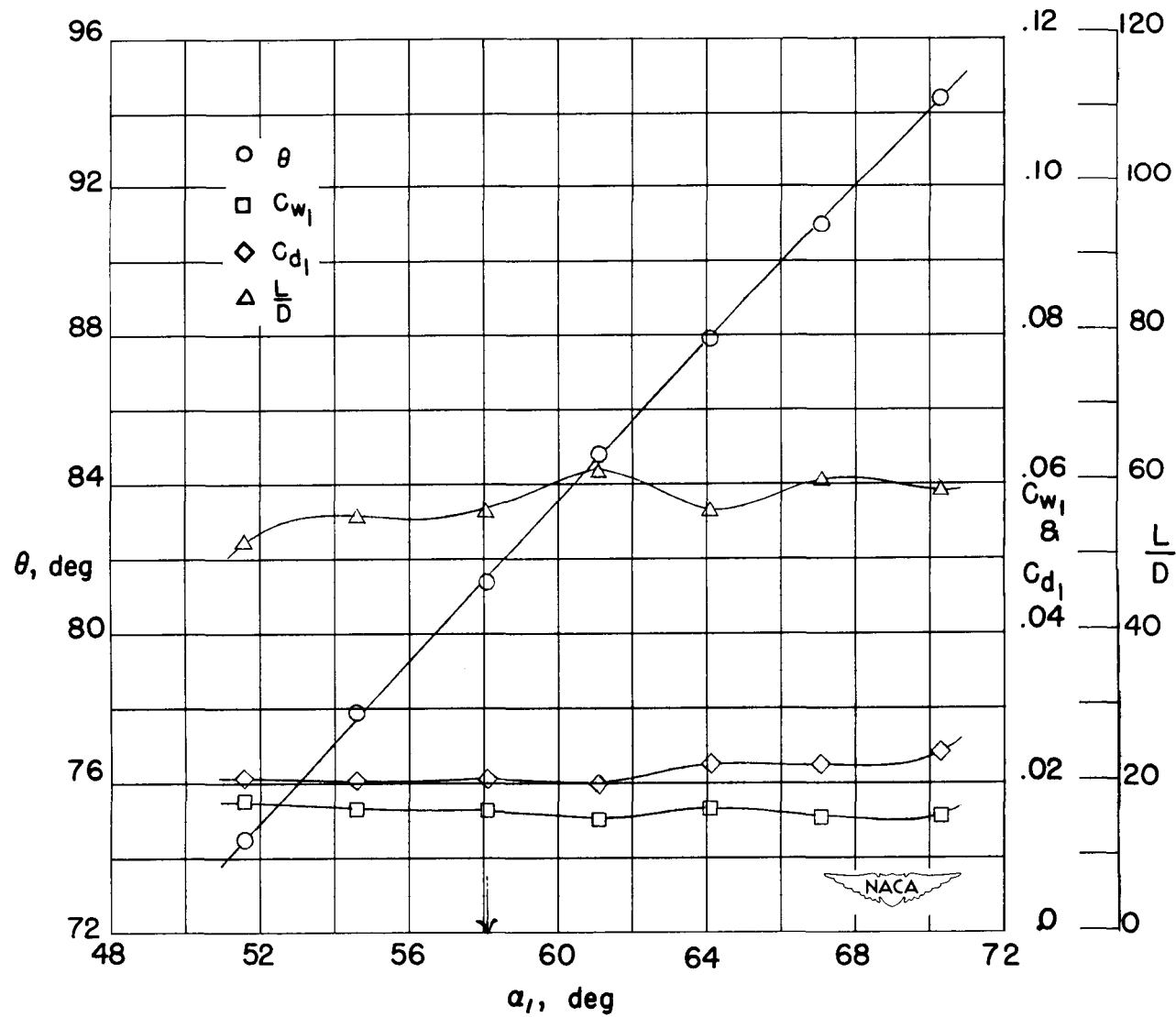


Figure 16.- Low-speed pressure distributions and section characteristics for the cascade combinations  $\beta_1 = 45^\circ$ ,  $\sigma = 1.5$ ,  $\theta_c = 95^\circ$ .



(f) Section characteristics; arrow shows design angle of attack.

Figure 16.- Concluded.

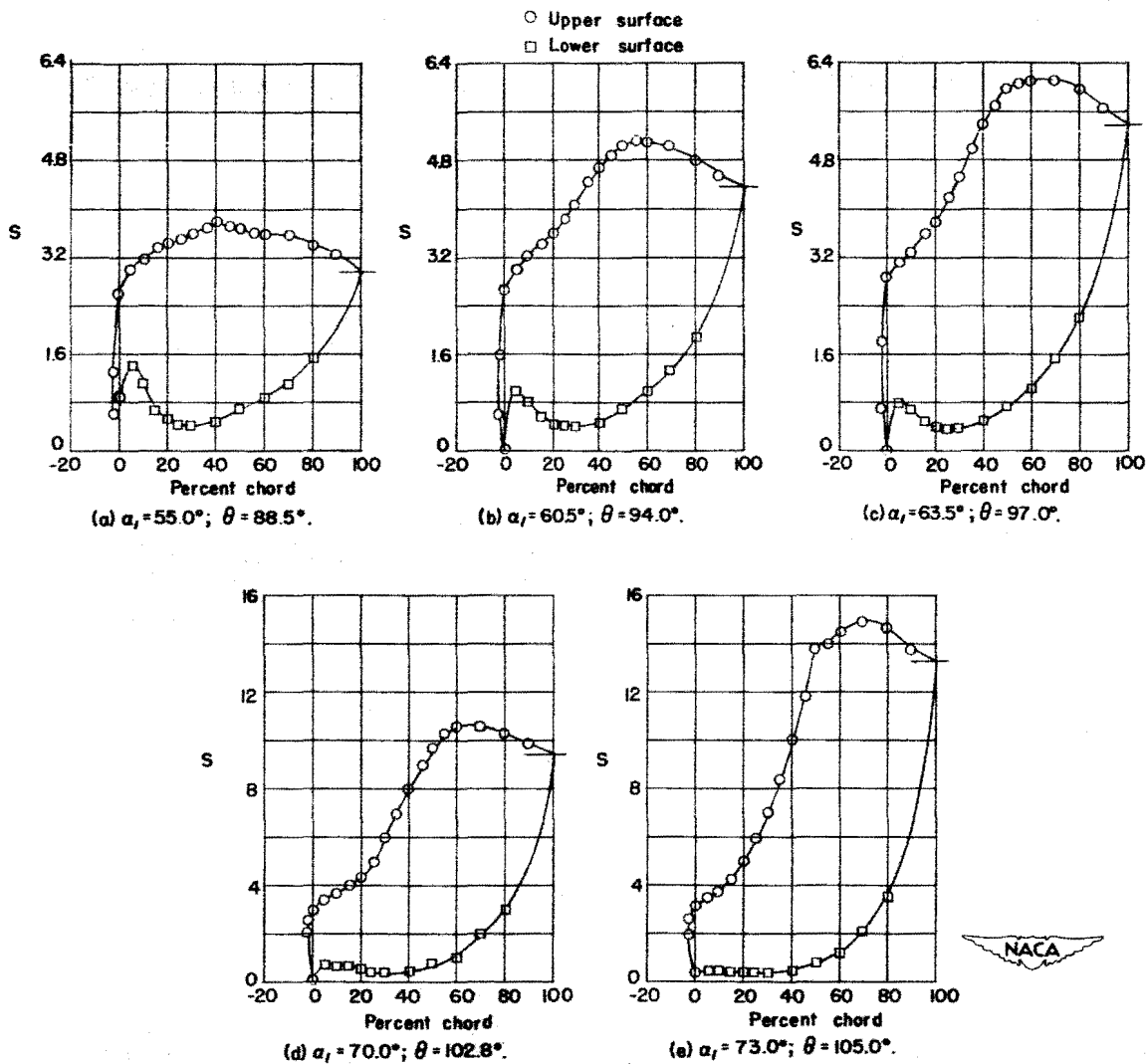
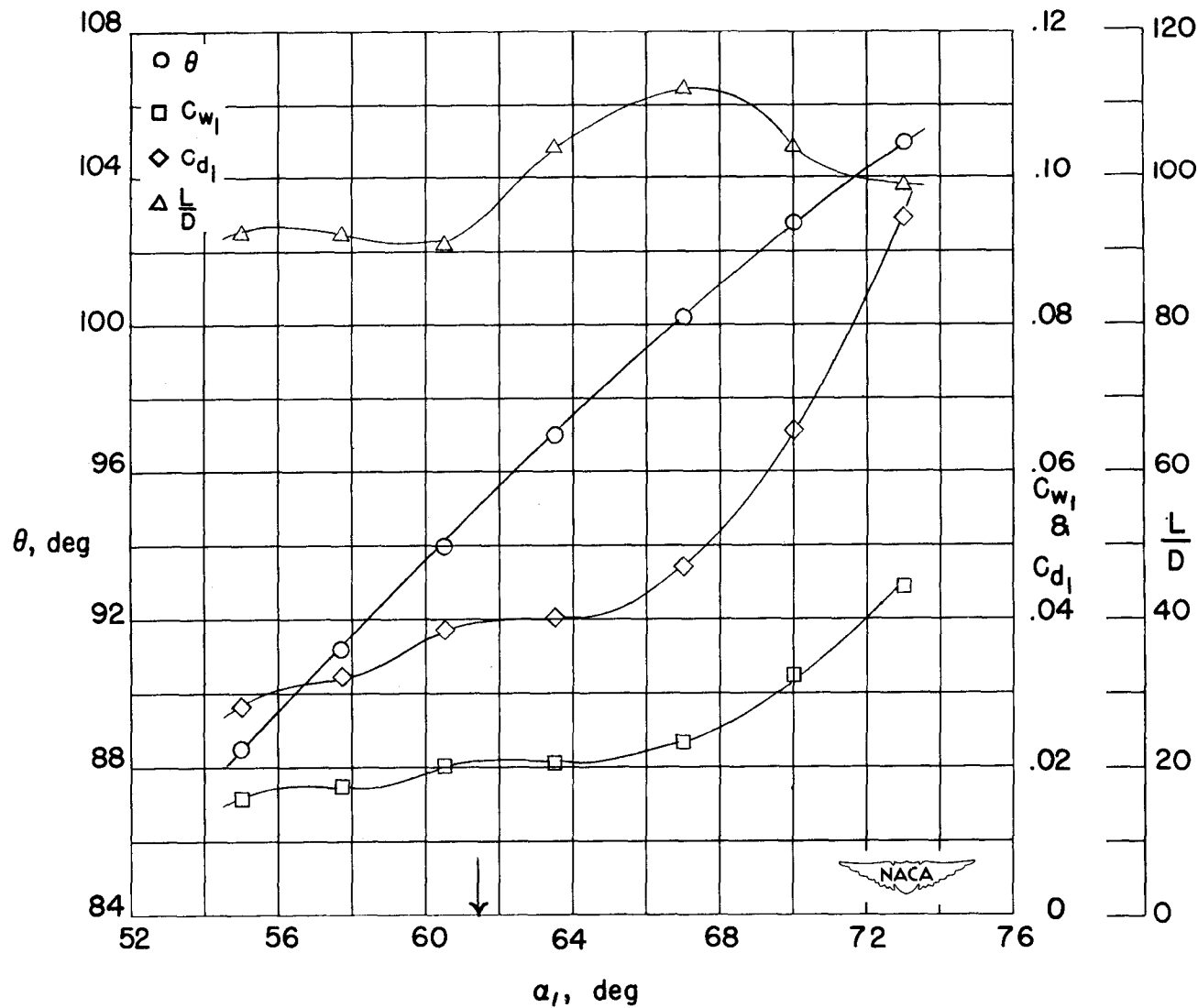


Figure 17.- Low-speed pressure distributions and section characteristics for the cascade combinations  $\beta_1 = 30^\circ$ ,  $\sigma = 1.5$ ,  $\theta_c = 110^\circ$ . Wire screen in throat.





(f) Section characteristics; arrow shows design angle of attack.

Figure 17.- Concluded.

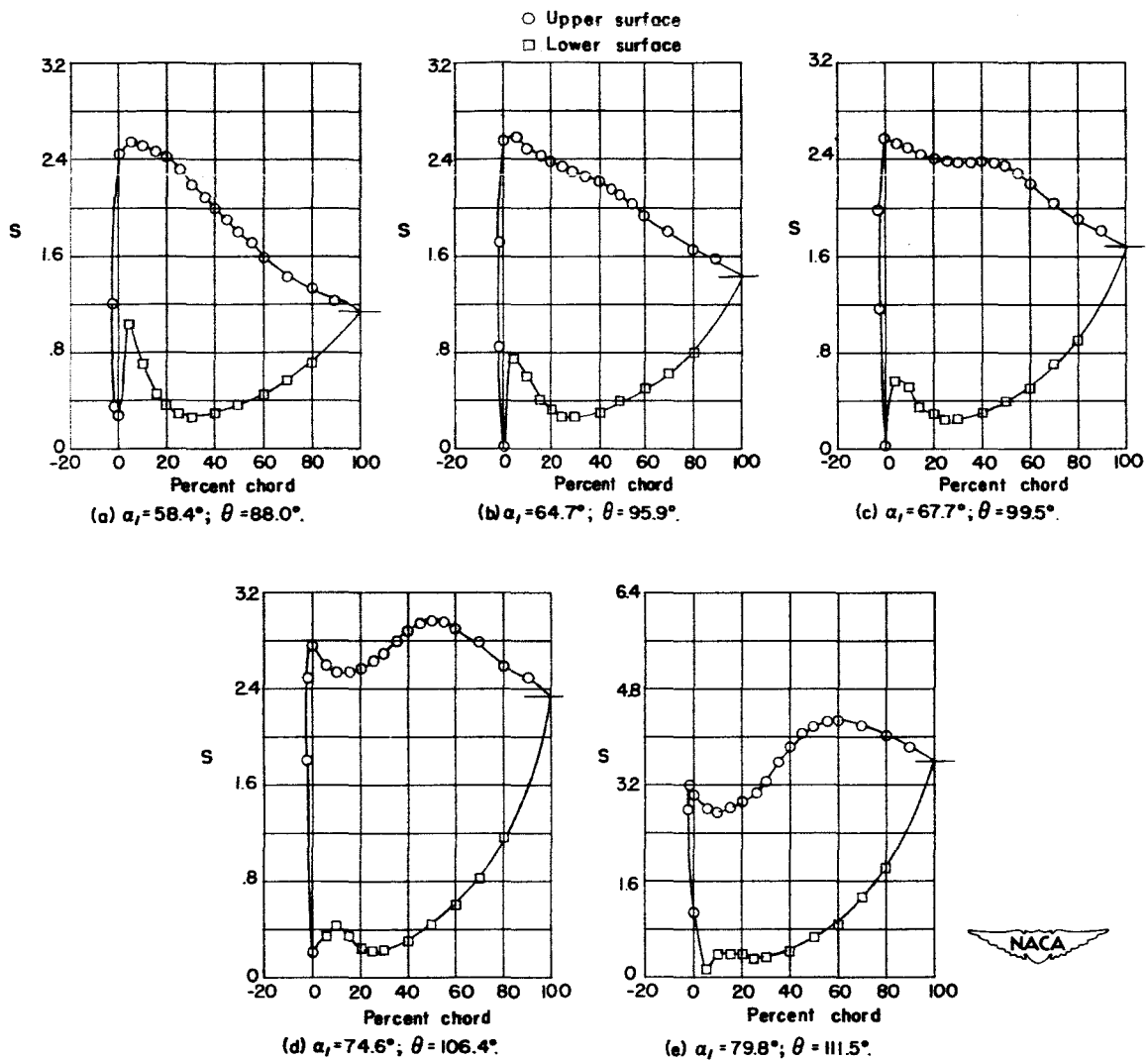
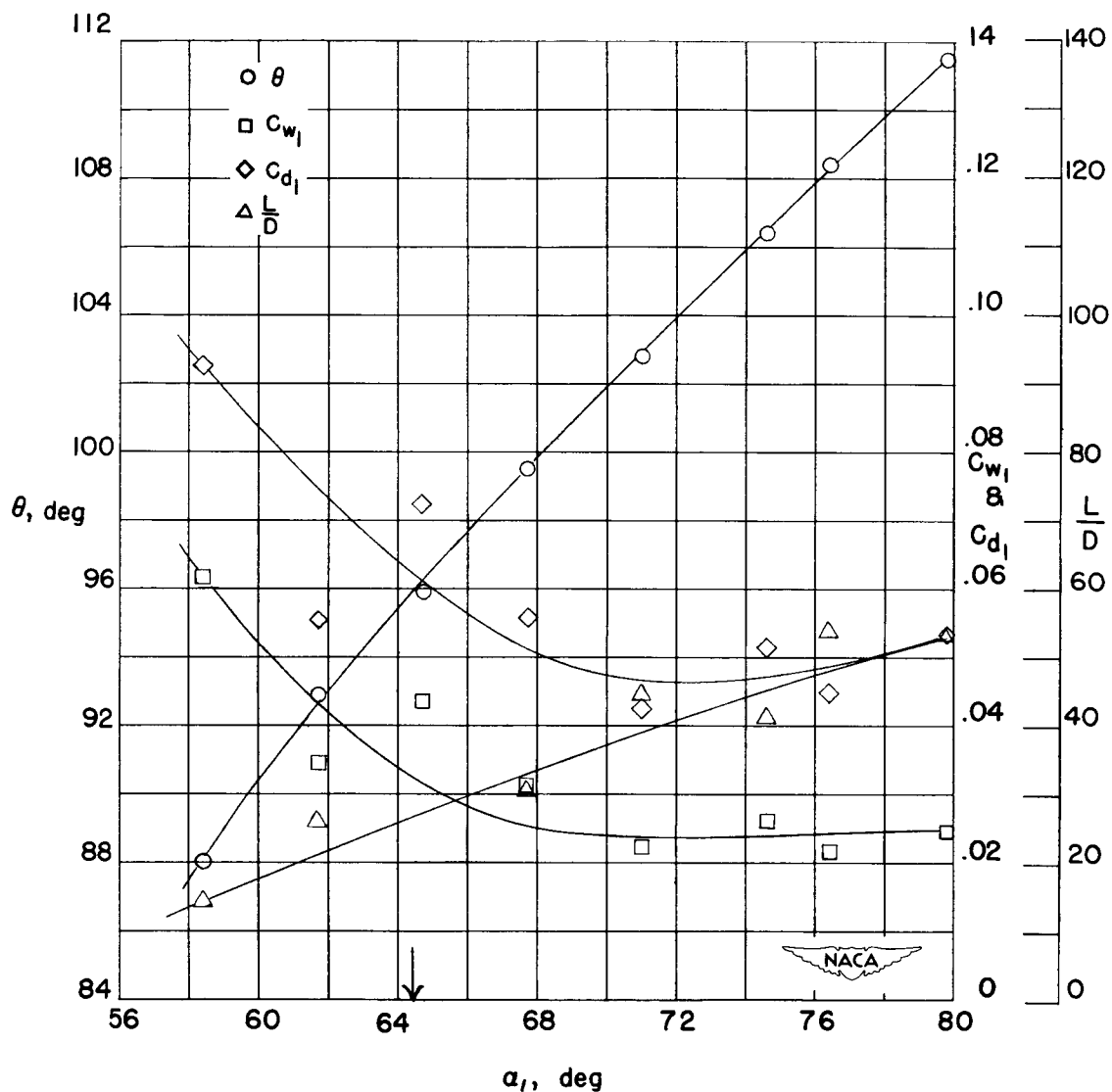


Figure 18.- Low-speed pressure distributions and section characteristics for the cascade combinations  $\beta_1 = 45^\circ$ ,  $\sigma = 1.5$ ,  $\theta_c = 110^\circ$ . Wire screen in throat.



(f) Section characteristics; arrow shows design angle of attack.

Figure 18.- Concluded.

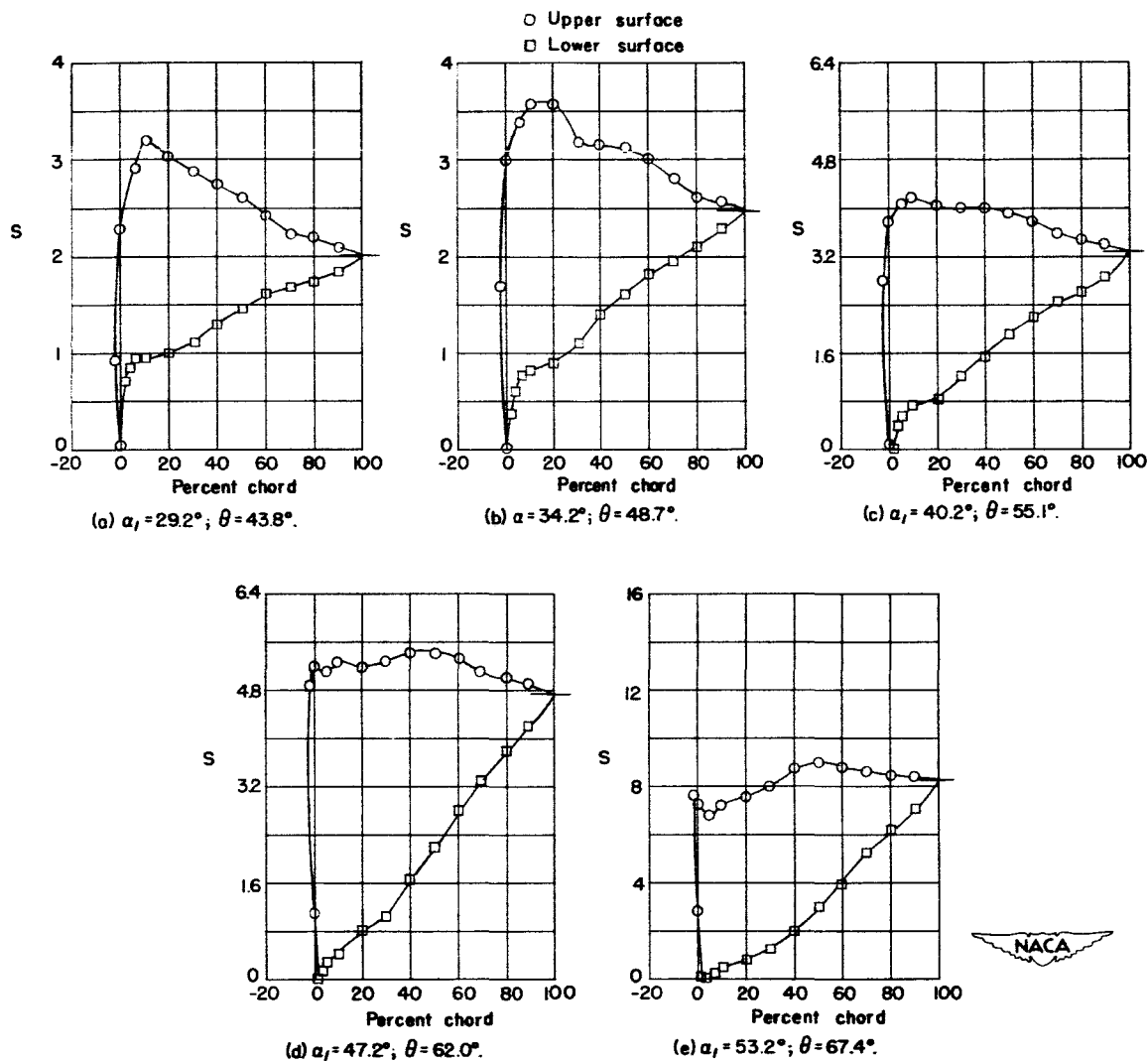
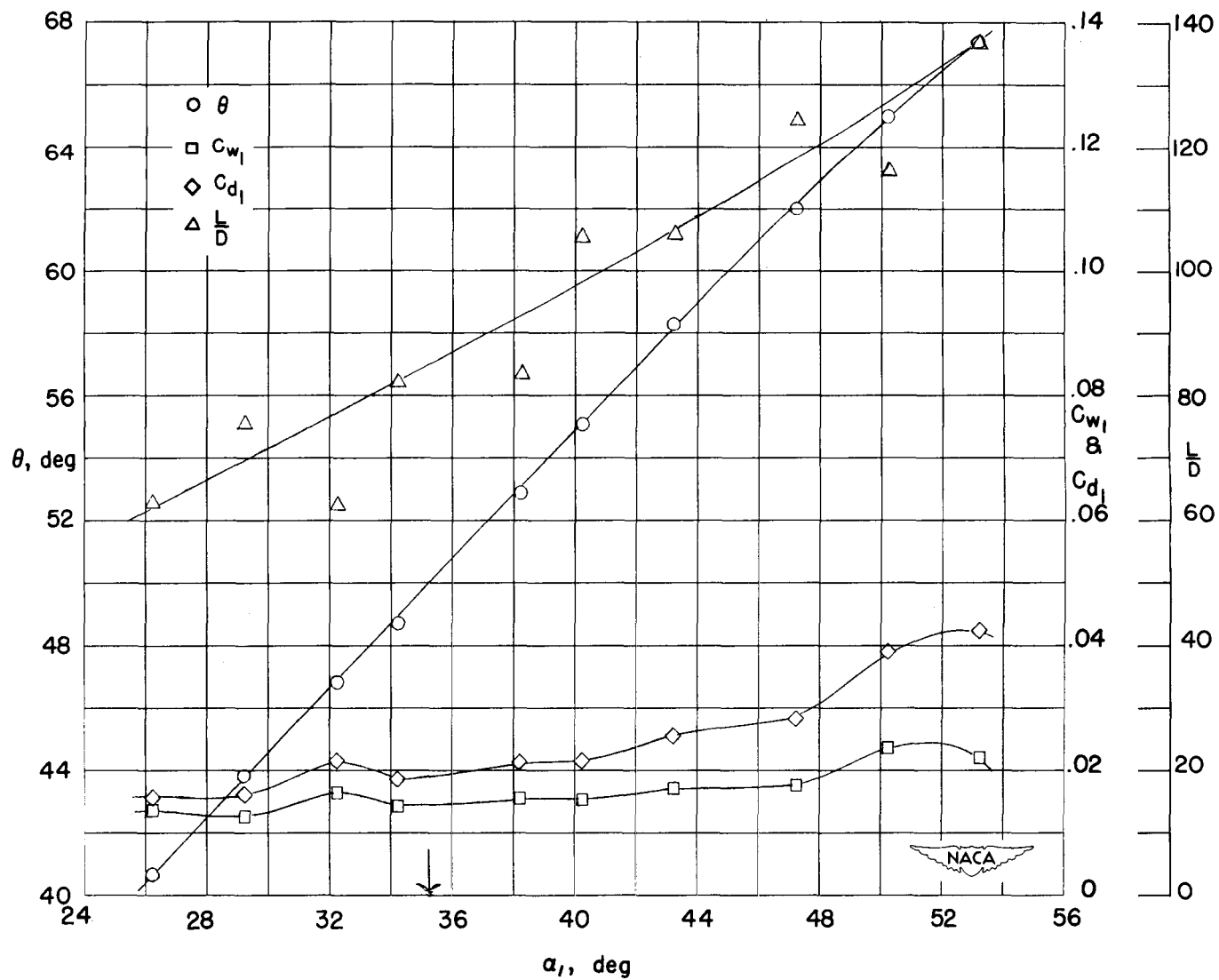


Figure 19.- Low-speed pressure distributions and section characteristics for the cascade combinations  $\beta_1 = 0^\circ$ ,  $\sigma = 1.8$ ,  $\theta_c = 65^\circ$ .



(f) Section characteristics; arrow shows design angle of attack.

Figure 19.- Concluded.

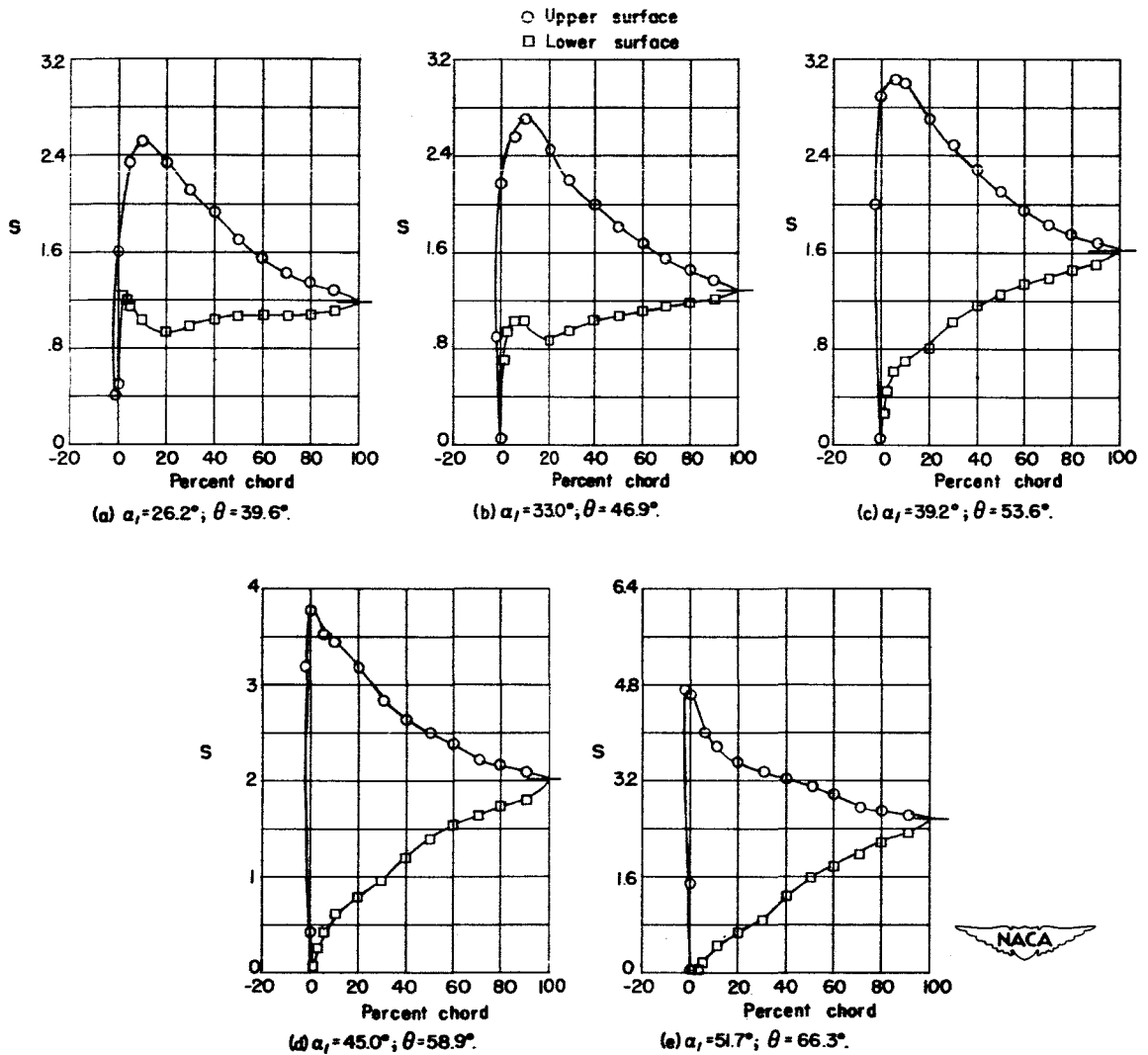
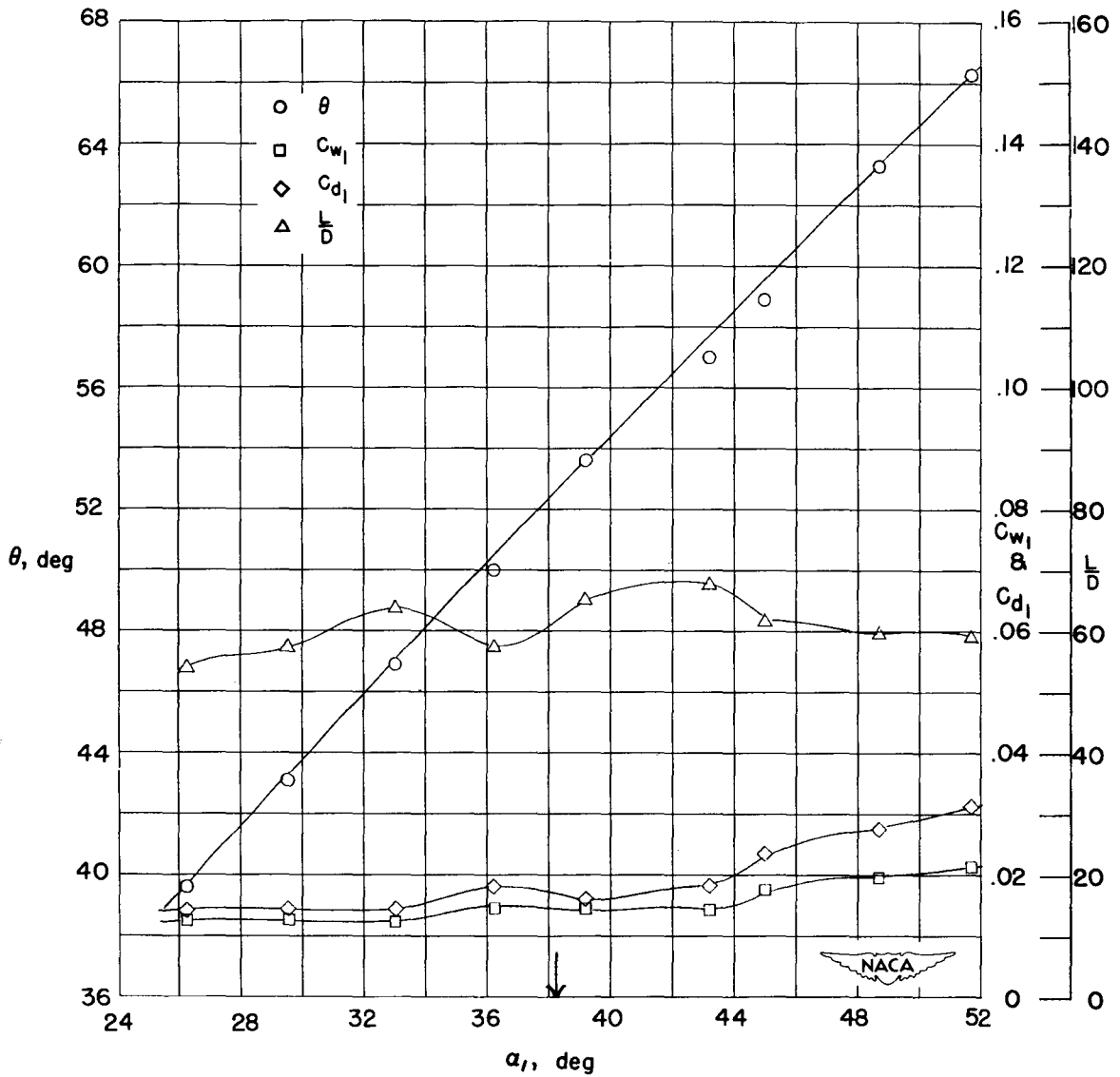


Figure 20.- Low-speed pressure distributions and section characteristics for the cascade combinations  $\beta_1 = 15^\circ$ ,  $\sigma = 1.8$ ,  $\theta_c = 65^\circ$ .



(f) Section characteristics; arrow shows design angle of attack.

Figure 20.- Concluded.

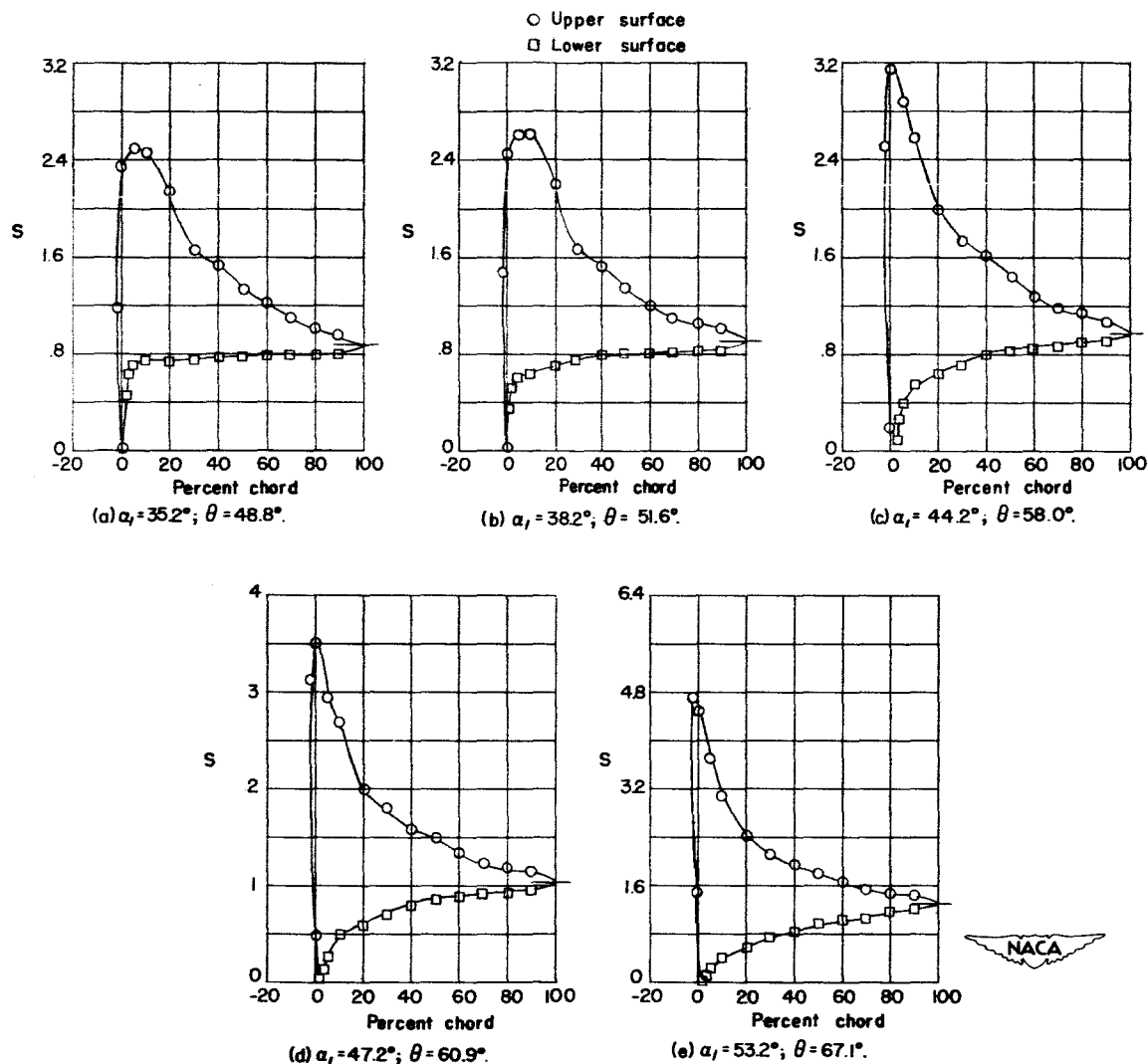
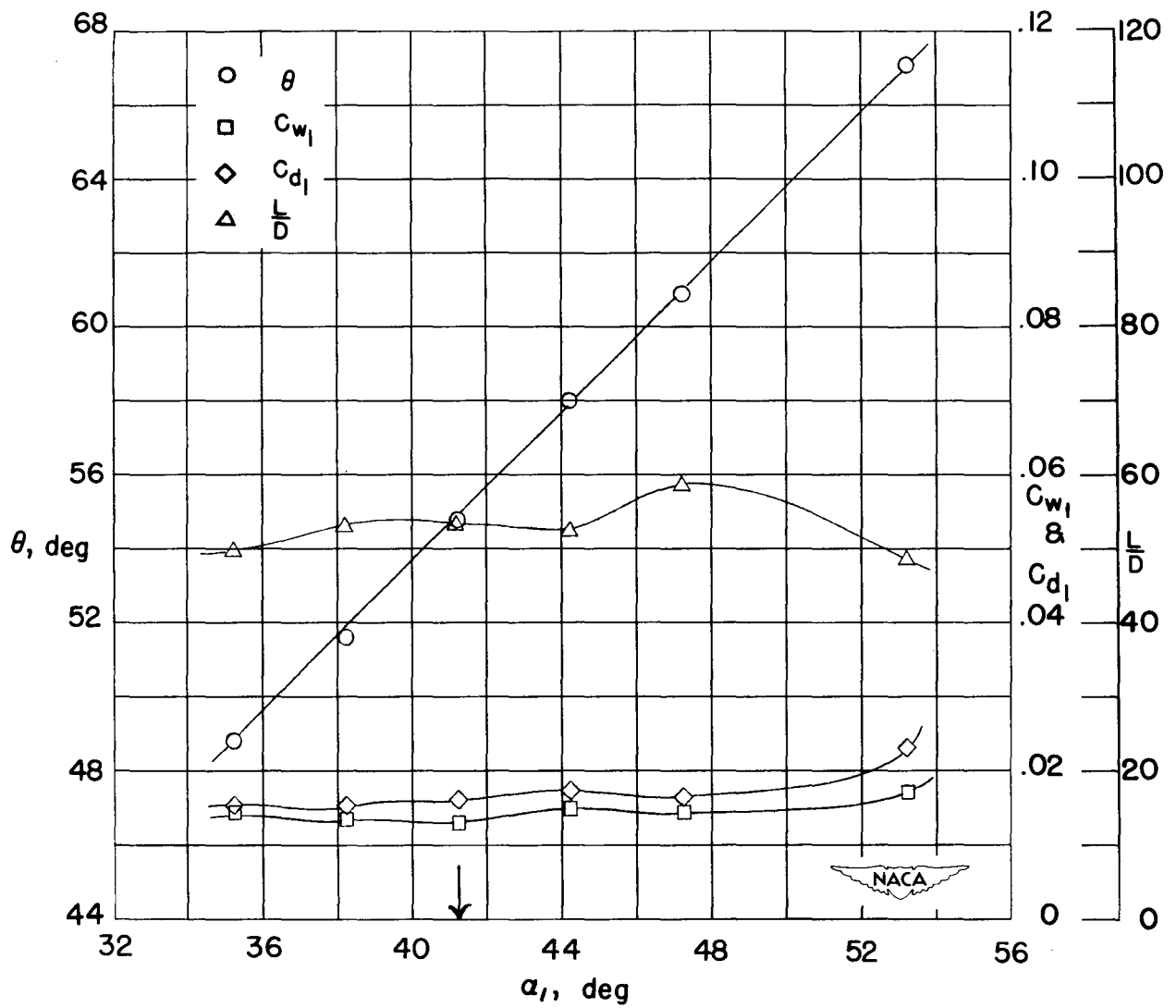


Figure 21.- Low-speed pressure distributions and section characteristics for the cascade combinations  $\beta_1 = 30^\circ$ ,  $\sigma = 1.8$ ,  $\theta_c = 65^\circ$ .





(f) Section characteristics; arrow shows design angle of attack.

Figure 21.- Concluded.

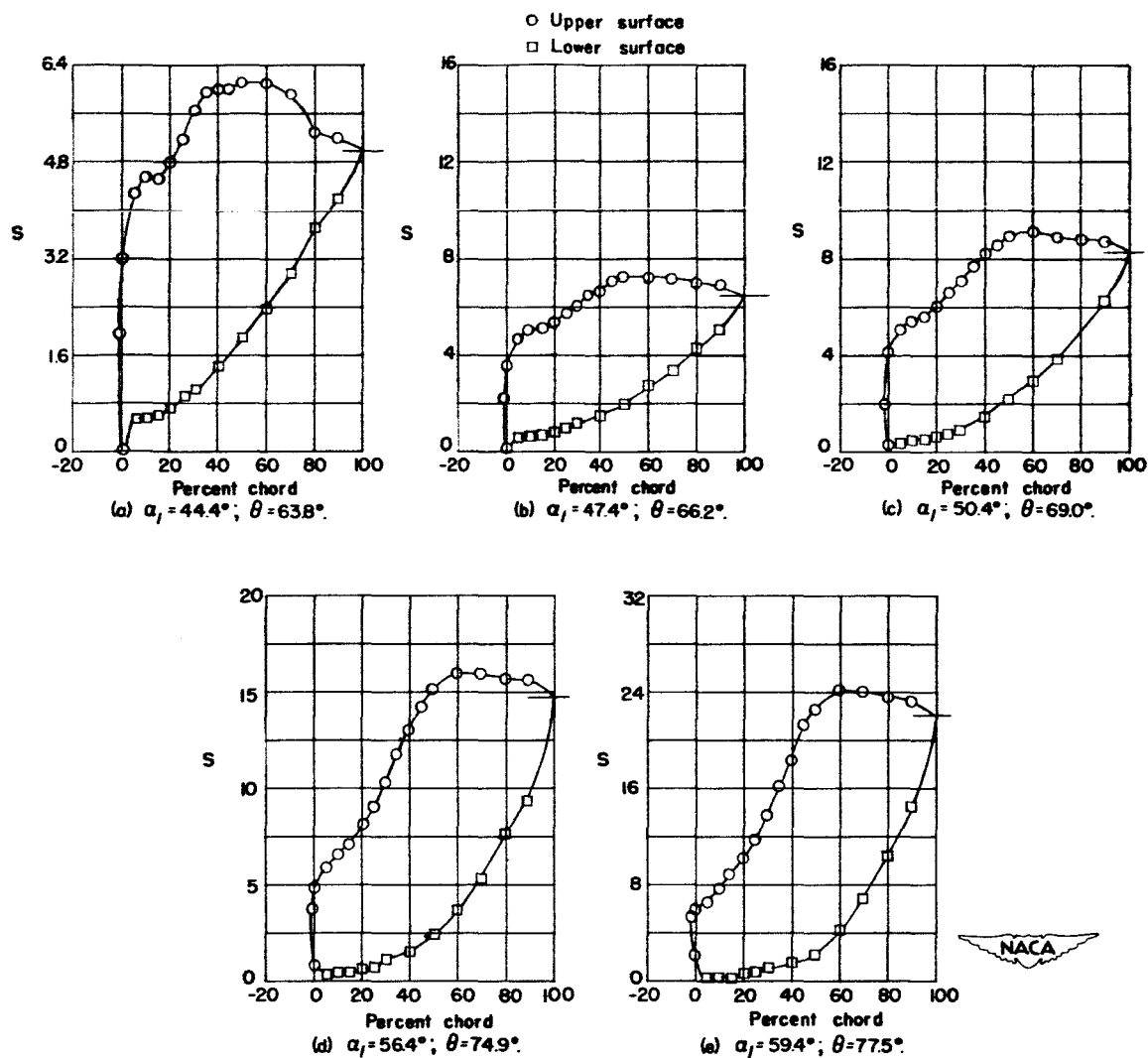
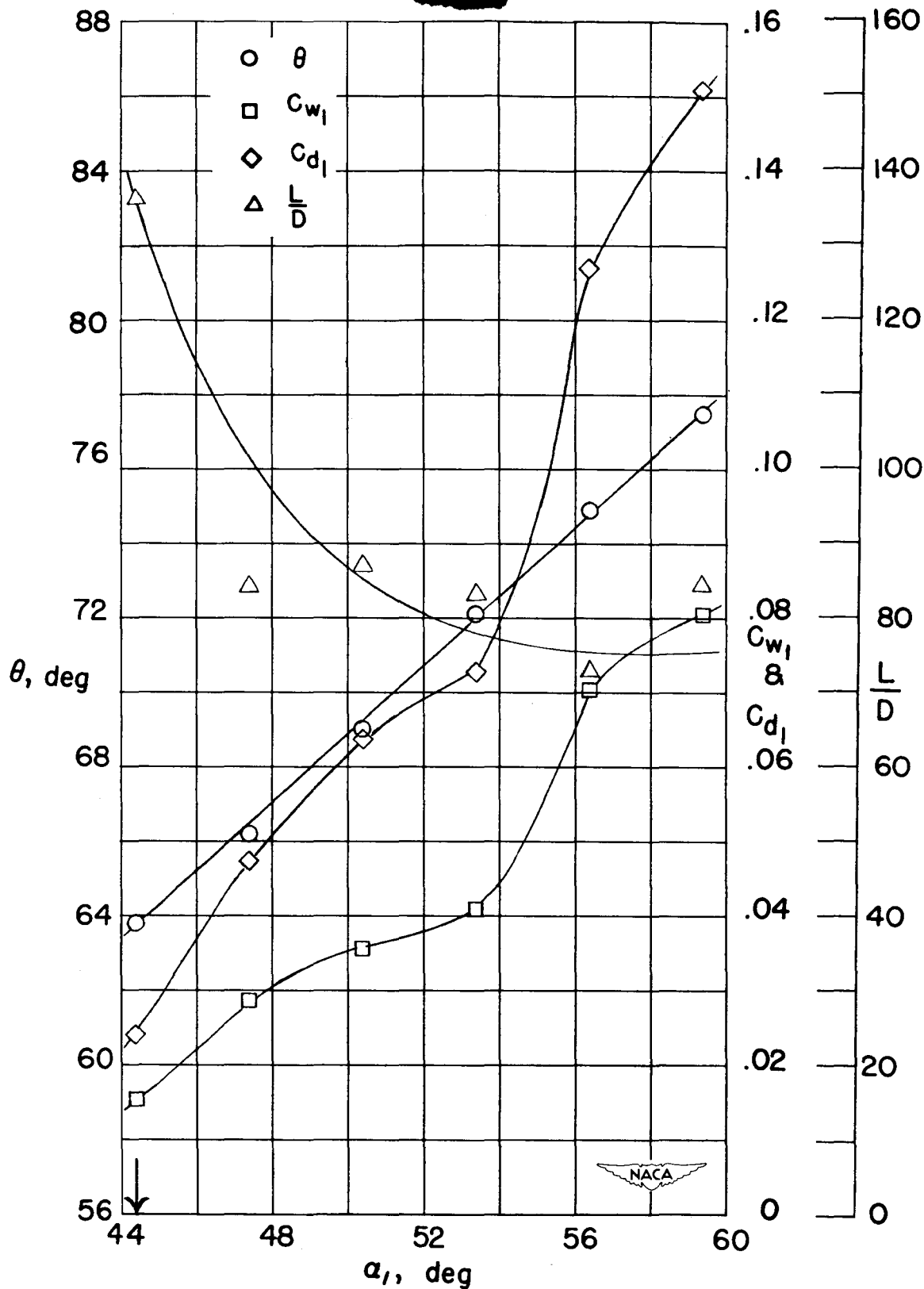


Figure 22.- Low-speed pressure distributions and section characteristics for the cascade combinations  $\beta_1 = 0^\circ$ ,  $\sigma = 1.8$ ,  $\theta_c = 80^\circ$ .



(f) Section characteristics; arrow shows design angle of attack.

Figure 22. - Concluded.

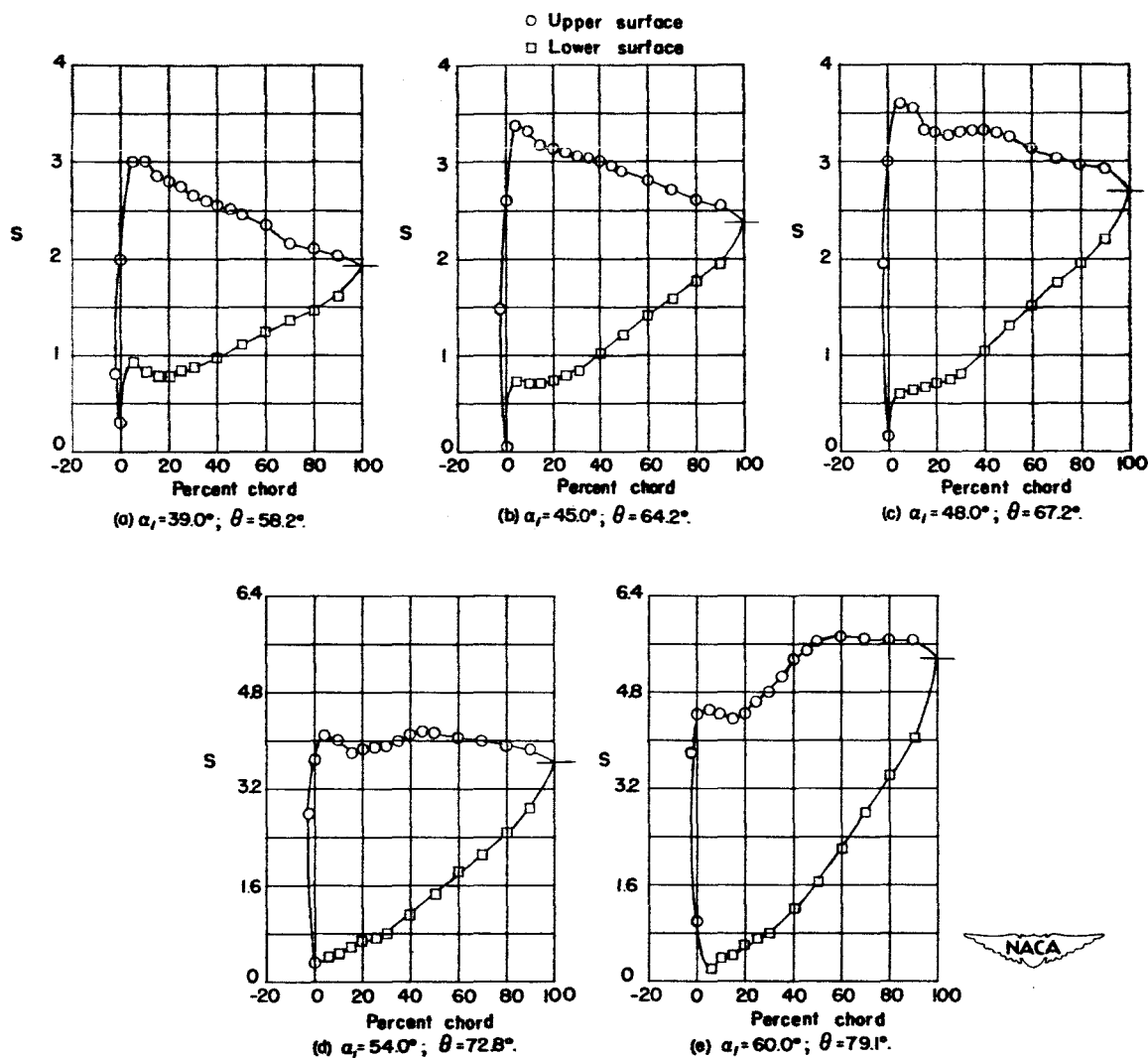
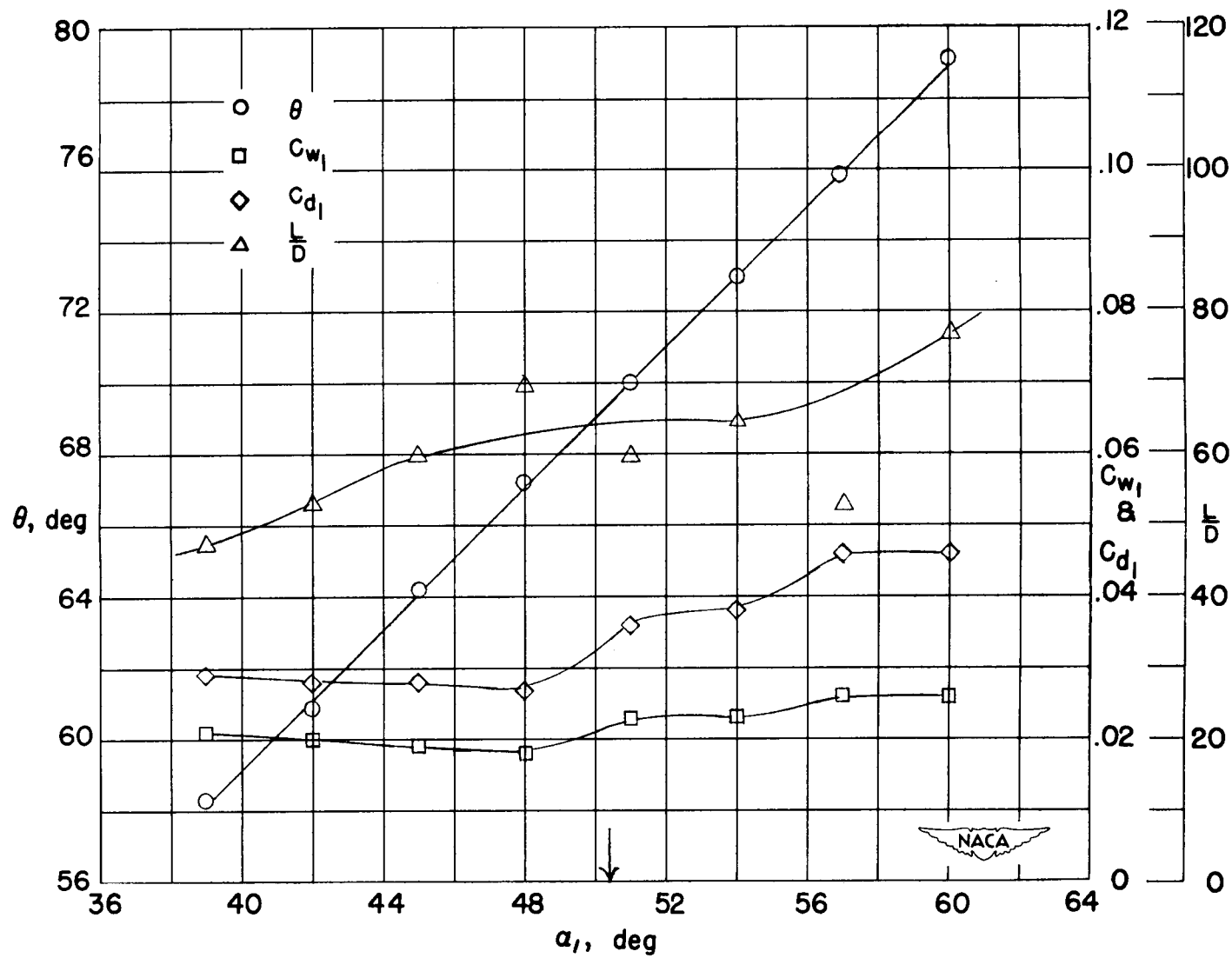


Figure 23.- Low-speed pressure distributions and section characteristics for the cascade combinations  $\beta_1 = 15^\circ$ ,  $\sigma = 1.8$ ,  $\theta_c = 80^\circ$ .



(f) Section characteristics; arrow shows design angle of attack.

Figure 23.- Concluded.

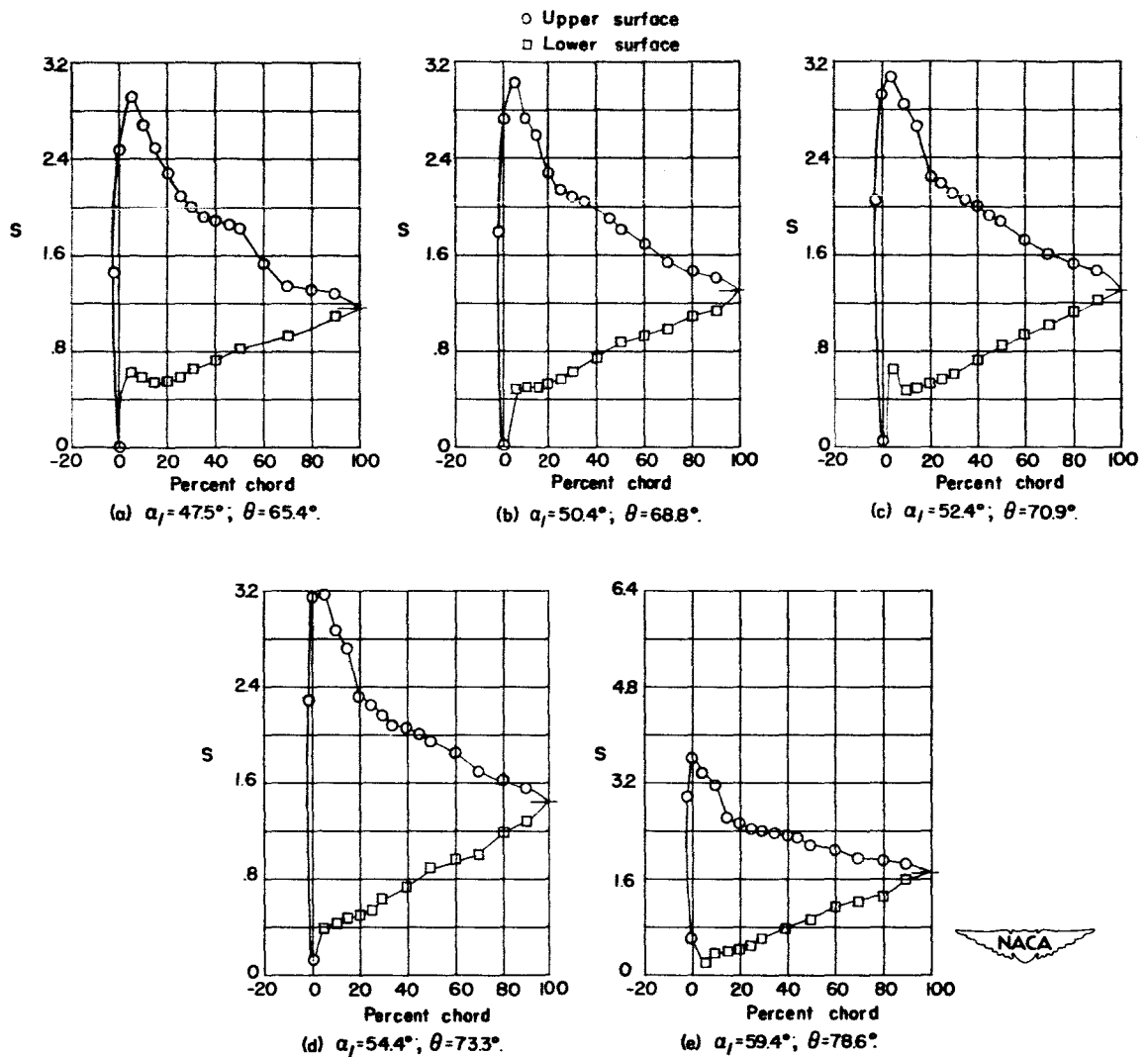
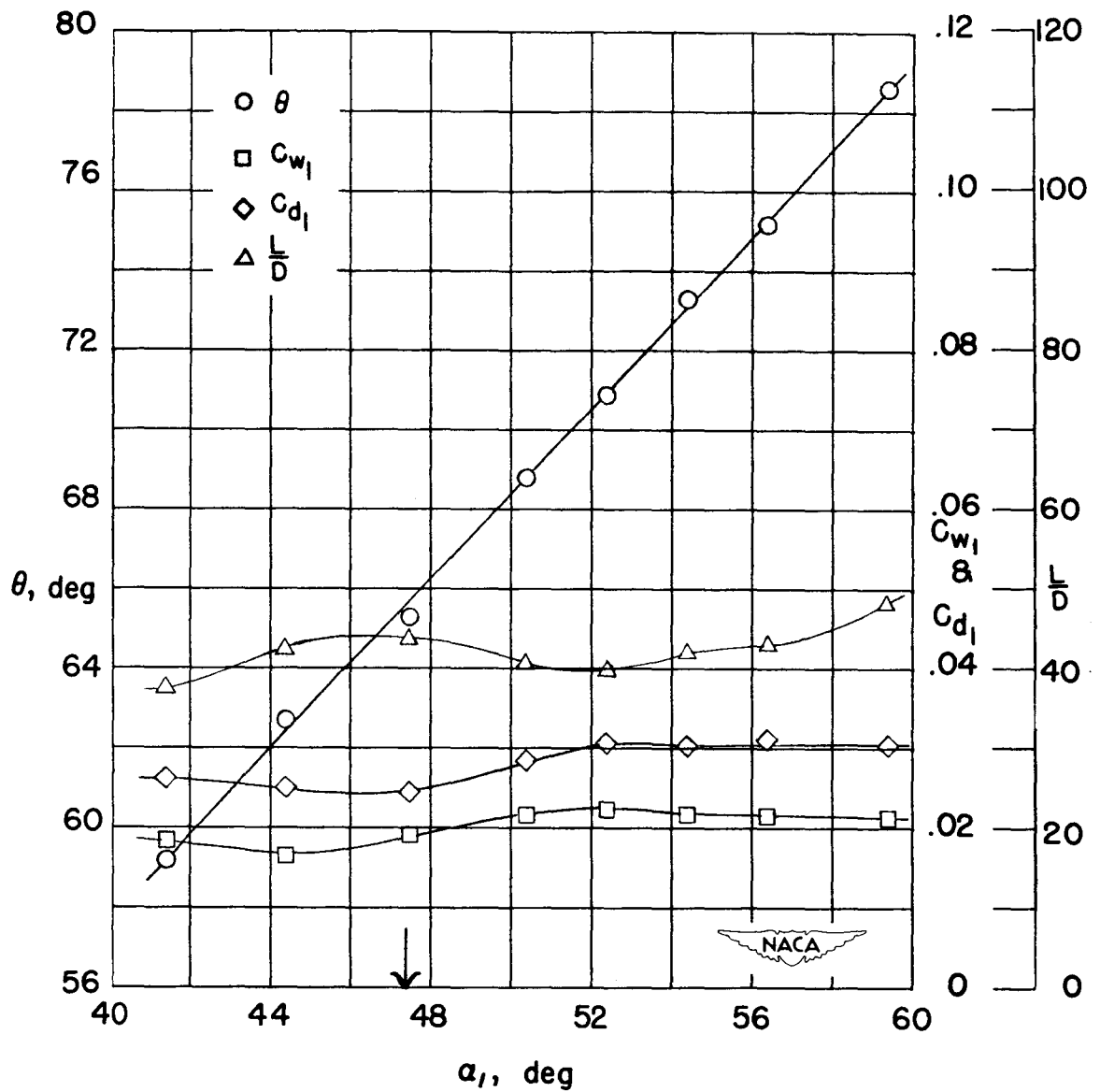


Figure 24.- Low-speed pressure distributions and section characteristics for the cascade combinations  $\beta_1 = 30^\circ$ ,  $\sigma = 1.8$ ,  $\theta_c = 80^\circ$ .



(f) Section characteristics; arrow shows design angle of attack.

Figure 24.- Concluded.

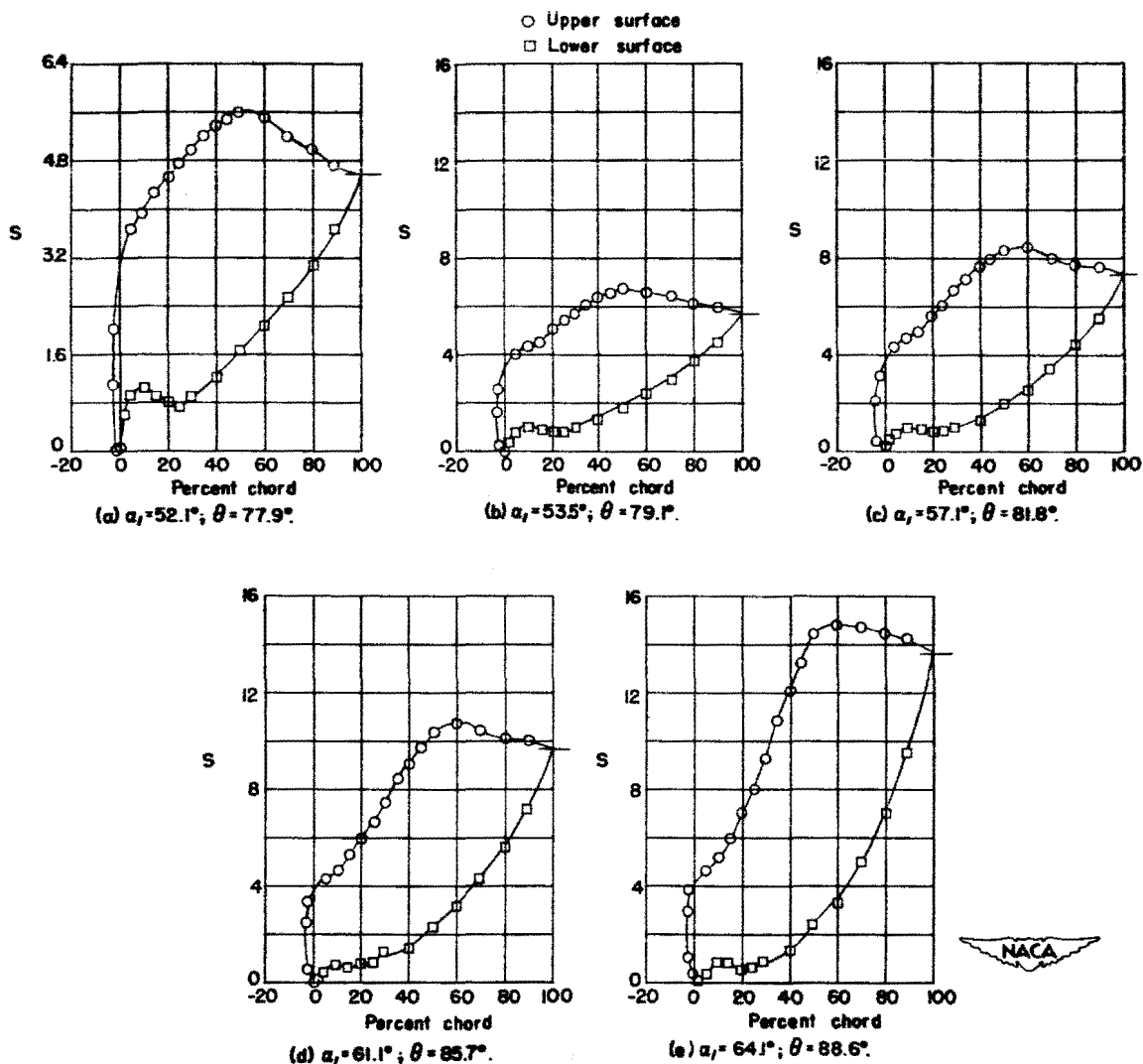
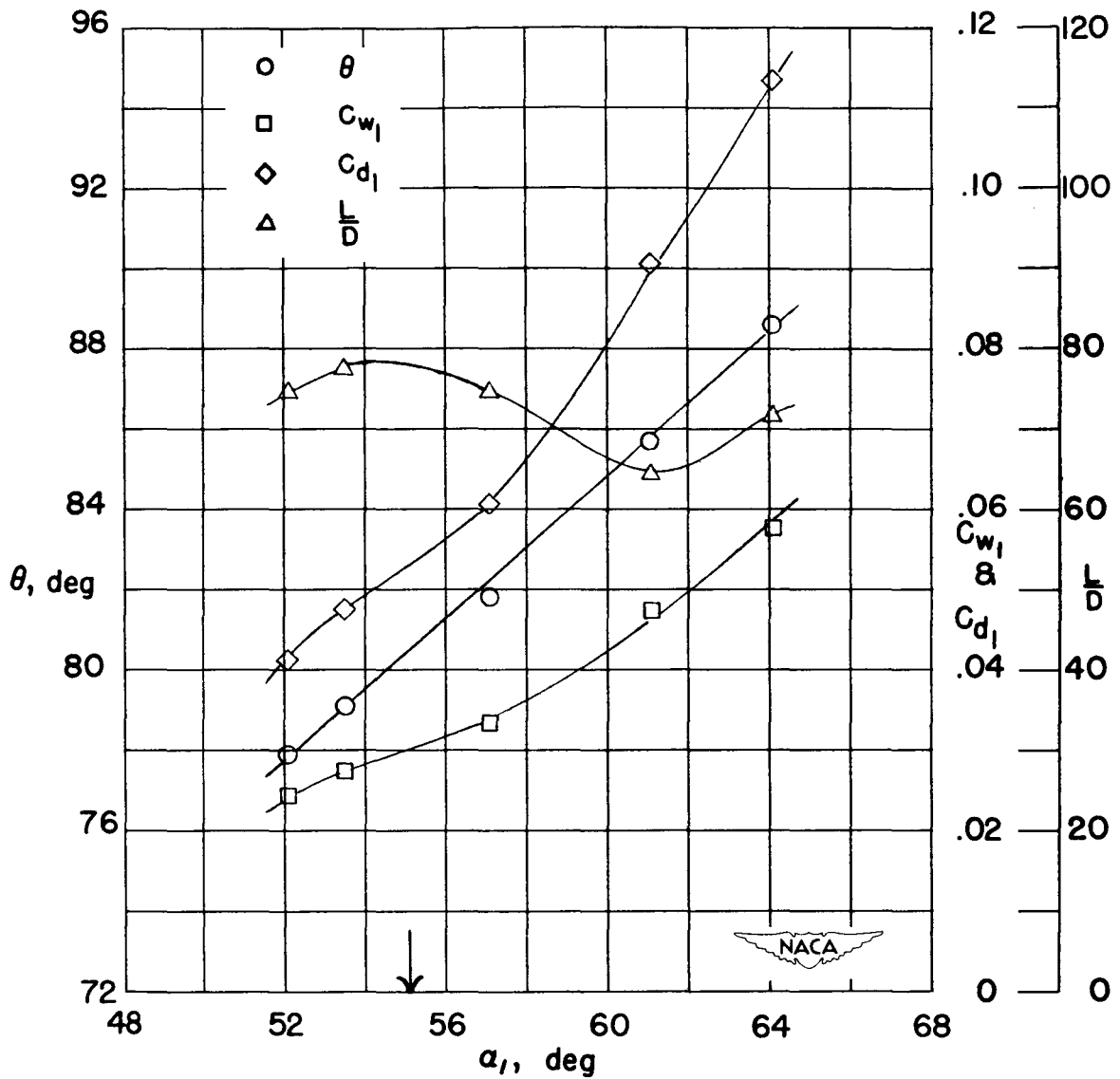


Figure 25.- Low-speed pressure distributions and section characteristics for the cascade combinations  $\beta_1 = 15^\circ$ ,  $\sigma = 1.8$ ,  $\theta_c = 95^\circ$ .





(f) Section characteristics; arrow shows design angle of attack.

Figure 25.- Concluded.

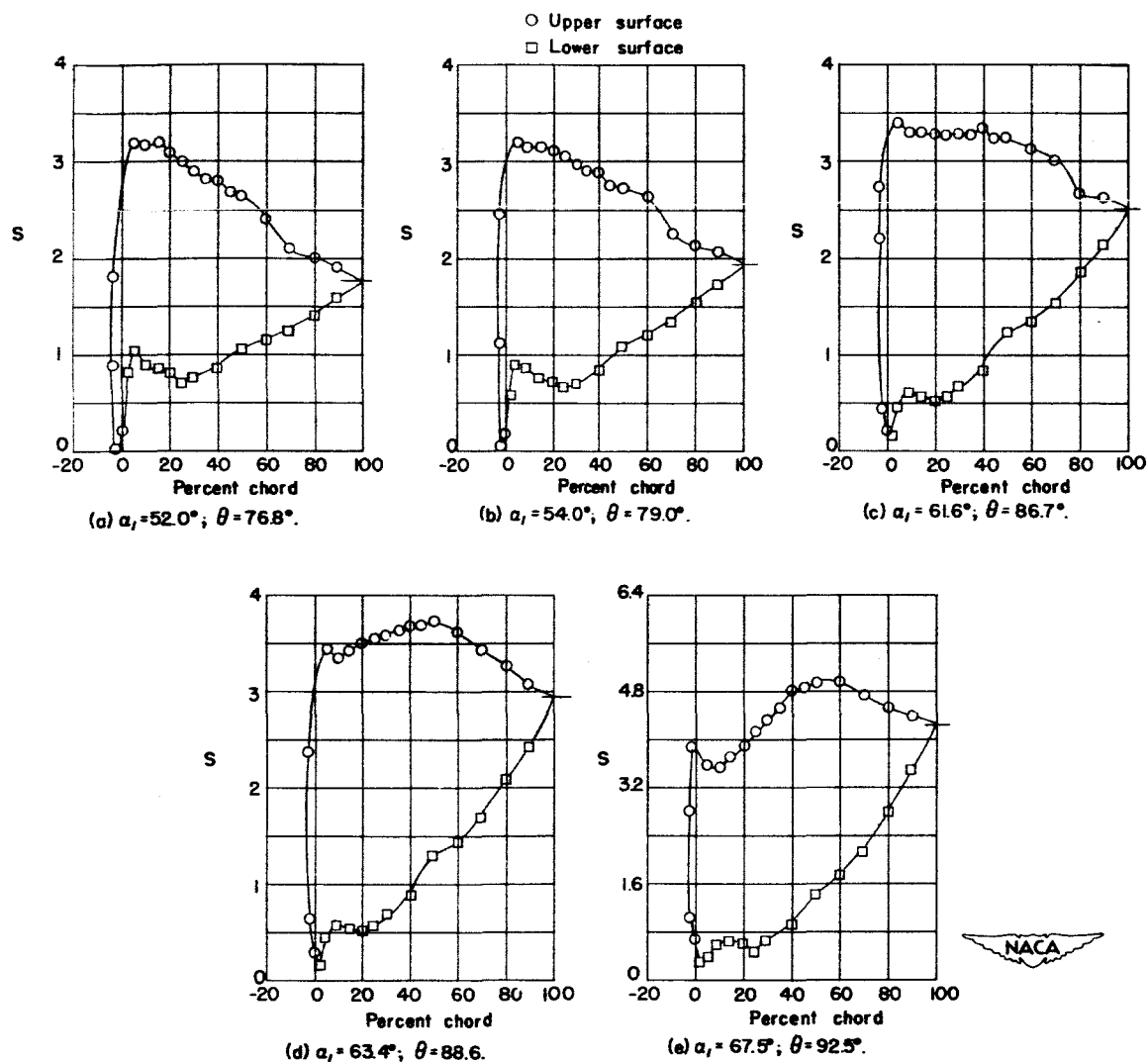
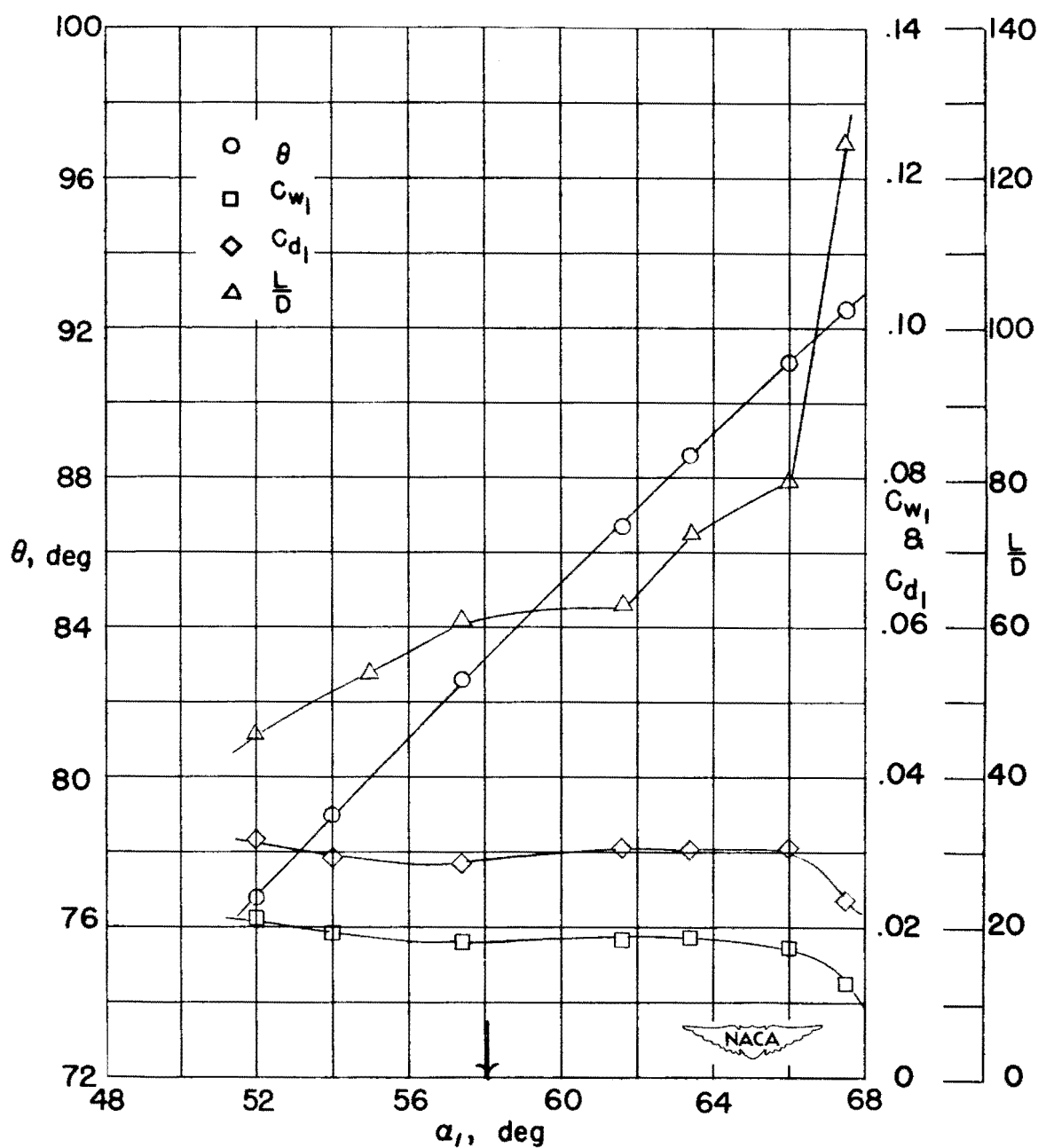


Figure 26.- Low-speed pressure distributions and section characteristics for the cascade combinations  $\beta_1 = 30^\circ$ ,  $\sigma = 1.8$ ,  $\theta_c = 95^\circ$ .



(f) Section characteristics; arrow shows design angle of attack.

Figure 26.- Concluded.

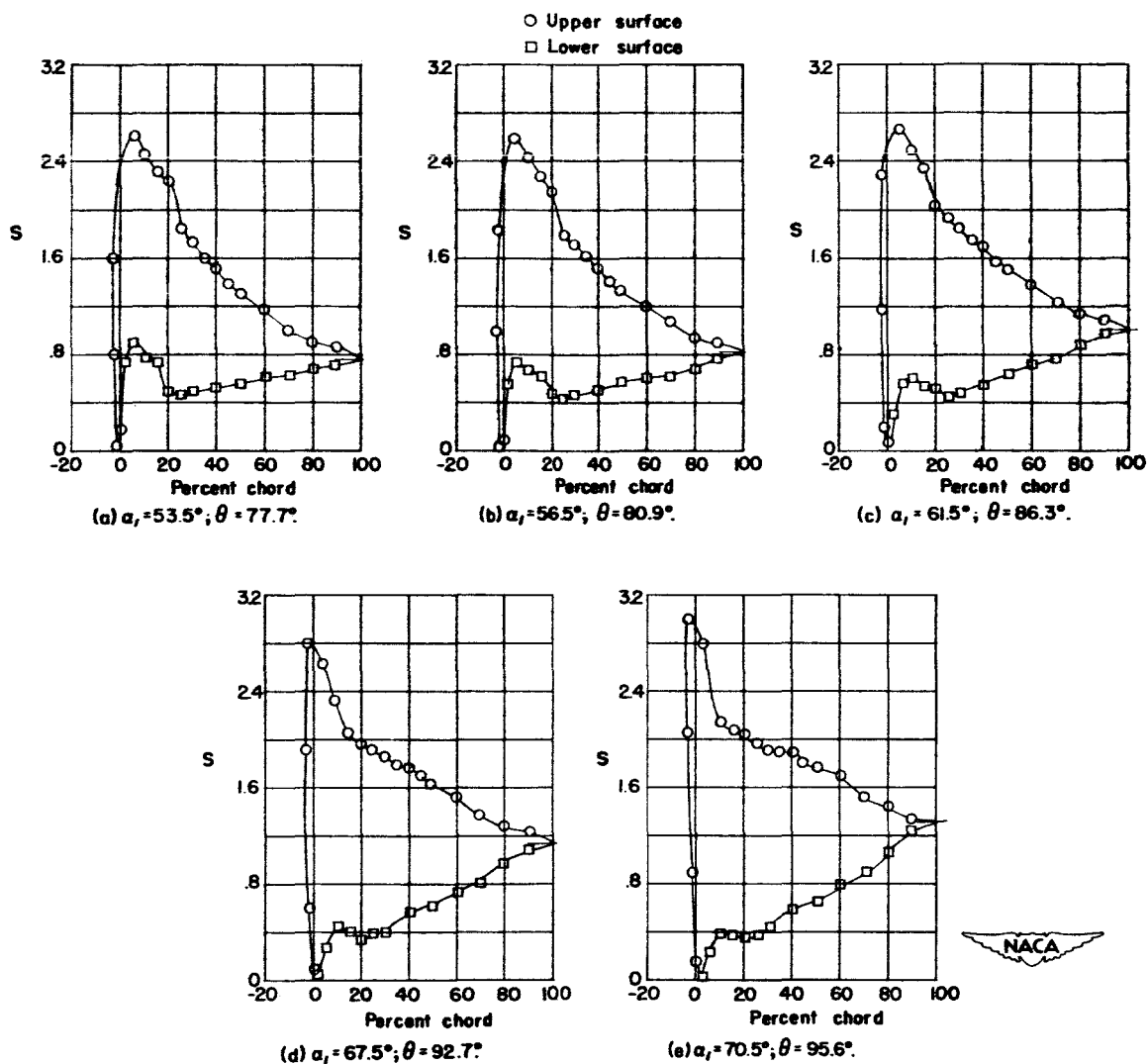
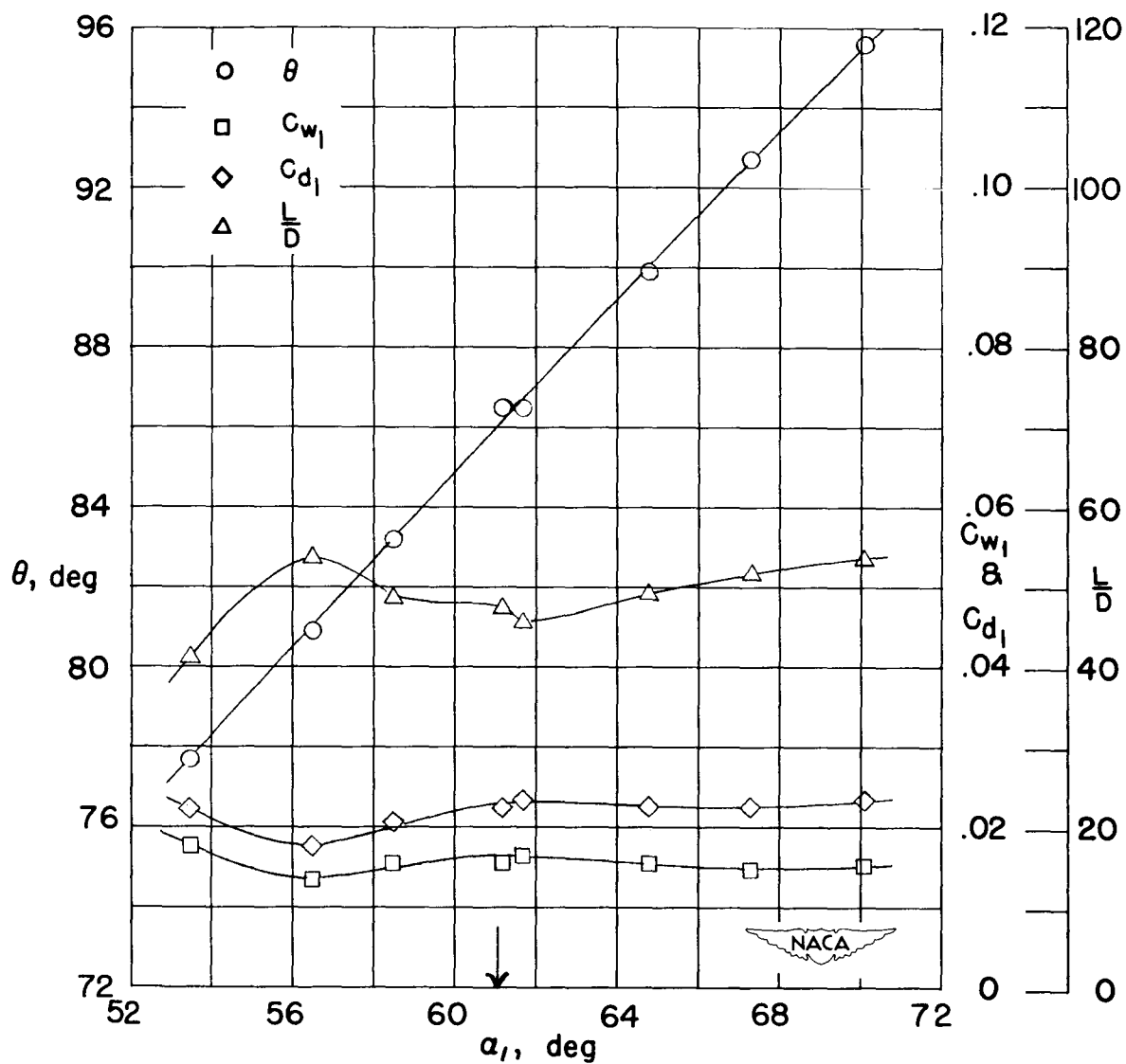


Figure 27.- Low-speed pressure distributions and section characteristics for the cascade combinations  $\beta_1 = 45^\circ$ ,  $\sigma = 1.8$ ,  $\theta_c = 95^\circ$ .



(f) Section characteristics; arrow shows design angle of attack.

Figure 27.- Concluded.

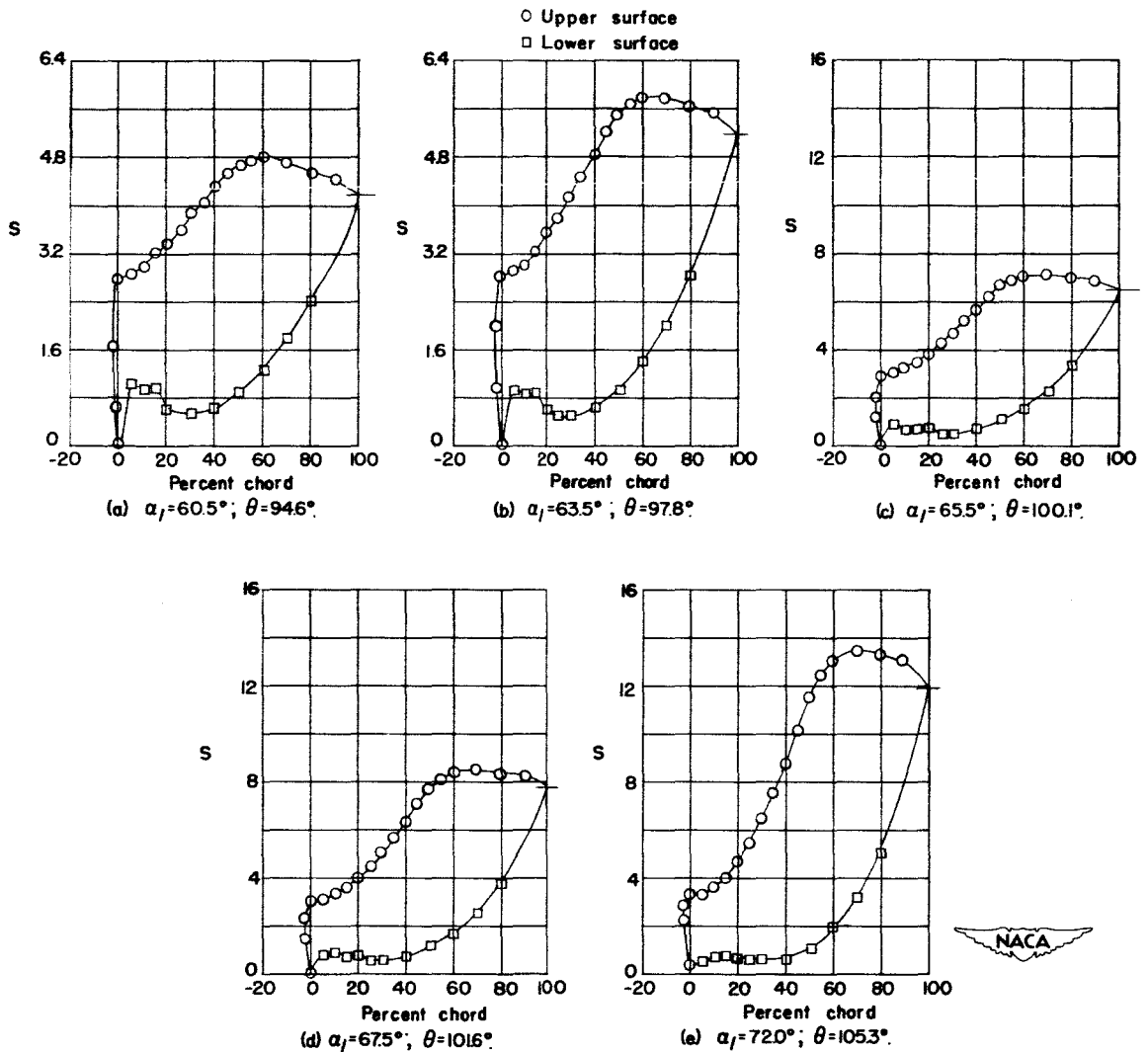
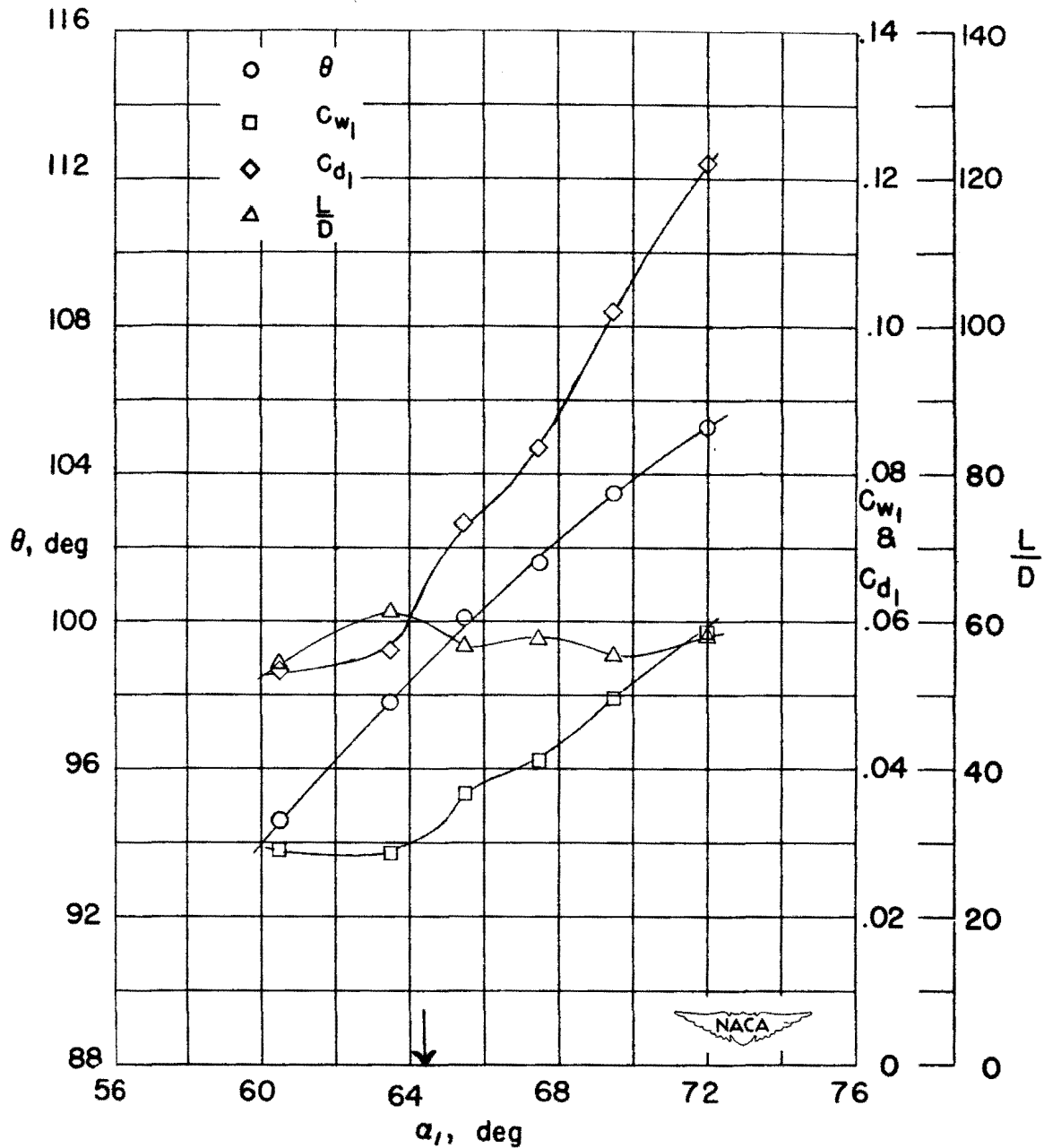


Figure 28.- Low-speed pressure distributions and section characteristics for the cascade combinations  $\beta_1 = 30^\circ$ ,  $\sigma = 1.8$ ,  $\theta_c = 110^\circ$ .



(f) Section characteristics; arrow shows design angle of attack.

Figure 28.- Concluded.

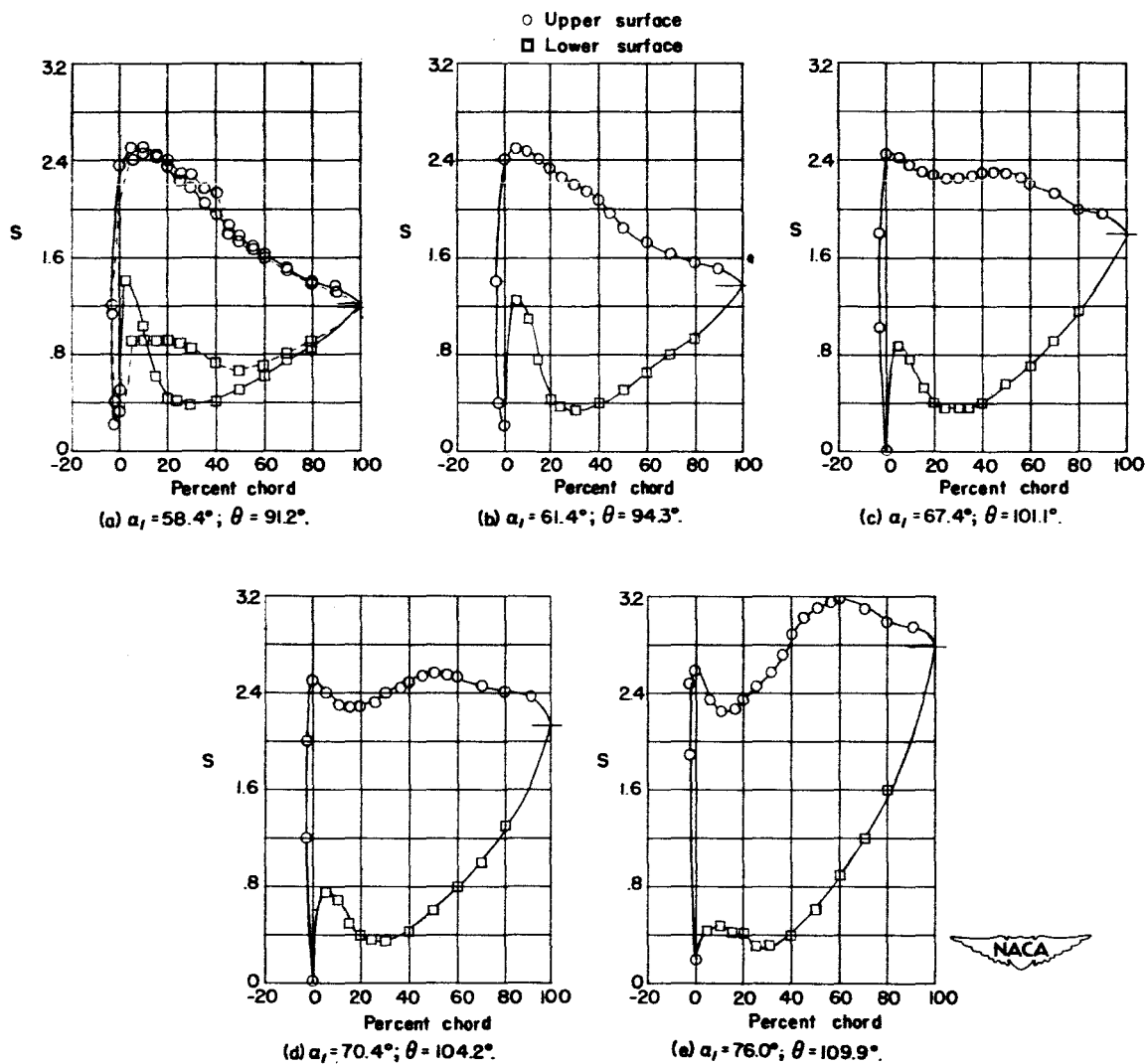
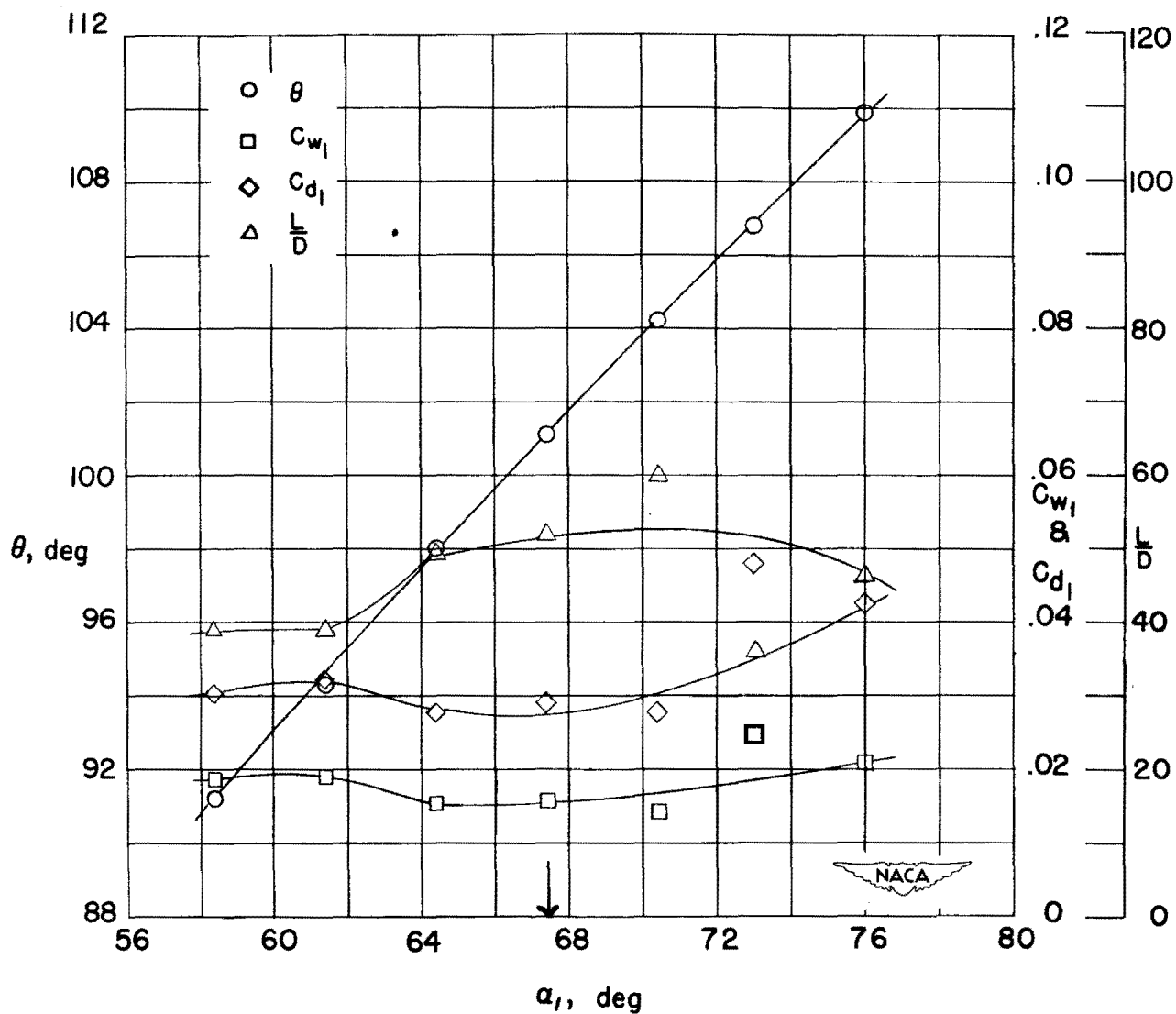


Figure 29.- Low-speed pressure distributions and section characteristics for the cascade combinations  $\beta_1 = 45^\circ$ ,  $\sigma = 1.8$ ,  $\theta_c = 110^\circ$ . Solid line indicates wire screen in throat. Dashed line indicates no screen.





(f) Section characteristics; arrow shows design angle of attack.

Figure 29.- Concluded.

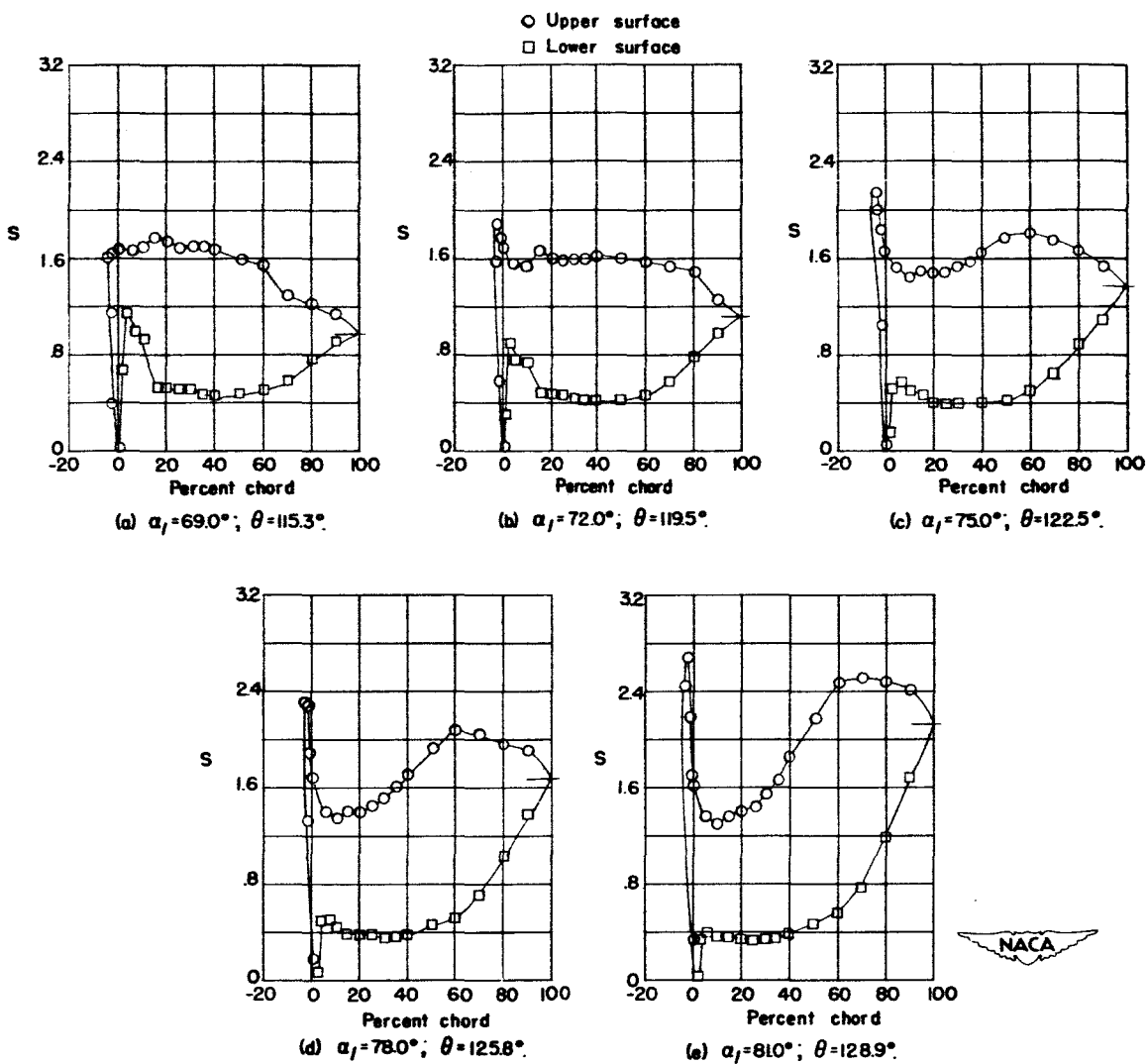
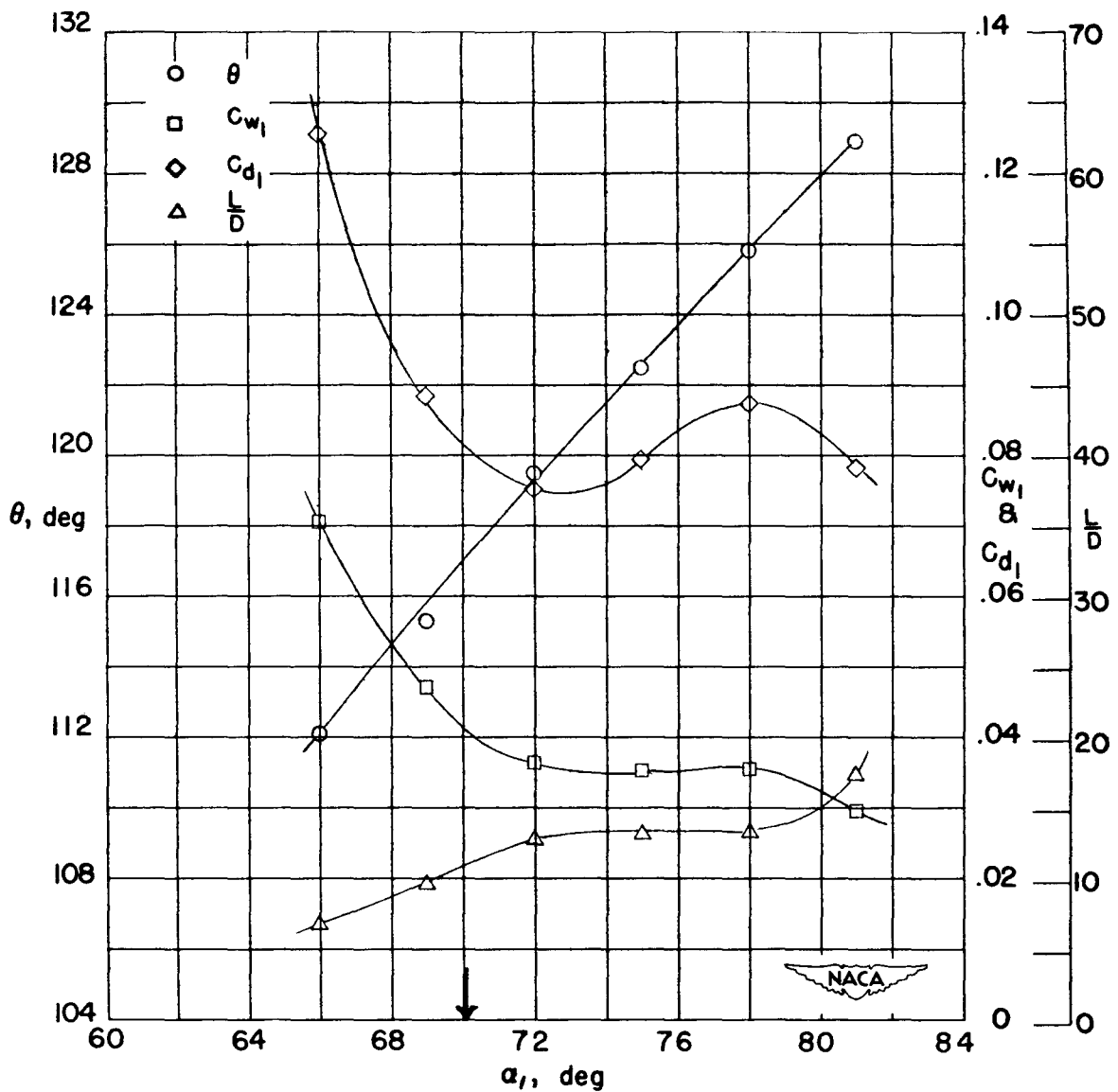
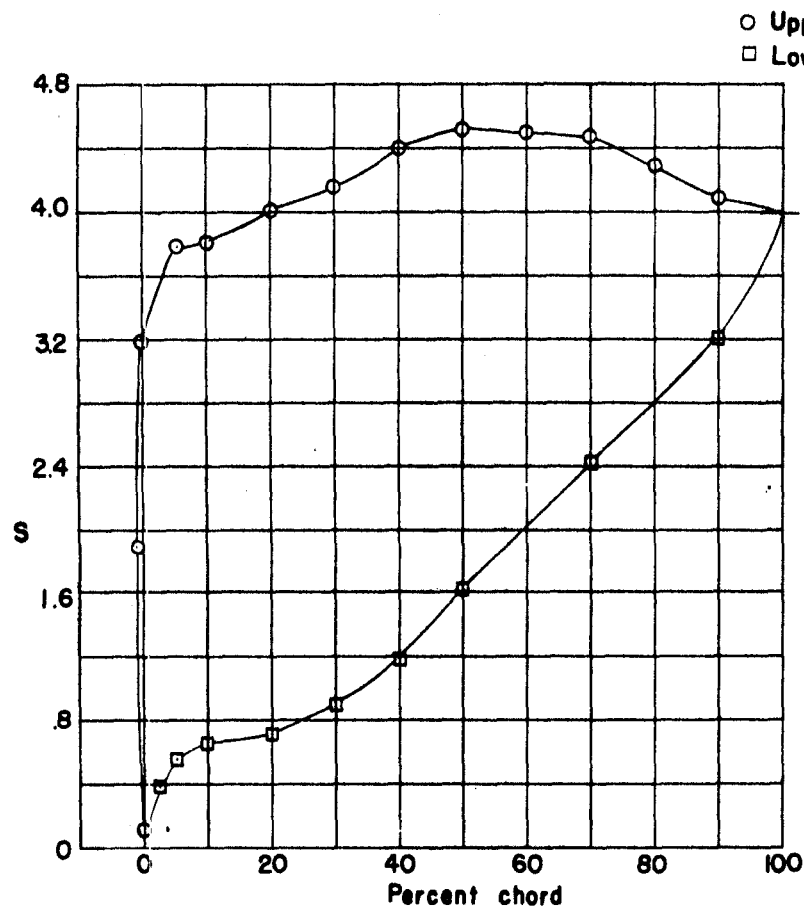


Figure 30.- Low-speed pressure distributions and section characteristics for the cascade combinations  $\beta_1 = 60^\circ$ ,  $\sigma = 1.8$ ,  $\theta_c = 120^\circ$ . Wire screen in throat.

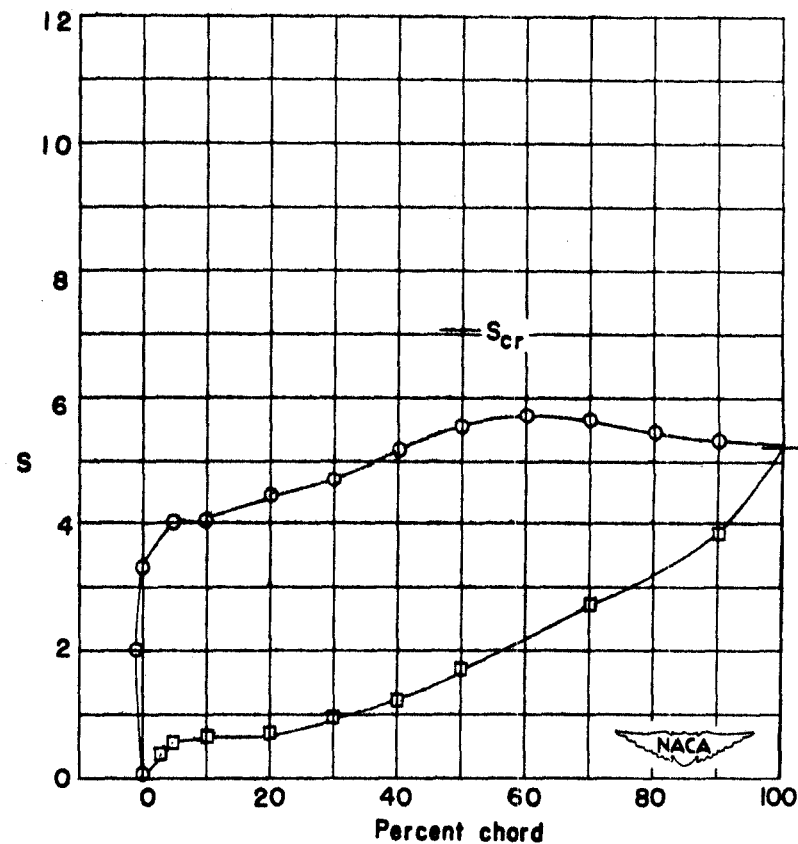


(f) Section characteristics; arrow shows design angle of attack.

Figure 30.- Concluded.

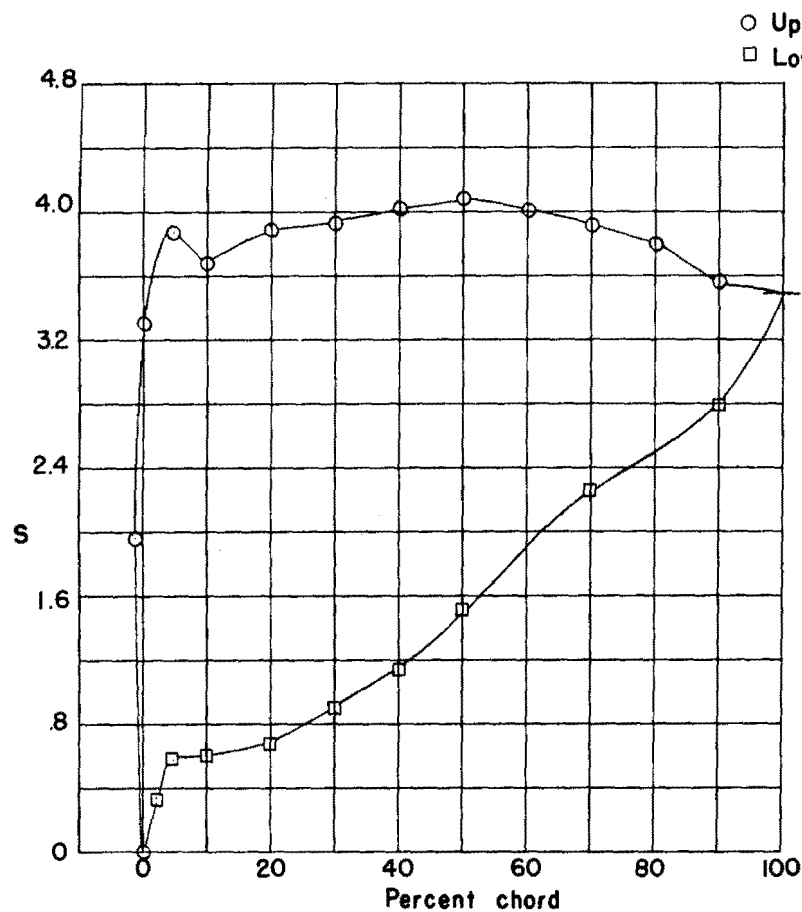


(a)  $M_1 = .245$ ;  $M_2 = .507$ ;  $C_{w1} = .0166$ ;  $\theta = 68.2^\circ$ .

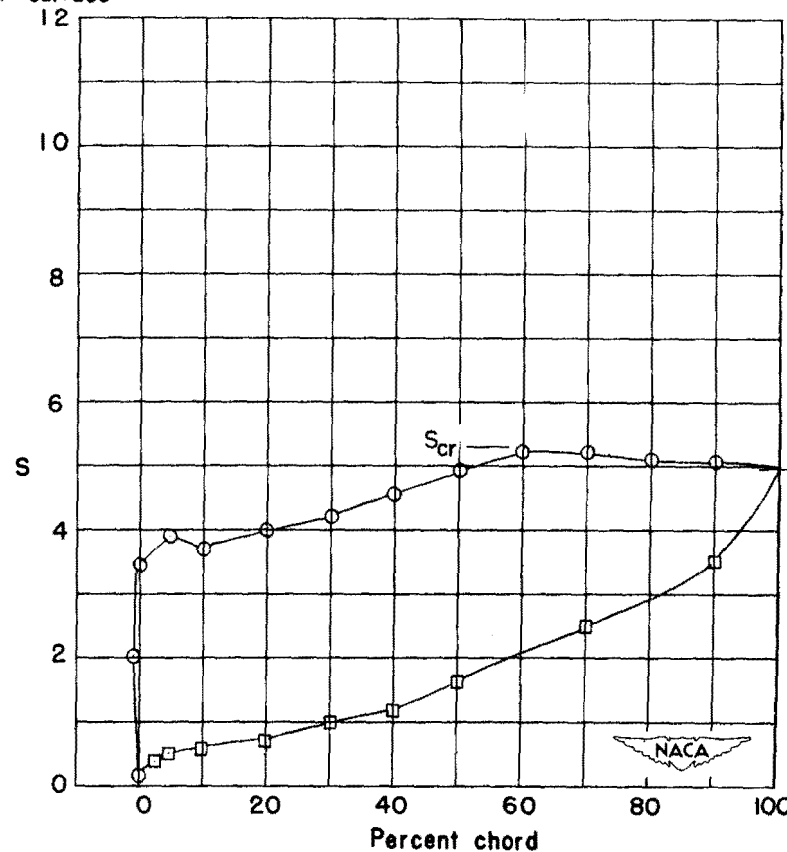


(b)  $M_1 = .319$ ;  $M_2 = .801$ ;  $C_{w1} = .0164$ ;  $\theta = 68.2^\circ$ .

Figure 31.- High-speed pressure distributions for cascade combinations  
 $\beta_1 = 10^\circ$ ,  $\alpha_1 = 48.4^\circ$ ,  $\theta_c = 80^\circ$ ,  $\sigma = 1.8$ .



(a)  $M_1 = .289$ ;  $M_2 = .561$ ;  $C_{w1} = .0202$ ;  $\theta = 70.5^\circ$ .



(b)  $M_1 = .374$ ;  $M_2 = .953$ ;  $C_{w1} = .0228$ ;  $\theta = 70.2^\circ$ .

Figure 32.- High-speed pressure distributions for cascade combinations  
 $\beta_1 = 15^\circ$ ,  $\alpha_1 = 50.4^\circ$ ,  $\theta_c = 80^\circ$ ,  $\sigma = 1.8$ .

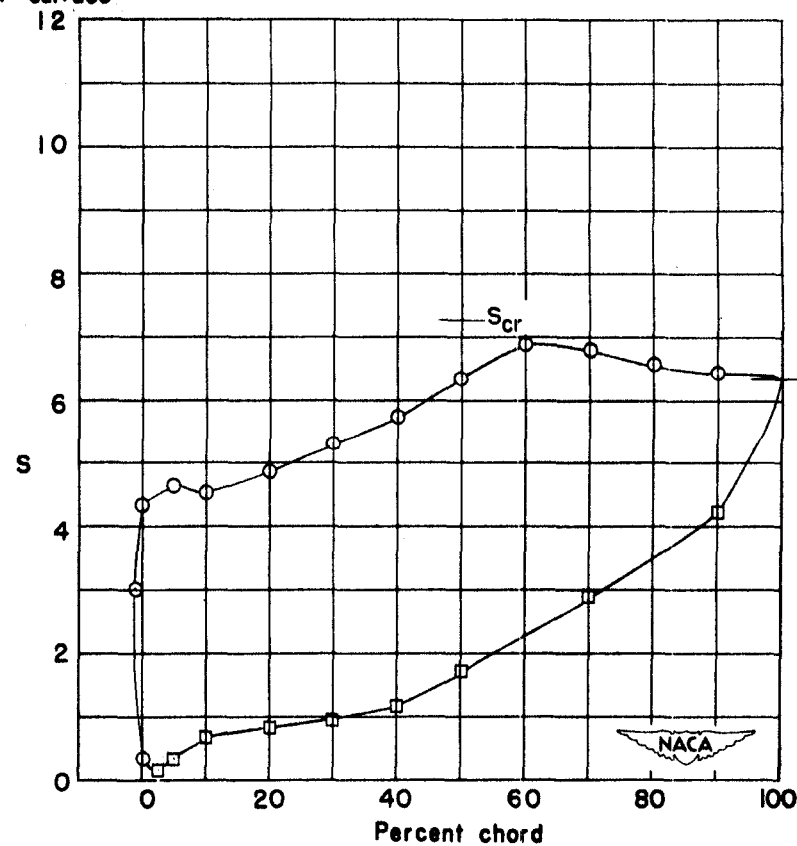
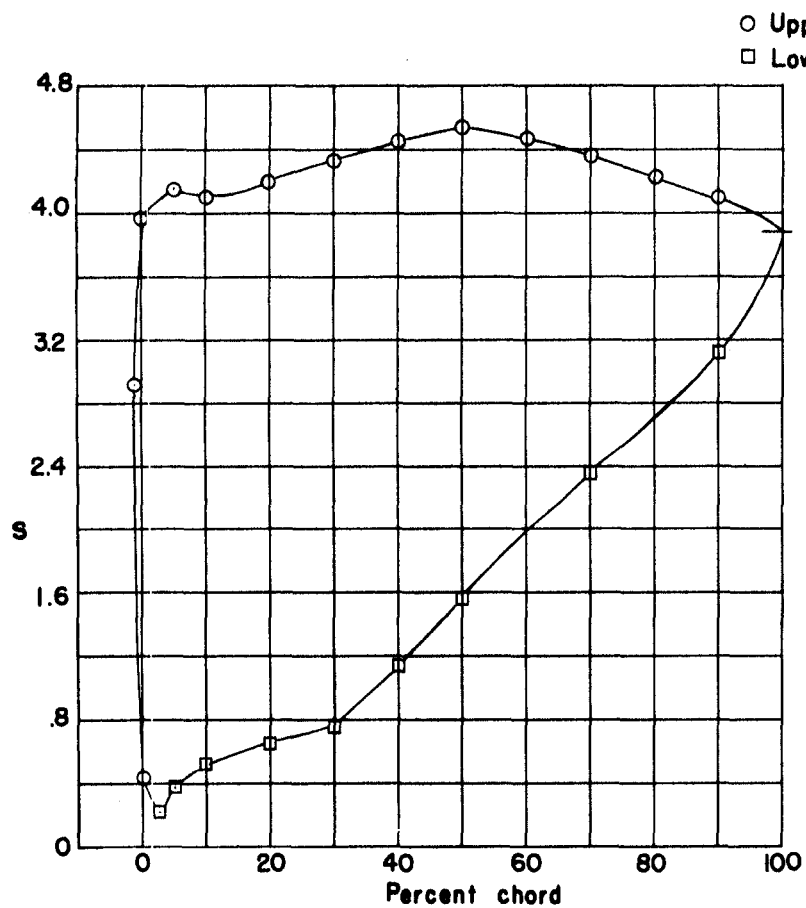


Figure 33.- High-speed pressure distributions for cascade combinations  
 $\beta_1 = 15^\circ$ ,  $\alpha_1 = 53.4^\circ$ ,  $\theta_c = 80^\circ$ ,  $\sigma = 1.8$ .

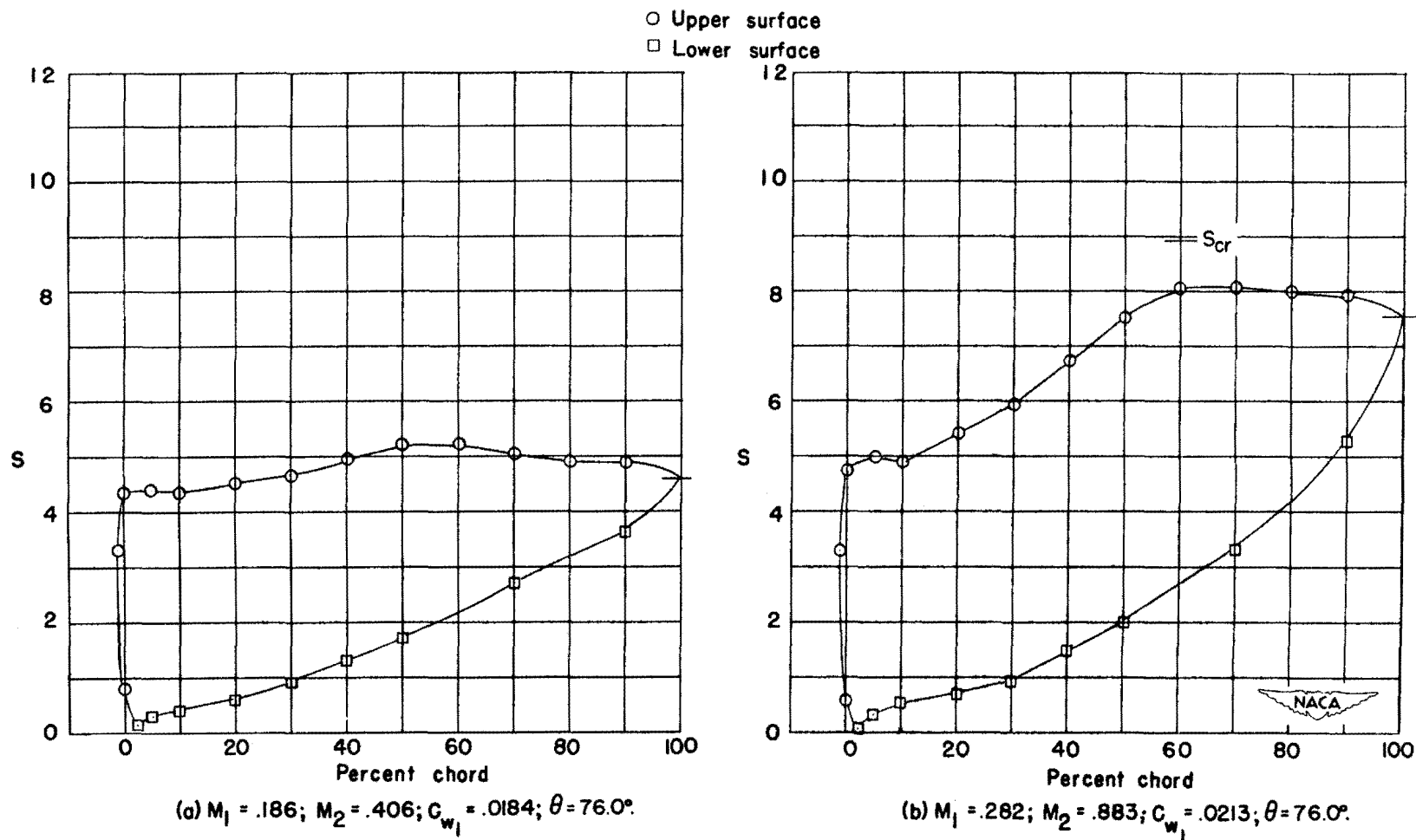
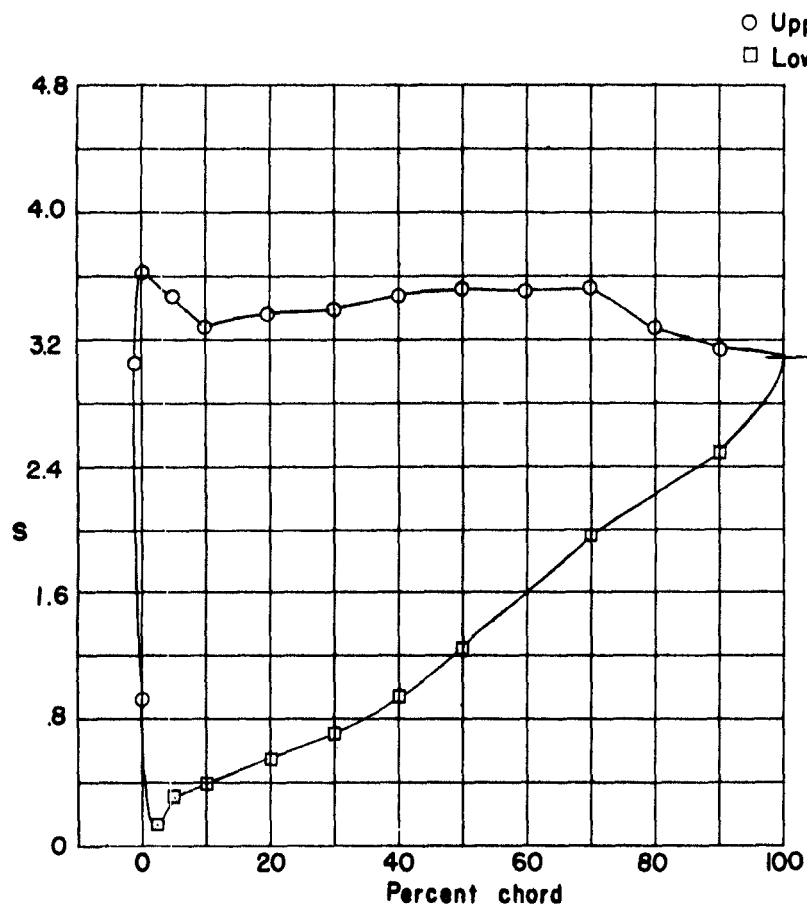
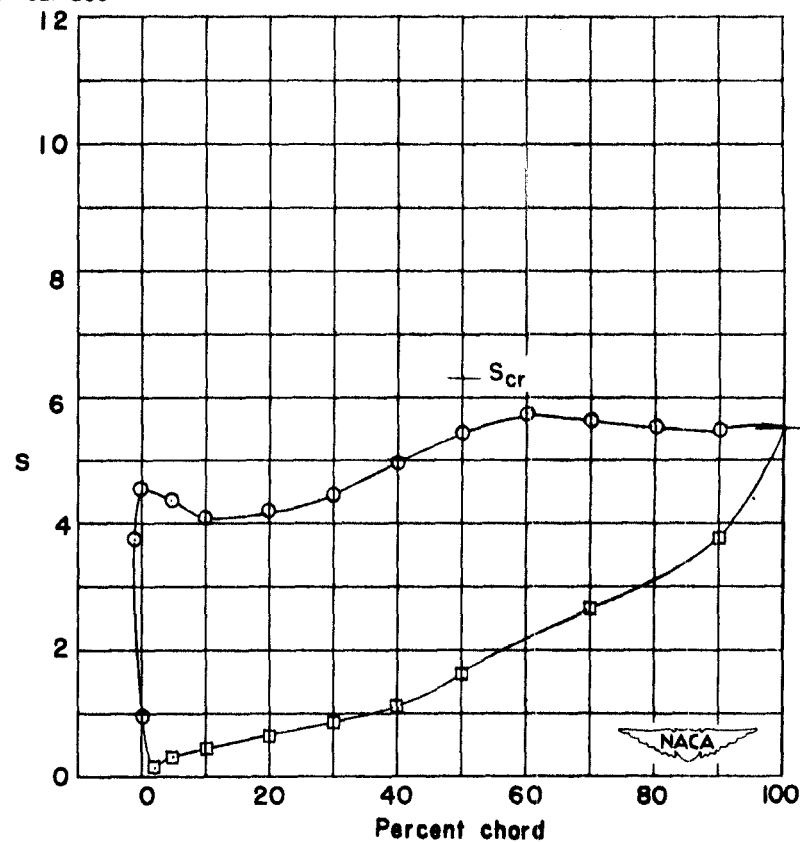


Figure 34.- High-speed pressure distributions for cascade combinations  
 $\beta_1 = 15^\circ$ ,  $\alpha_1 = 56.4^\circ$ ,  $\theta_c = 80^\circ$ ,  $\sigma = 1.8$ .



(a)  $M_1 = .224$ ;  $M_2 = .402$ ;  $C_{w1} = .0162$ ;  $\theta = 78.1^\circ$ .



(b)  $M_1 = .340$ ;  $M_2 = .906$ ;  $C_{w1} = .0219$ ;  $\theta = 78.3^\circ$ .

Figure 35.- High-speed pressure distributions for cascade combinations  
 $\beta_1 = 20^\circ$ ,  $\alpha_1 = 58.4^\circ$ ,  $\theta_c = 80^\circ$ ,  $\sigma = 1.8$ .



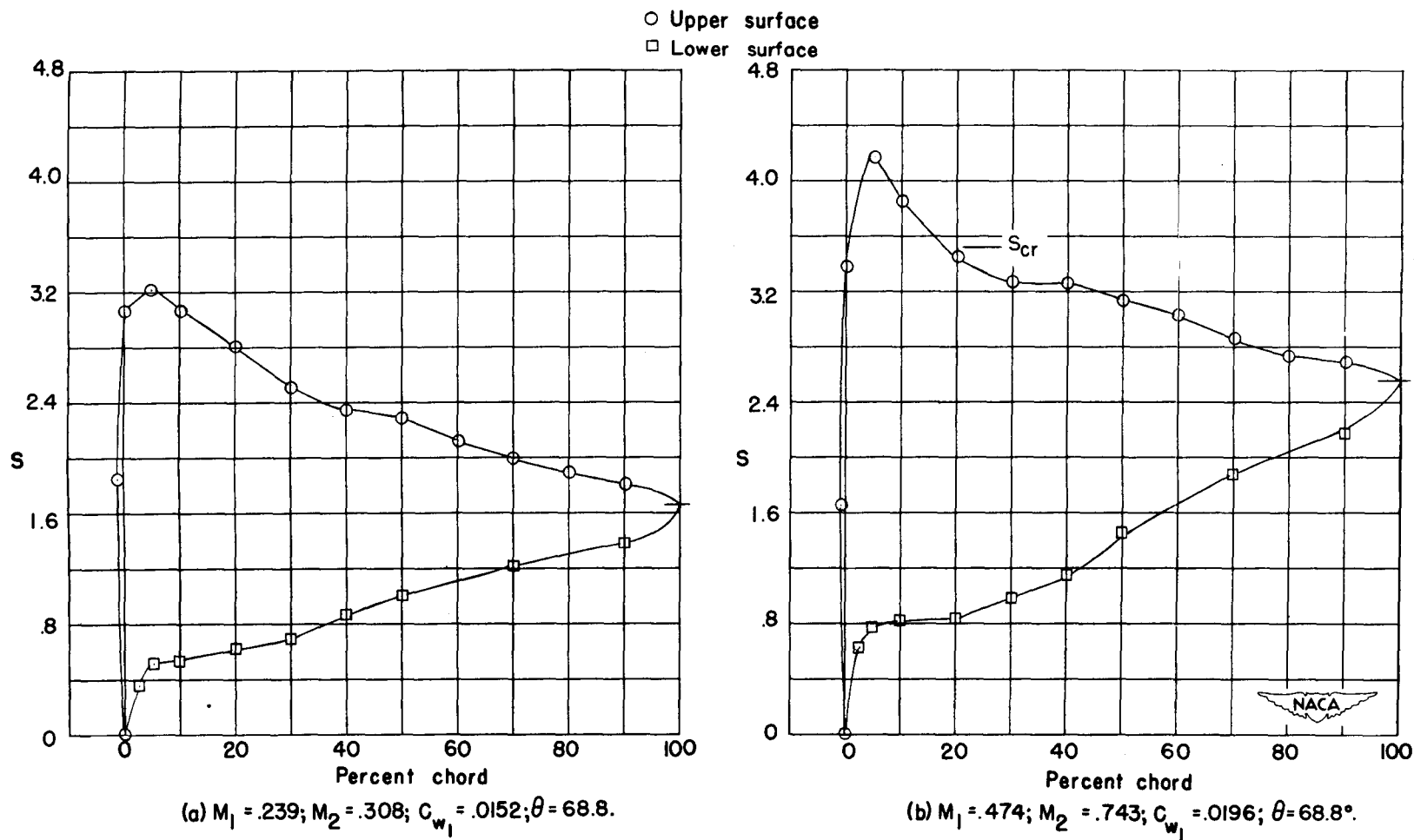
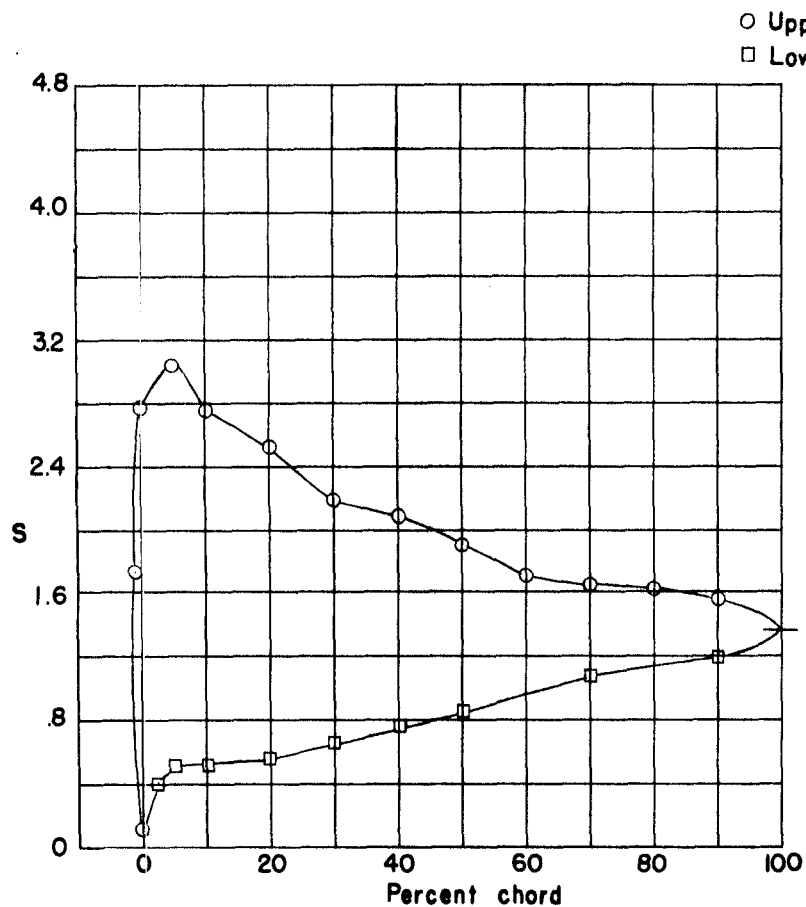
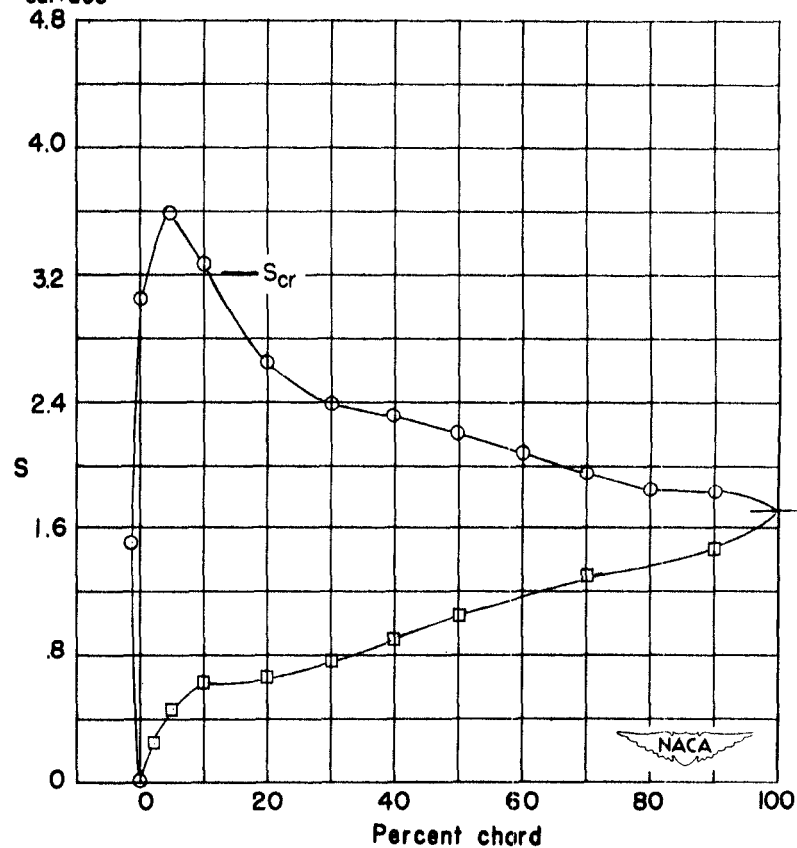


Figure 36.- High-speed pressure distributions for cascade combinations  
 $\beta_1 = 25^\circ$ ,  $\alpha_1 = 48.4^\circ$ ,  $\theta_c = 80^\circ$ ,  $\sigma = 1.8$ .

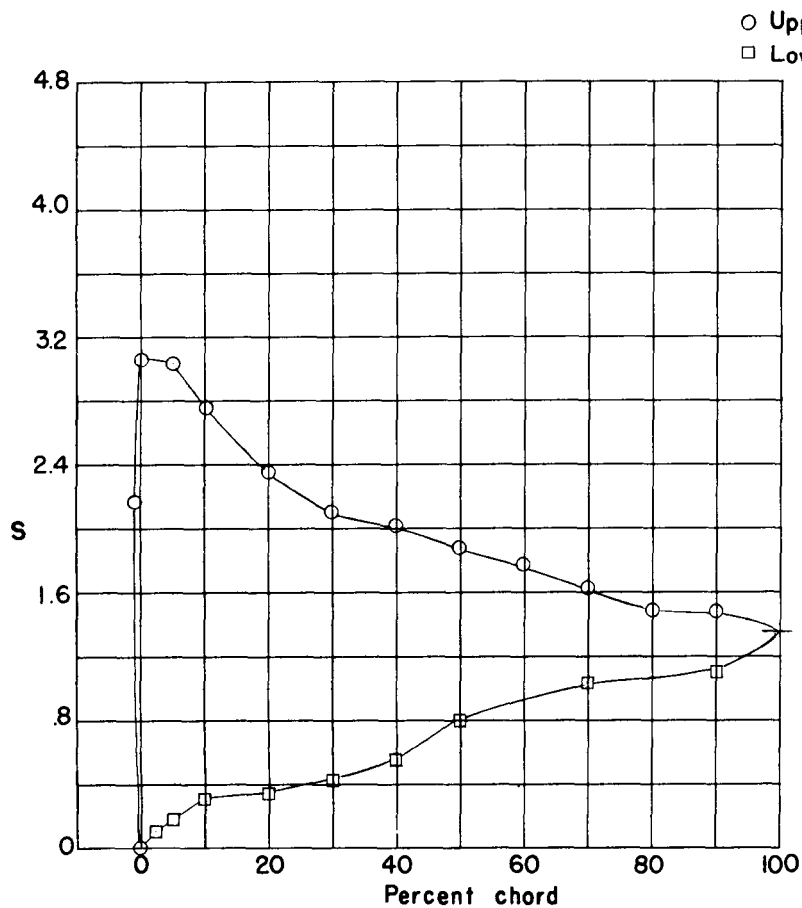


(a)  $M_1 = .186$ ;  $M_2 = .218$ ;  $C_{w1} = .0153$ ;  $\theta = 71.0^\circ$ .

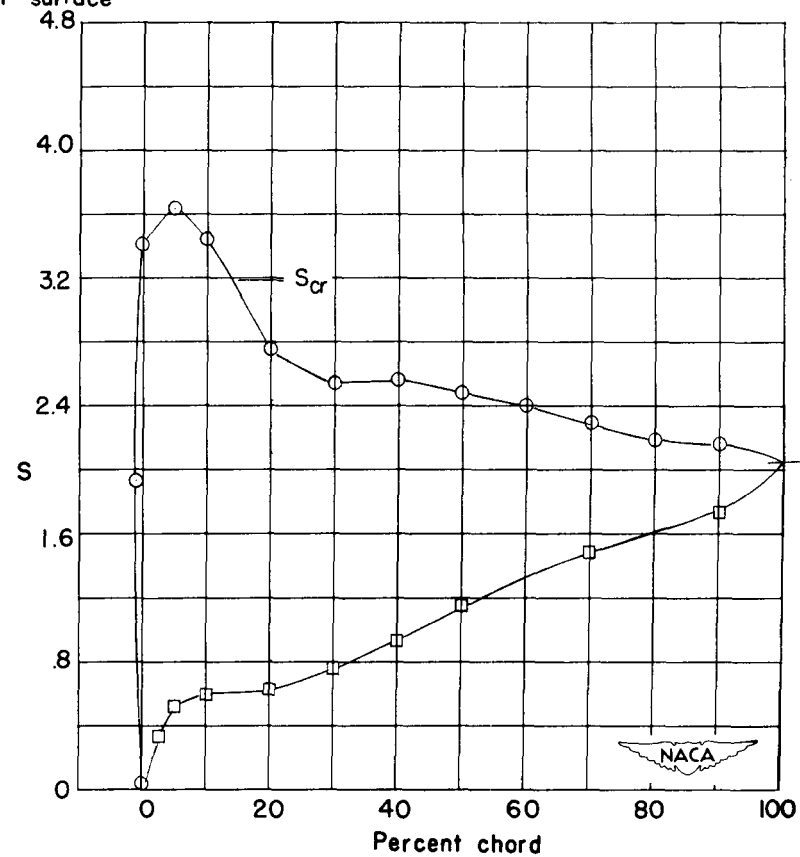


(b)  $M_1 = .499$ ;  $M_2 = .655$ ;  $C_{w1} = .0175$ ;  $\theta = 71.0^\circ$ .

Figure 37.- High-speed pressure distributions for cascade combinations  
 $\beta_1 = 30^\circ$ ,  $\alpha_1 = 50.4^\circ$ ,  $\theta_c = 80^\circ$ ,  $\sigma = 1.8$ .

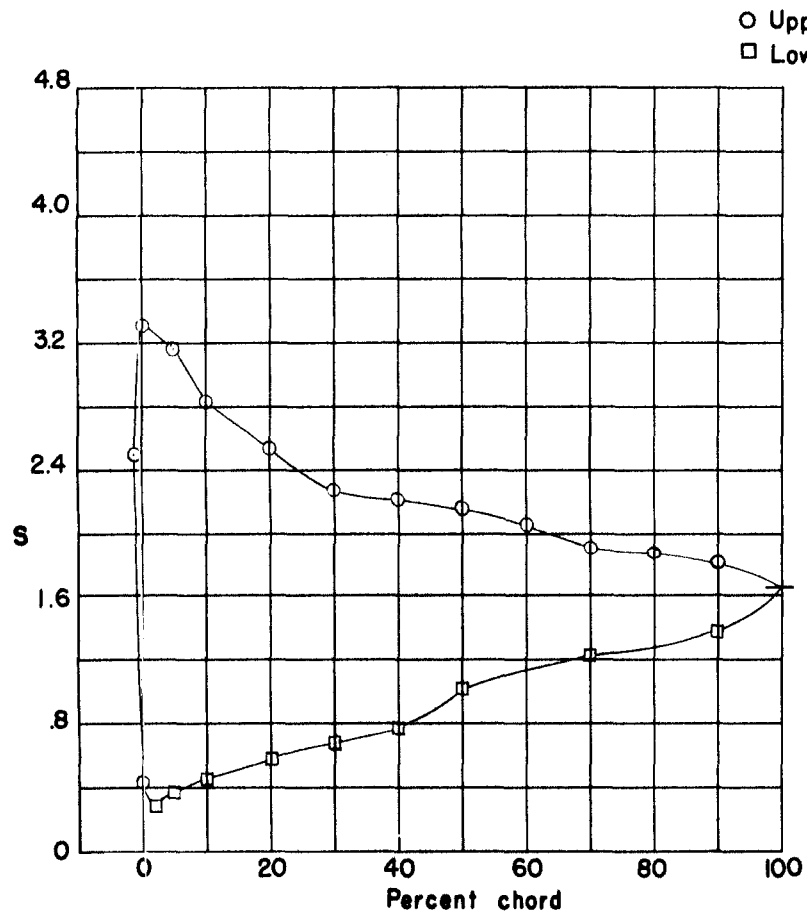


(a)  $M_1 = .265$ ;  $M_2 = .330$ ;  $C_{w1} = .0153$ ;  $\theta = 73.4^\circ$ .

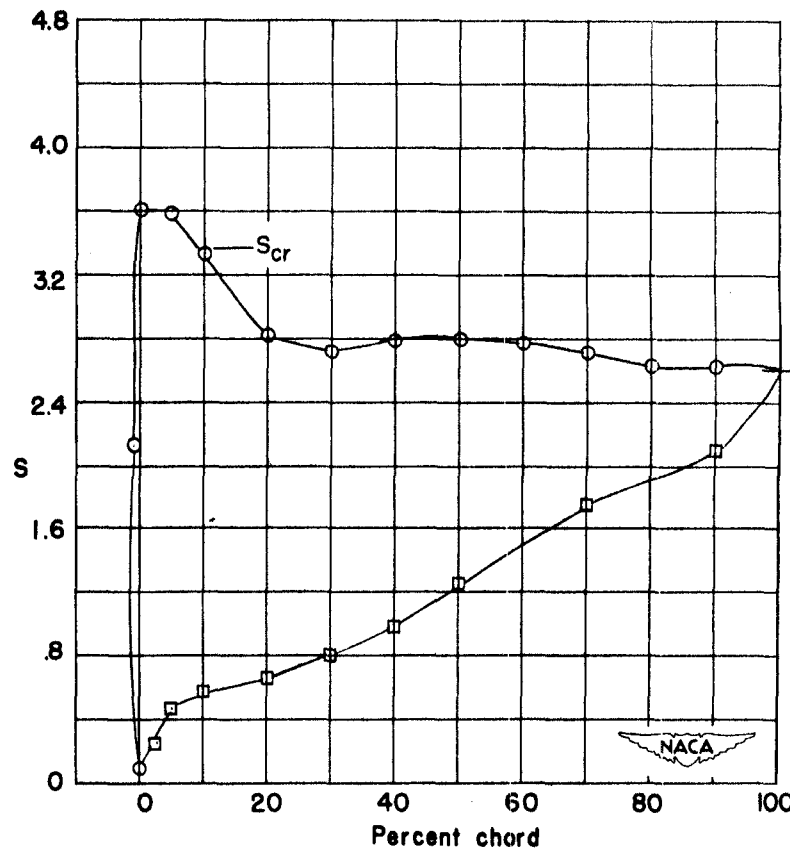


(b)  $M_1 = .500$ ;  $M_2 = .732$ ;  $C_{w1} = .0180$ ;  $\theta = 73.8^\circ$

Figure 38.- High-speed pressure distributions for cascade combinations  
 $\beta_1 = 30^\circ$ ,  $\alpha_1 = 53.4^\circ$ ,  $\theta_c = 80^\circ$ ,  $\sigma = 1.8$ .

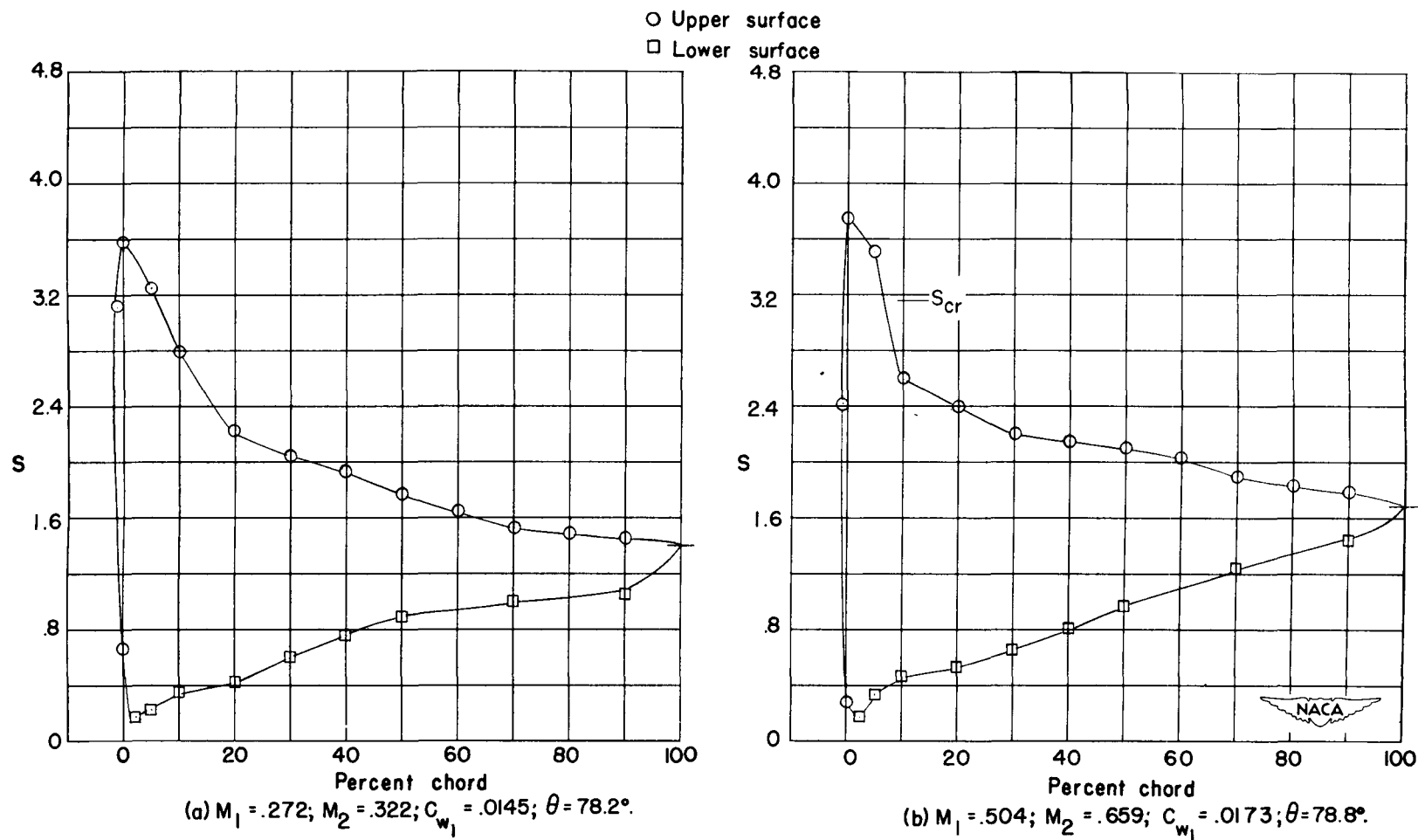


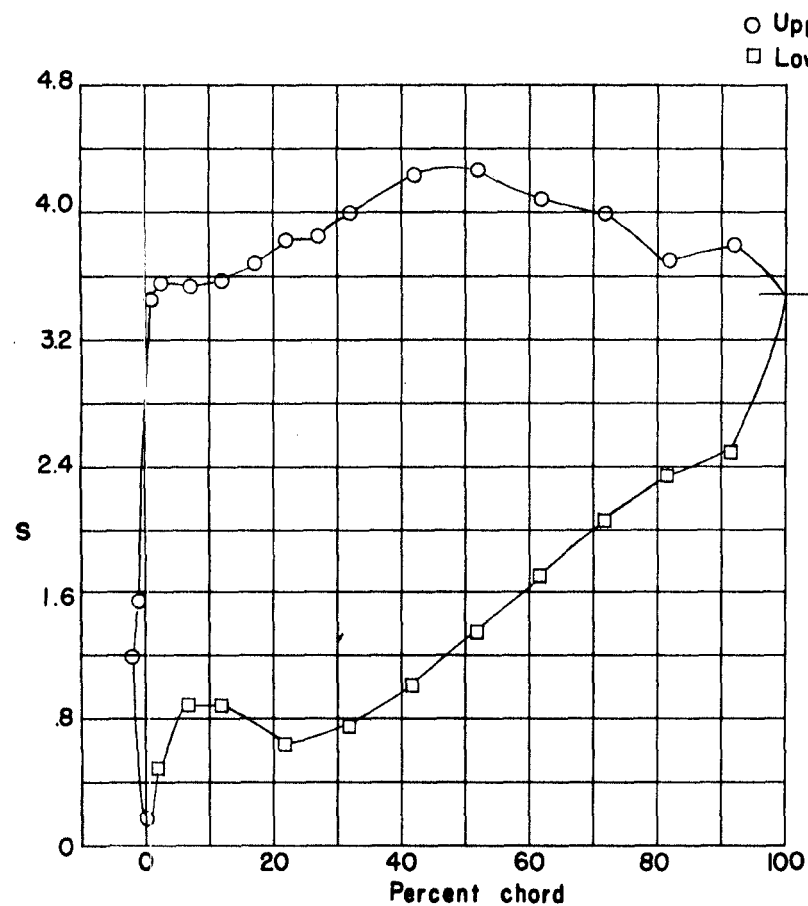
(a)  $M_1 = .180$ ;  $M_2 = .233$ ;  $C_{w1} = .0157$ ;  $\theta = 77.2^\circ$ .



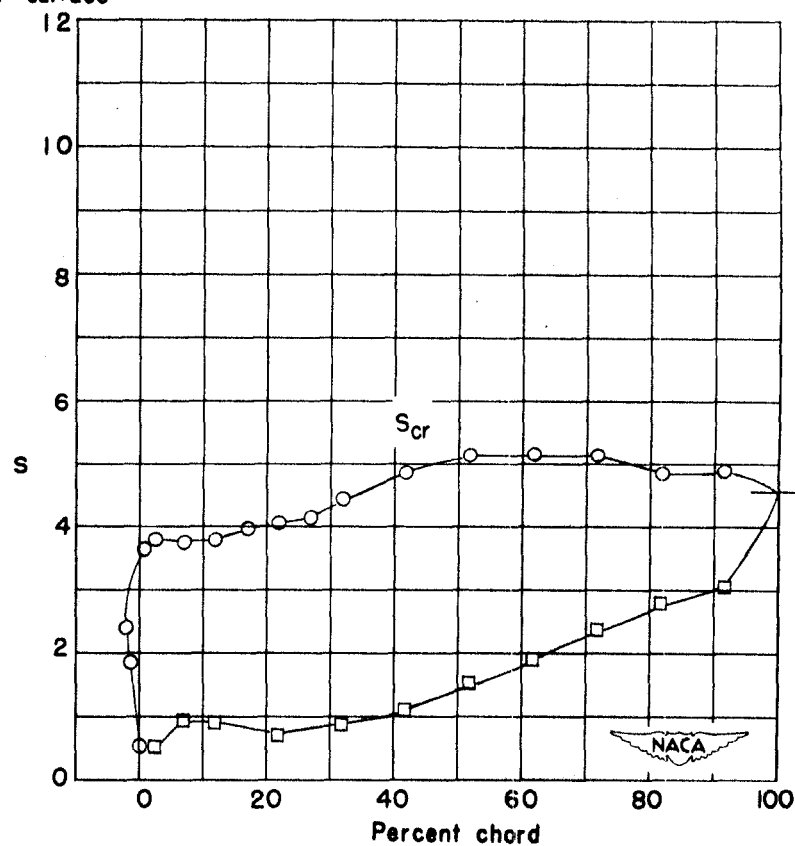
(b)  $M_1 = .485$ ;  $M_2 = .832$ ;  $C_{w1} = .0178$ ;  $\theta = 77.3^\circ$ .

Figure 39.- High-speed pressure distributions for cascade combinations  
 $\beta_1 = 30^\circ$ ,  $\alpha_1 = 56.4^\circ$ ,  $\theta_c = 80^\circ$ ,  $\sigma = 1.8$ .





(a)  $M_1 = .270$ ;  $M_2 = .509$ ;  $C_{w1} = .0156$ ;  $\theta = 83.2^\circ$ .



(b)  $M_1 = .364$ ;  $M_2 = .797$ ;  $C_{w1} = .0202$ ;  $\theta = 82.2^\circ$ .

Figure 41.- High-speed pressure distributions for cascade combinations

$$\beta_1 = 25^\circ, \quad \alpha_1 = 56.1^\circ, \quad \theta_c = 95^\circ, \quad \sigma = 1.8.$$

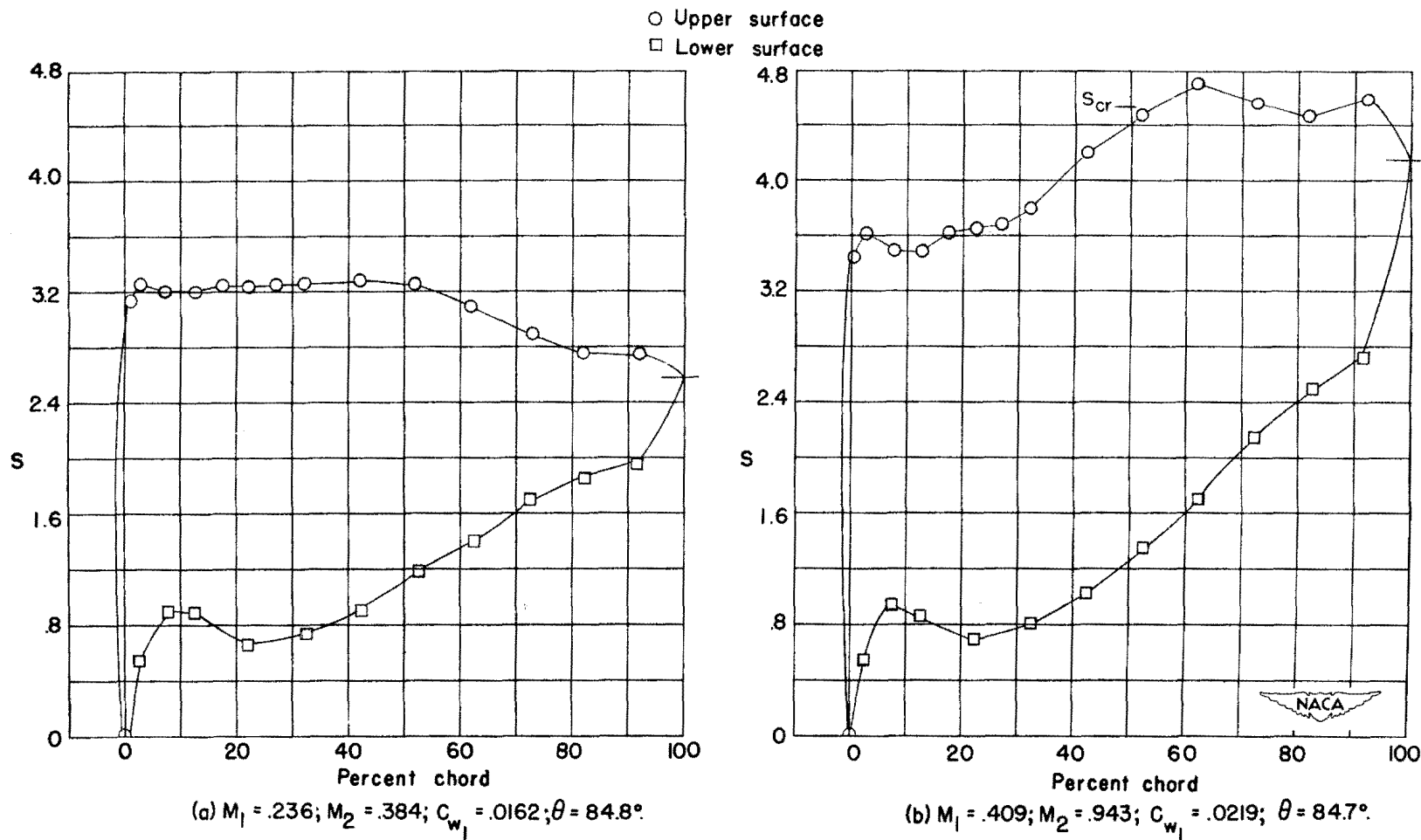
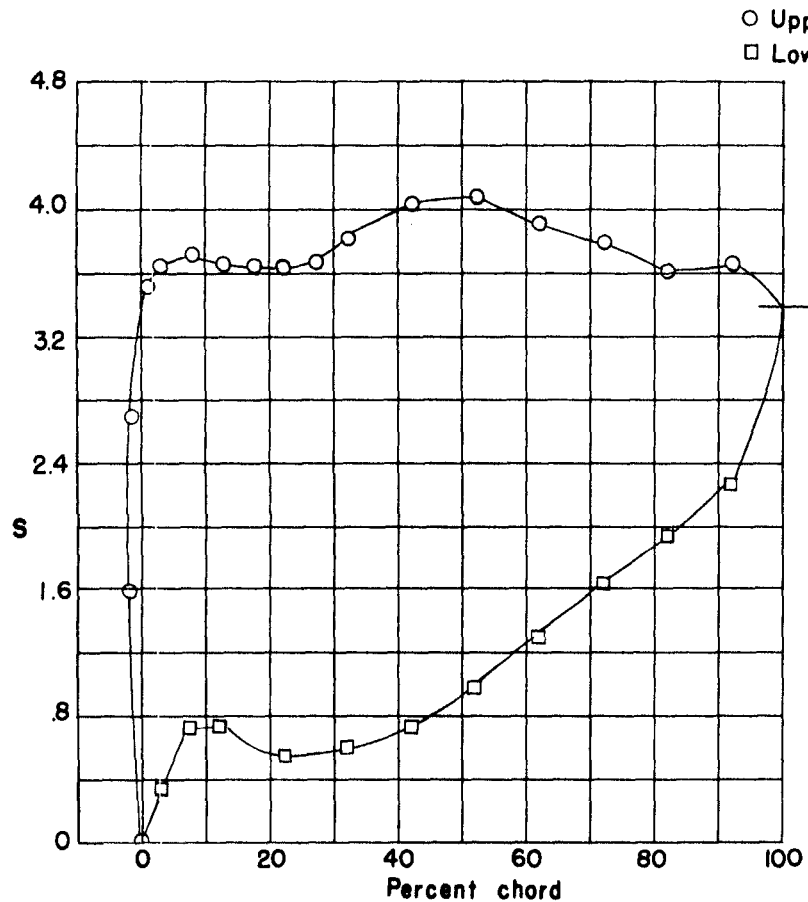
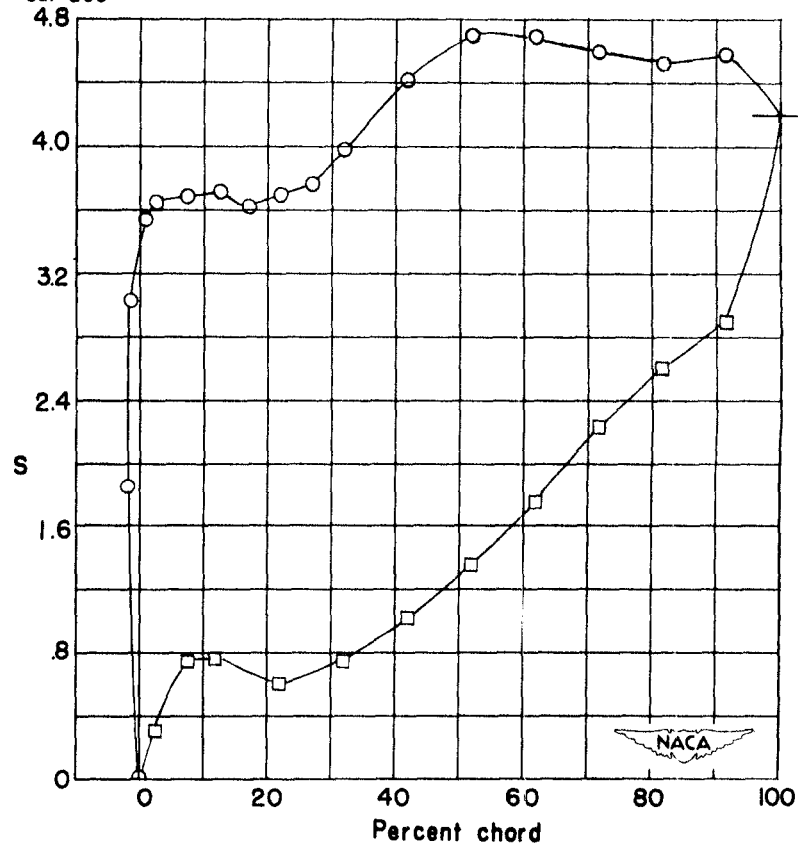


Figure 42.- High-speed pressure distributions for cascade combinations  
 $\beta_1 = 30^\circ, \alpha_1 = 58.1^\circ, \theta_c = 95^\circ, \sigma = 1.8.$



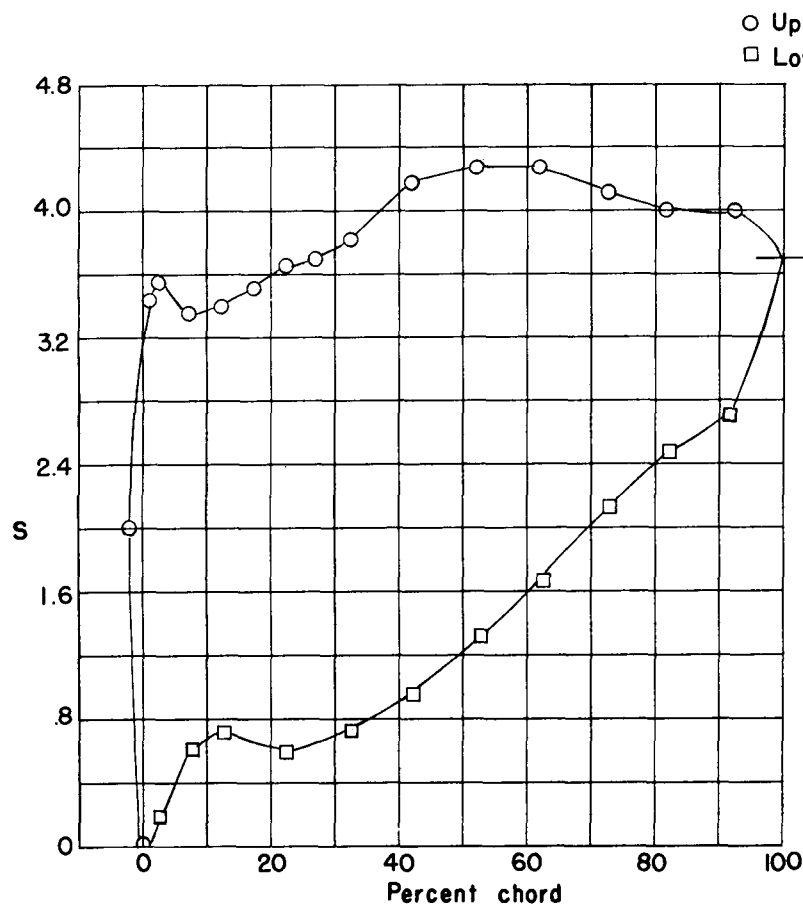
(a)  $M_1 = .276$ ;  $M_2 = .526$ ;  $C_{w1} = .0187$ ;  $\theta = 87.7^\circ$ .



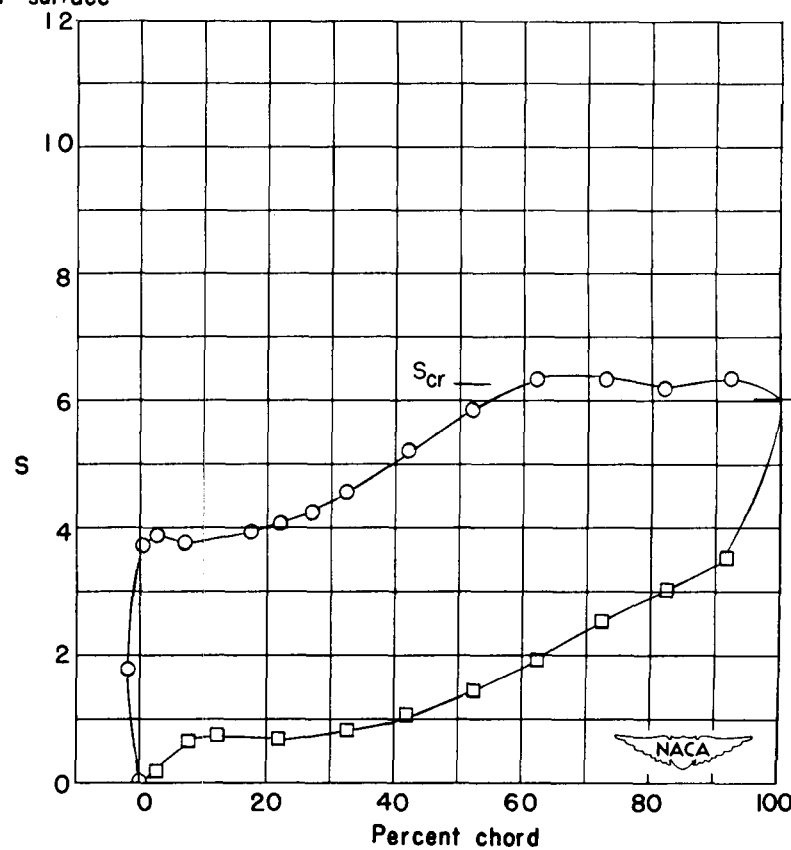
(b)  $M_1 = .362$ ;  $M_2 = .813$ ;  $C_{w1} = .0212$ ;  $\theta = 87.8^\circ$ .

Figure 43.- High-speed pressure distributions for cascade combinations  
 $\beta_1 = 30^\circ$ ,  $\alpha_1 = 61.1^\circ$ ,  $\theta_c = 95^\circ$ ,  $\sigma = 1.8$ .



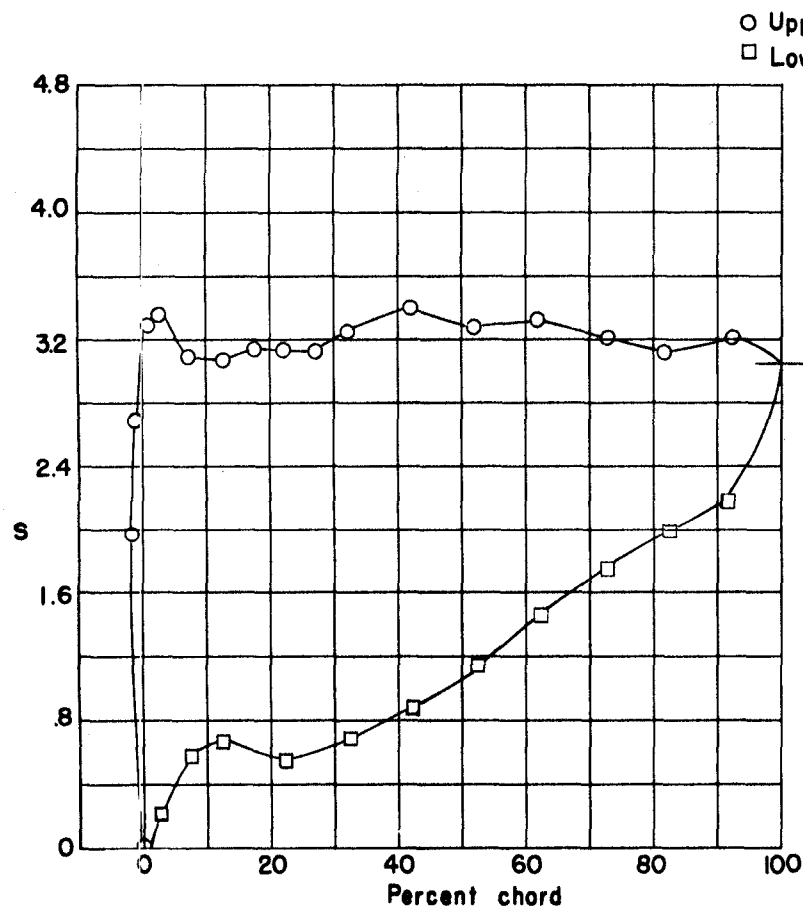


(a)  $M_1 = .235$ ;  $M_2 = .468$ ;  $C_{w1} = .0198$ ;  $\theta = 90.6^\circ$ .

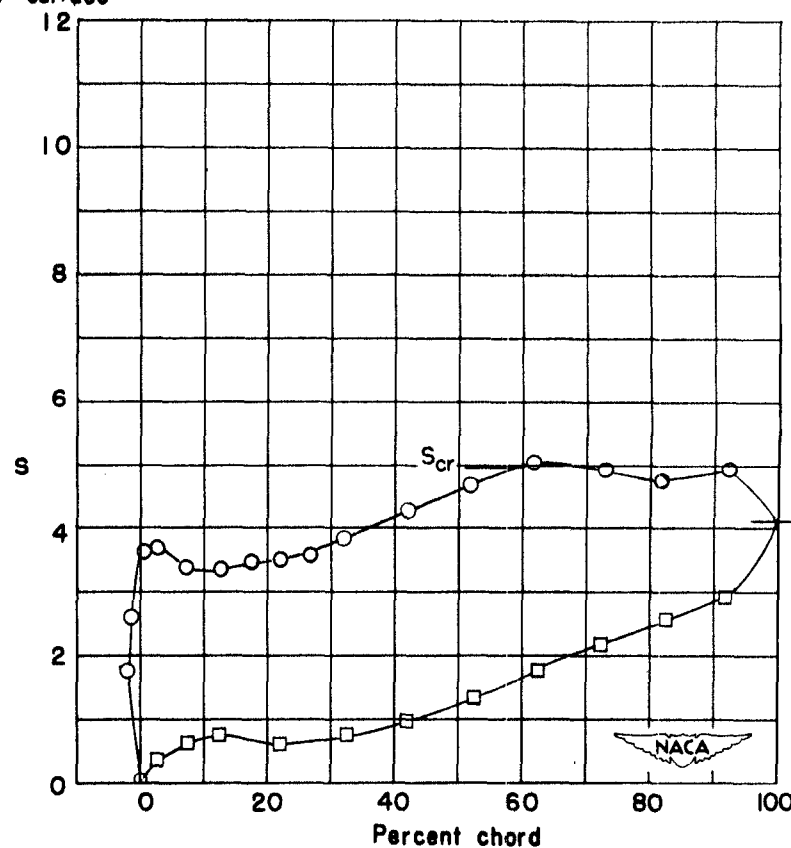


(b)  $M_1 = .341$ ;  $M_2 = .967$ ;  $C_{w1} = .0295$ ;  $\theta = 90.4^\circ$ .

Figure 44.- High-speed pressure distributions for cascade combinations  
 $\beta_1 = 30^\circ$ ,  $\alpha_1 = 64.1^\circ$ ,  $\theta_c = 95^\circ$ ,  $\sigma = 1.8$ .



(a)  $M_1 = .284$ ;  $M_2 = .512$ ;  $C_{w_1} = .0186$ ;  $\theta = 94.3$ .



(b)  $M_1 = .387$ ;  $M_2 = .902$ ;  $C_{w_1} = .0225$ ;  $\theta = 92.9^\circ$ .

Figure 45.- High-speed pressure distributions for cascade combinations

$$\beta_1 = 35^\circ, \quad \alpha_1 = 66.1^\circ, \quad \theta_c = 95^\circ, \quad \sigma = 1.8.$$

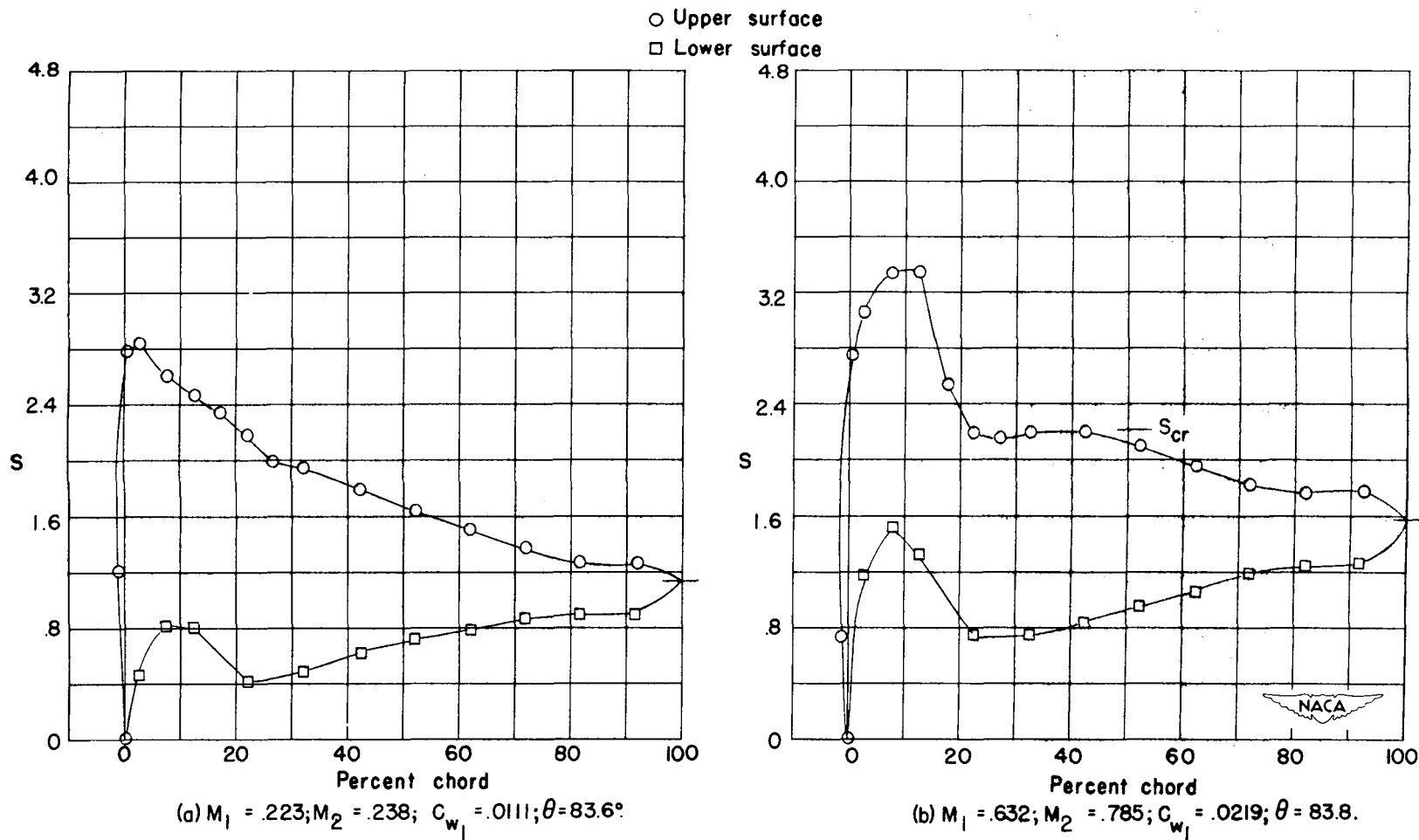


Figure 46.- High-speed pressure distributions for cascade combinations

$$\beta_1 = 40^\circ, \quad \alpha_1 = 56.1^\circ, \quad \theta_c = 95^\circ, \quad \sigma = 1.8.$$

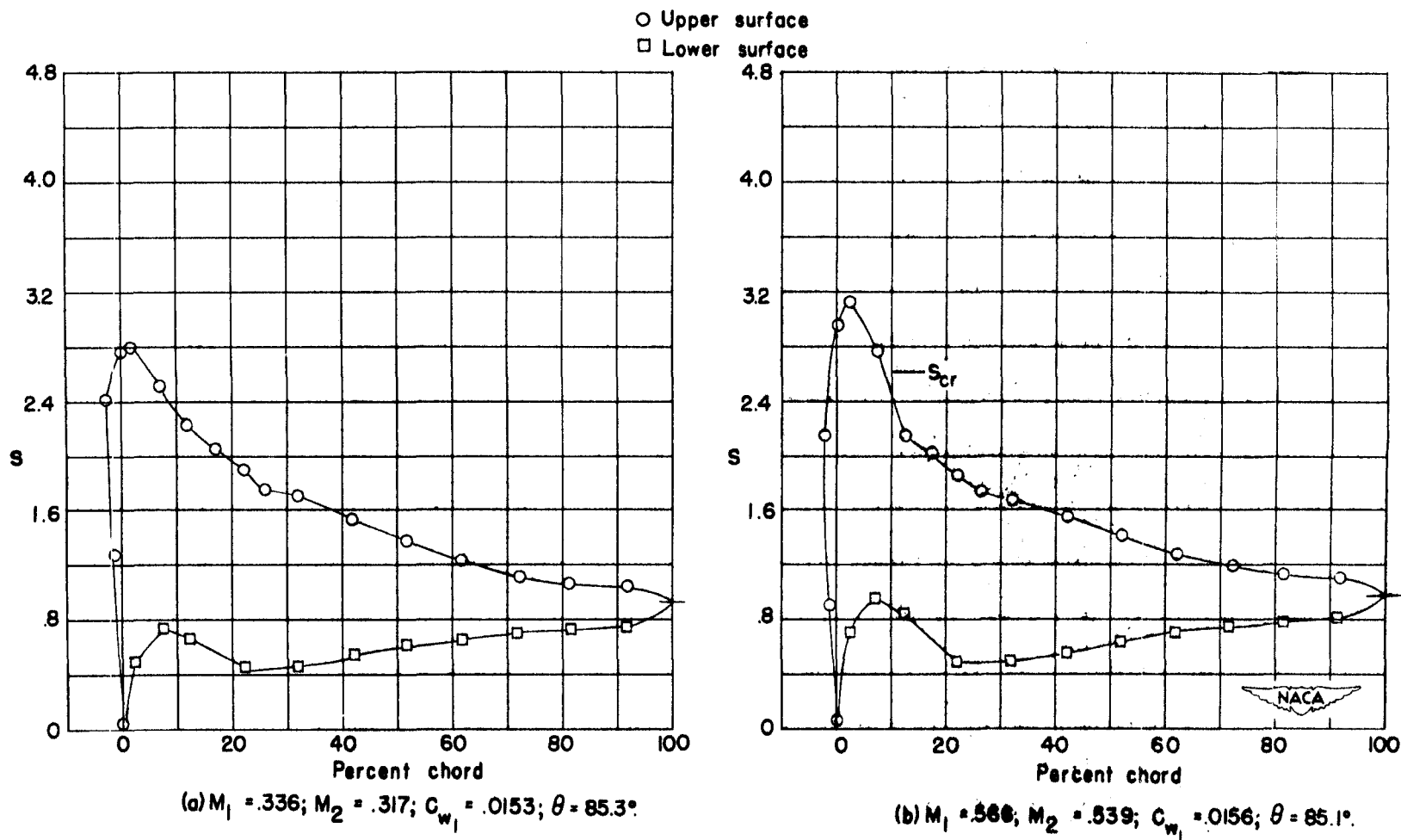
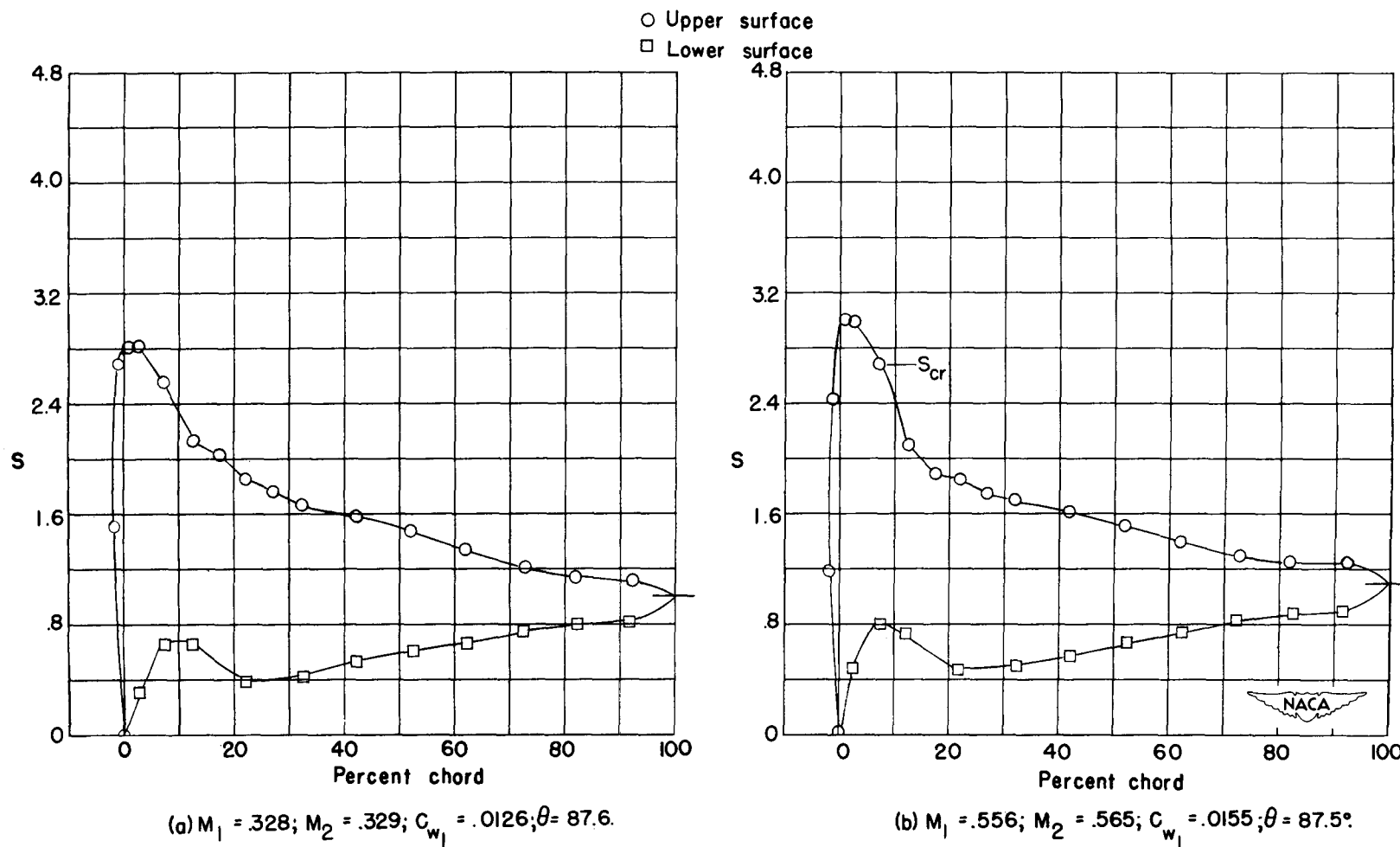
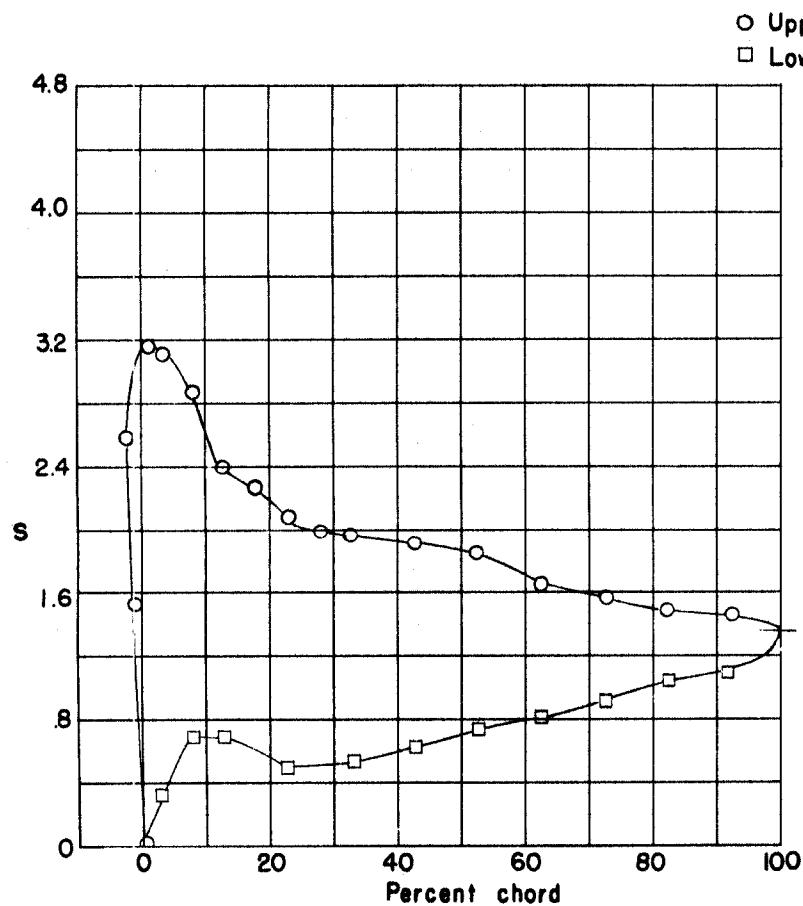
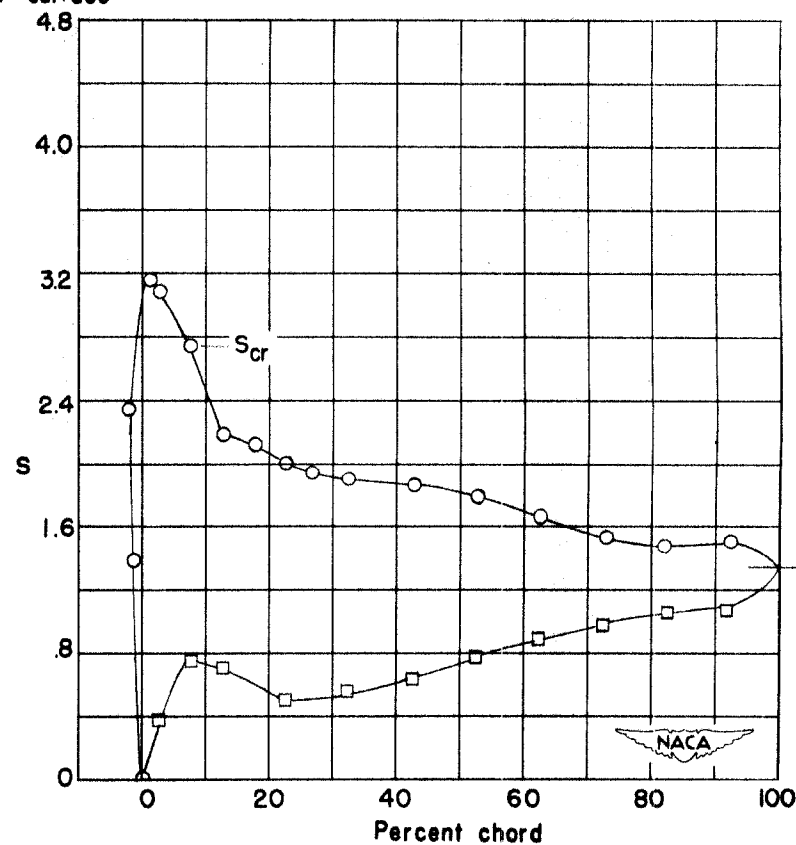


Figure 47.- High-speed pressure distributions for cascade combinations  
 $\beta_1 = 45^\circ$ ,  $\alpha_1 = 58.1^\circ$ ,  $\theta_c = 95^\circ$ ,  $\sigma = 1.8$ .





(a)  $M_1 = .412$ ;  $M_2 = .459$ ;  $C_{w1} = .0146$ ;  $\theta = 90.8^\circ$ .



(b)  $M_1 = .549$ ;  $M_2 = .629$ ;  $C_{w1} = .0193$ ;  $\theta = 91.0^\circ$ .

Figure 49.- High-speed pressure distributions for cascade combinations

$$\beta_1 = 45^\circ, \alpha_1 = 64.1^\circ, \theta_c = 95^\circ, \sigma = 1.8.$$

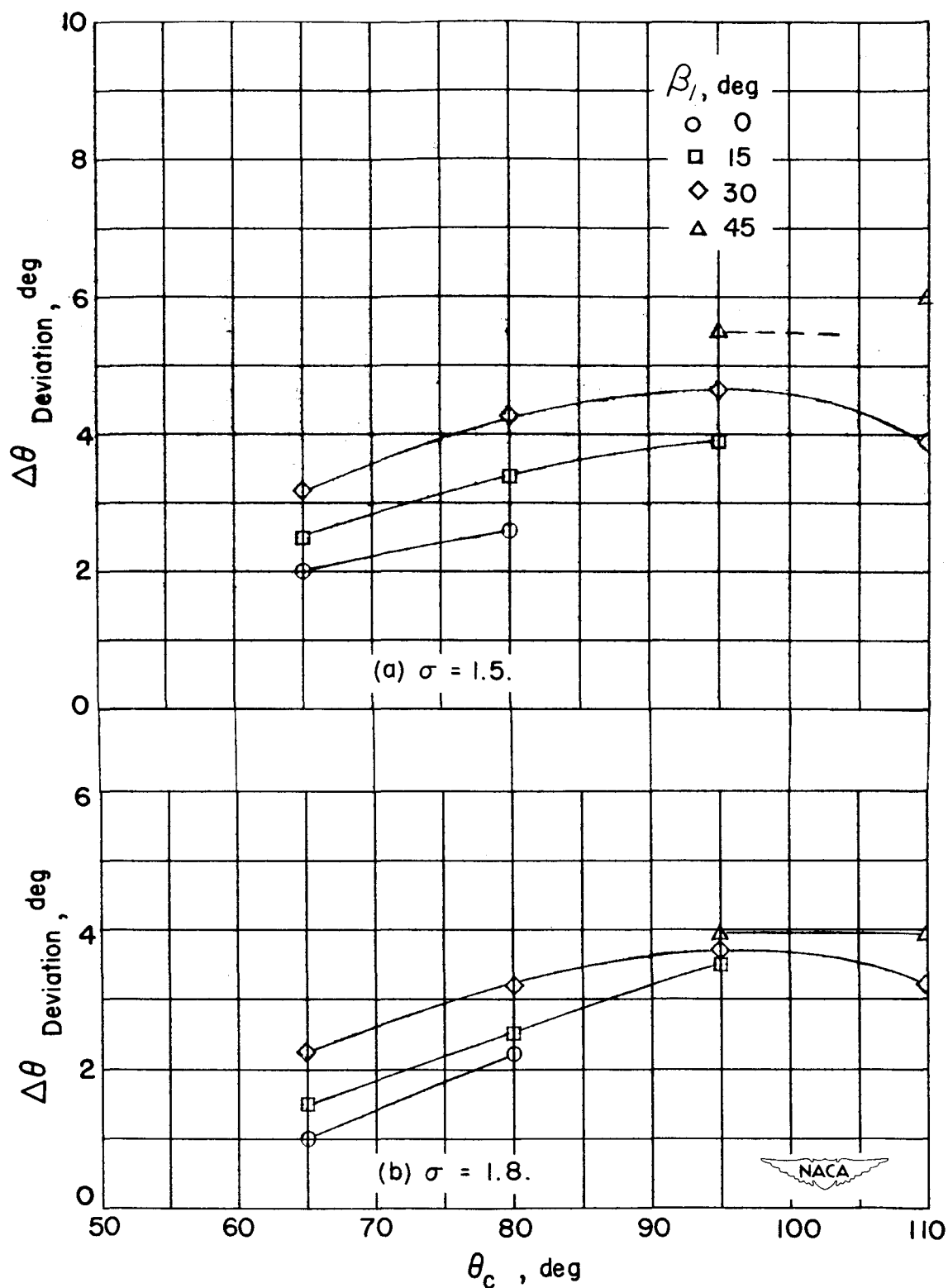


Figure 50.- Deviation of the leaving-flow direction from the mean-line direction at 95-percent-chord station for blade camber.

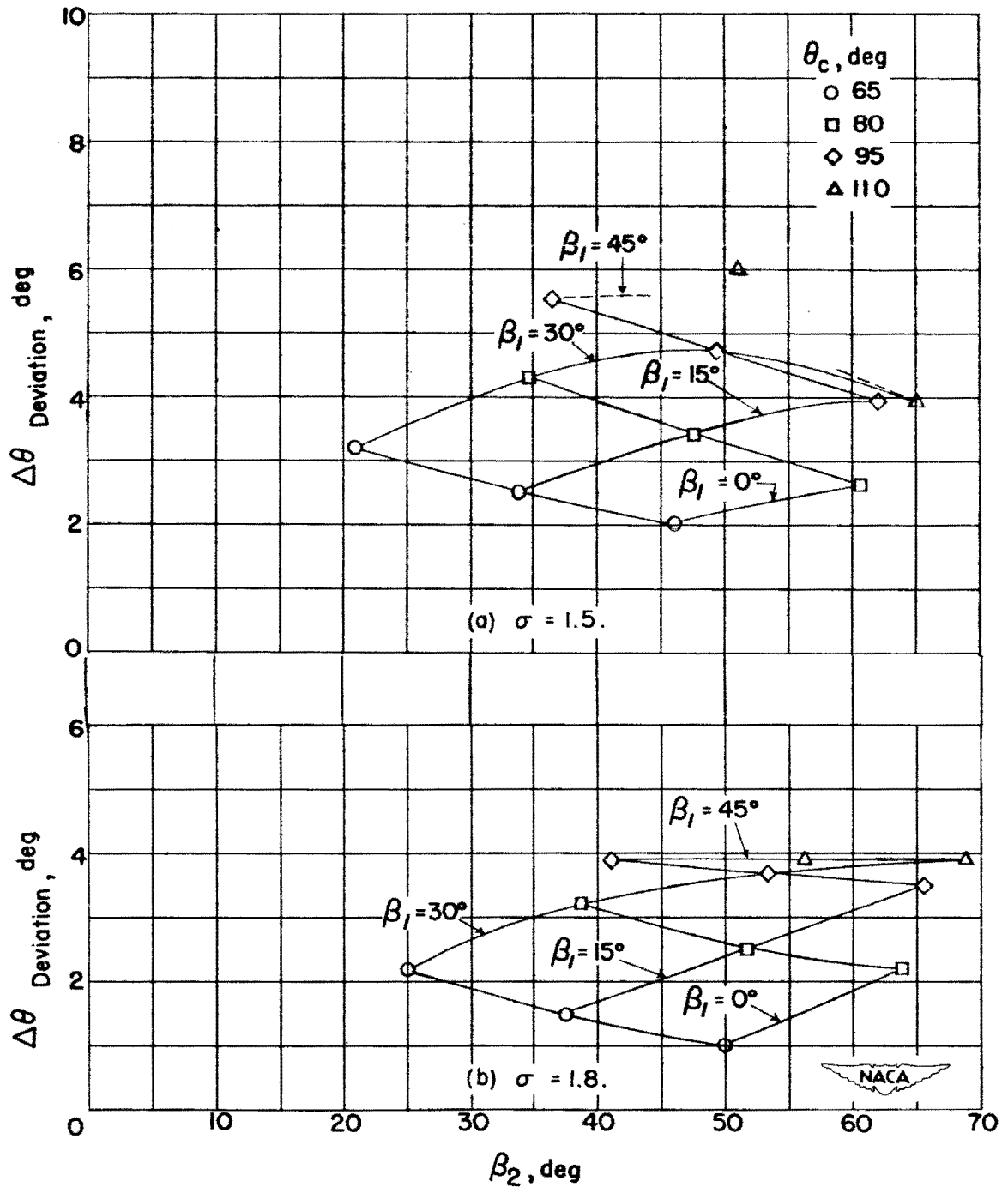


Figure 51.- Deviation of the leaving-flow direction from the mean-line direction at 95-percent-chord station for leaving-flow angles.



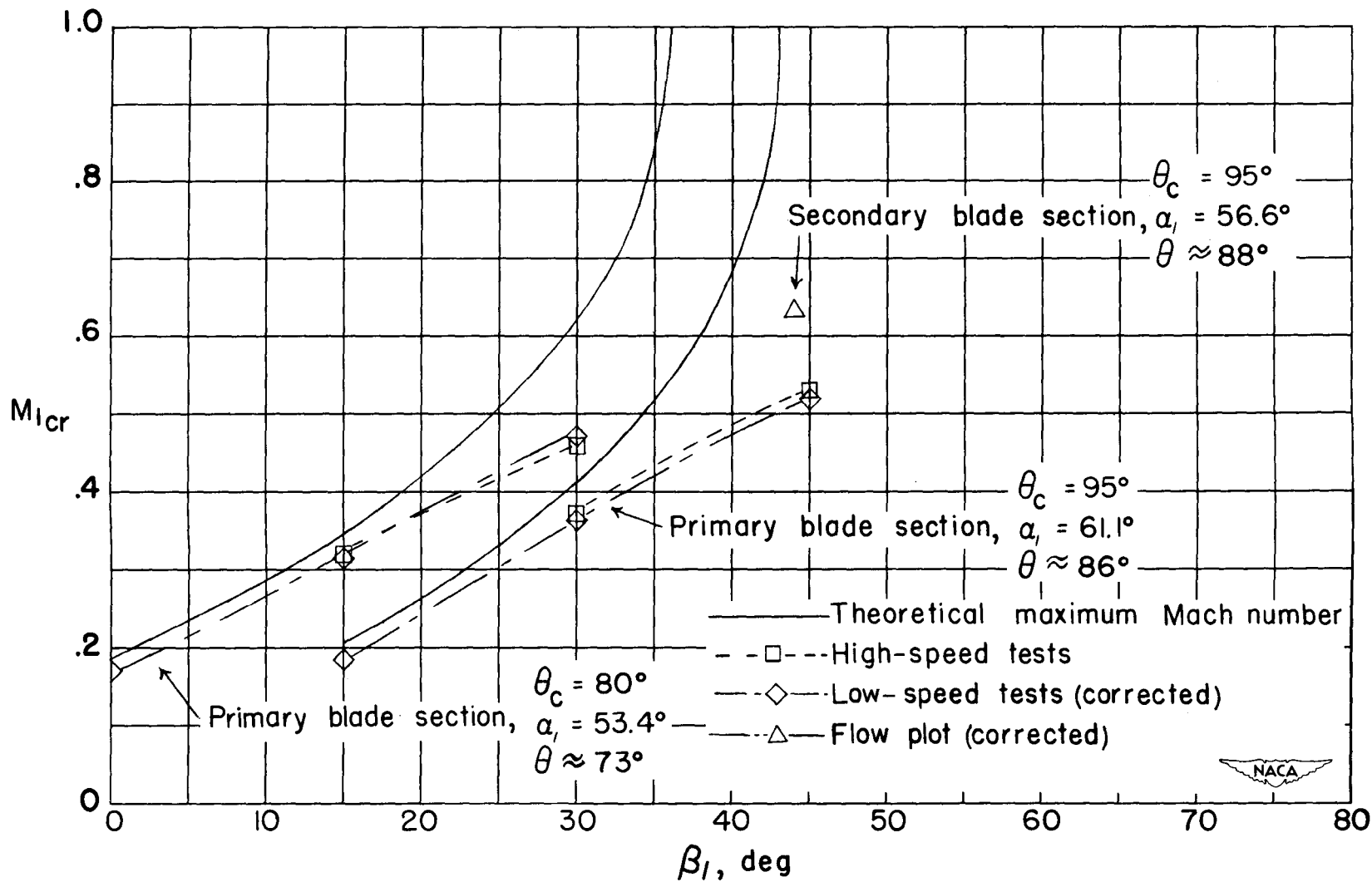


Figure 52.- Critical Mach numbers for blade sections.  $\sigma = 1.8$ .

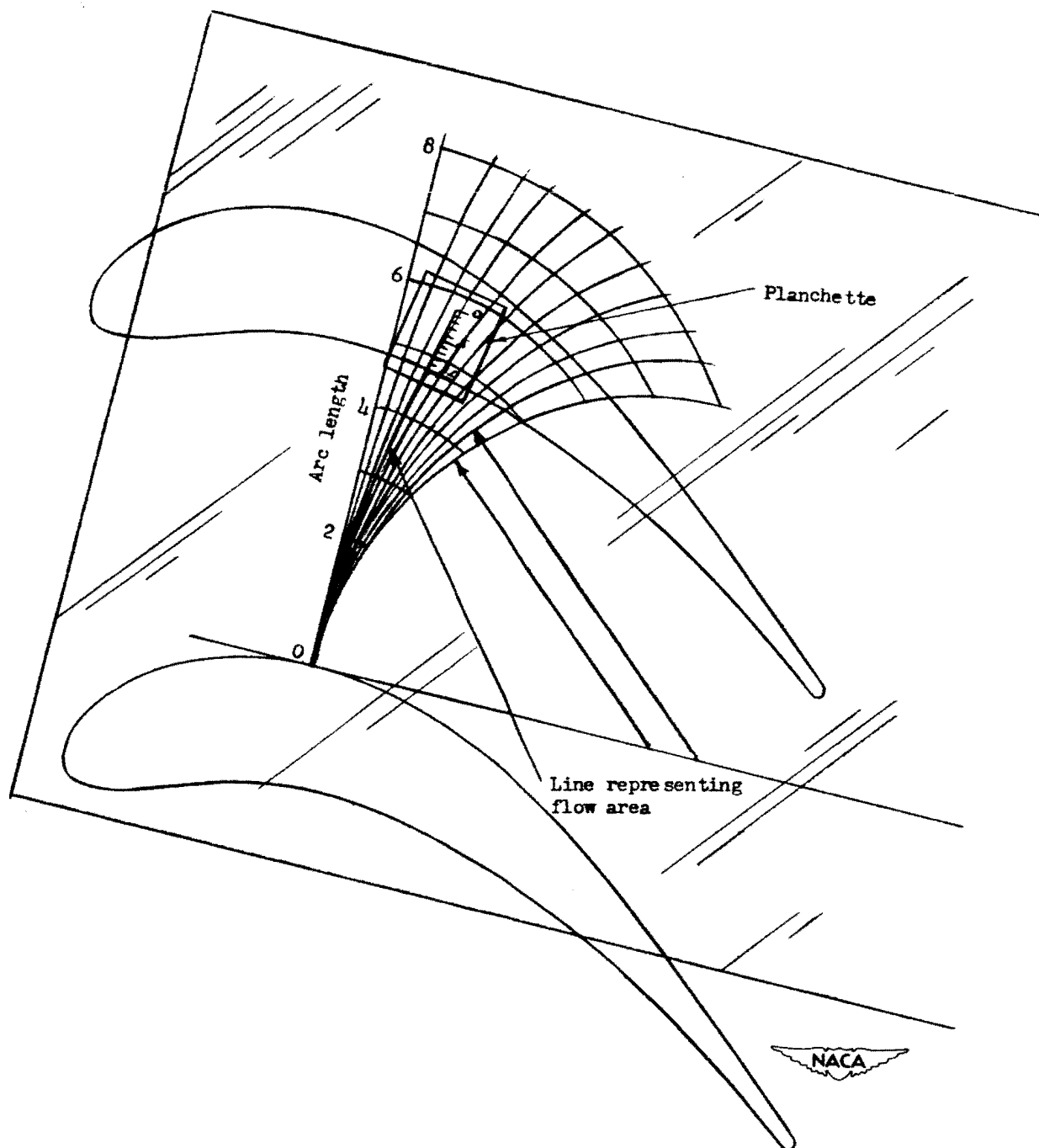


Figure 53.- Measurement of flow-passage area for compressibility corrections to low-speed tests.

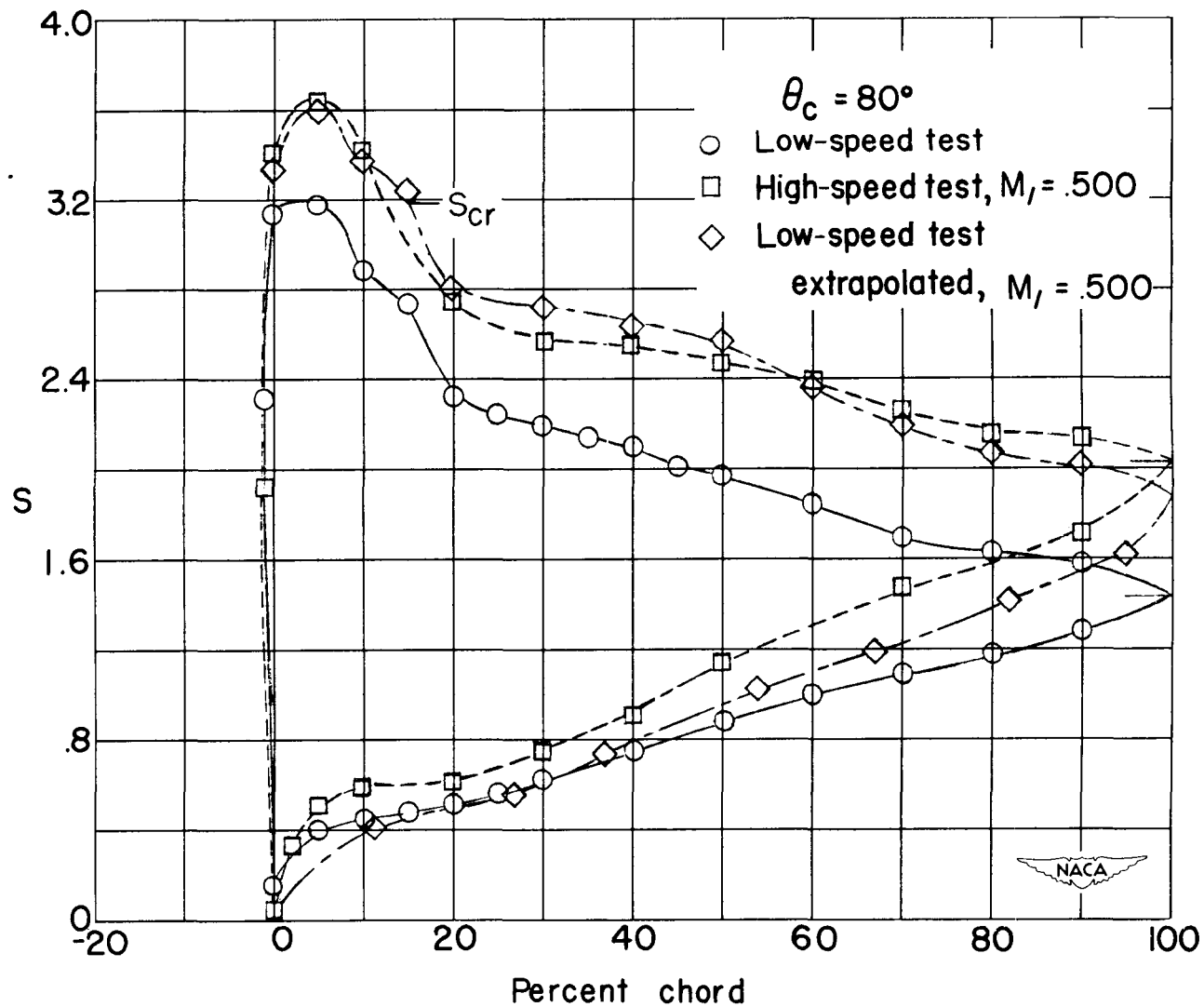


Figure 54.- Comparison of high-speed-test pressure distribution and pressure distribution extrapolated from low-speed blade test.

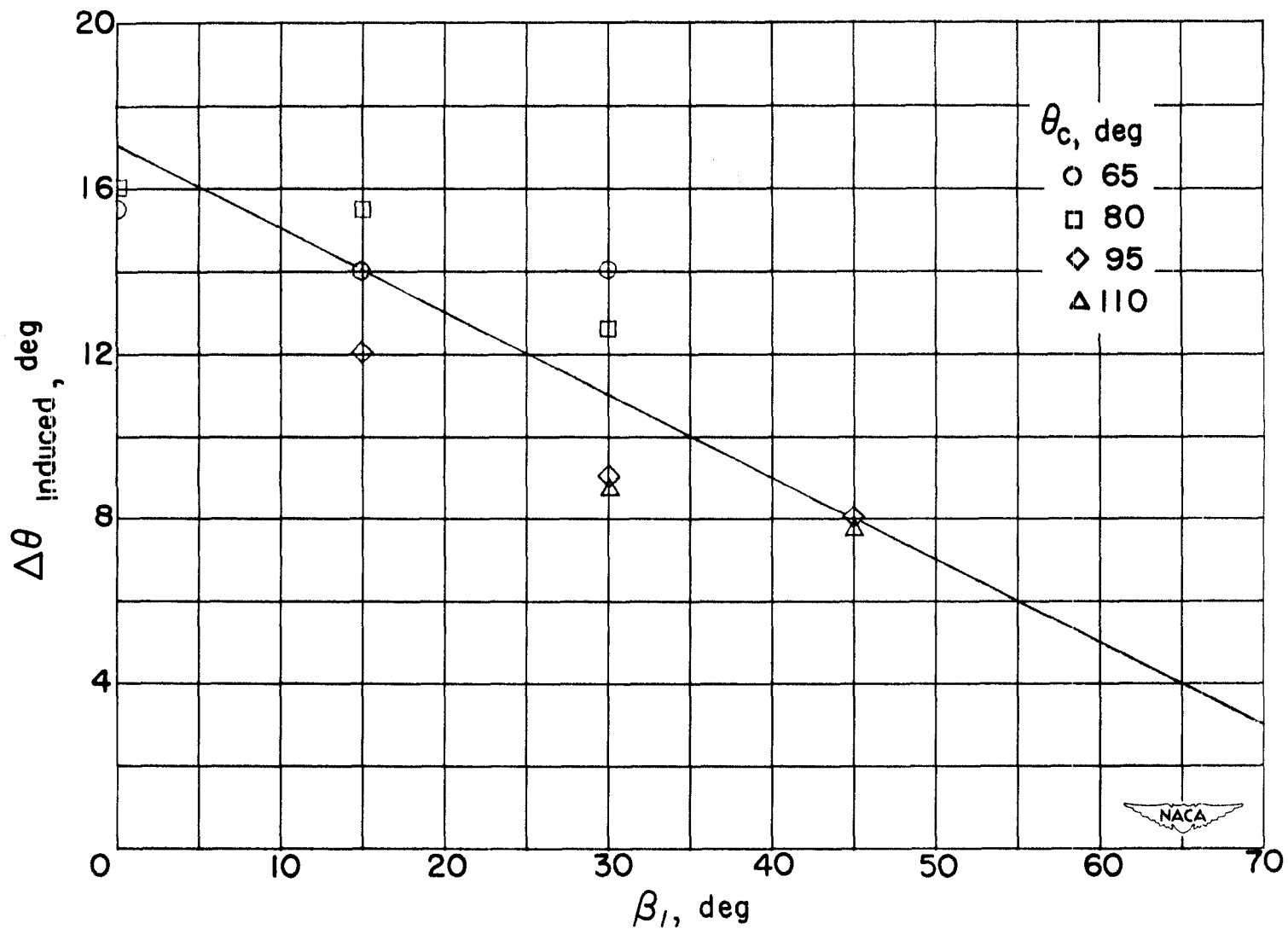


Figure 55.- Measured values of induced angle at low speed and mean induced angle for solidity of 1.5.

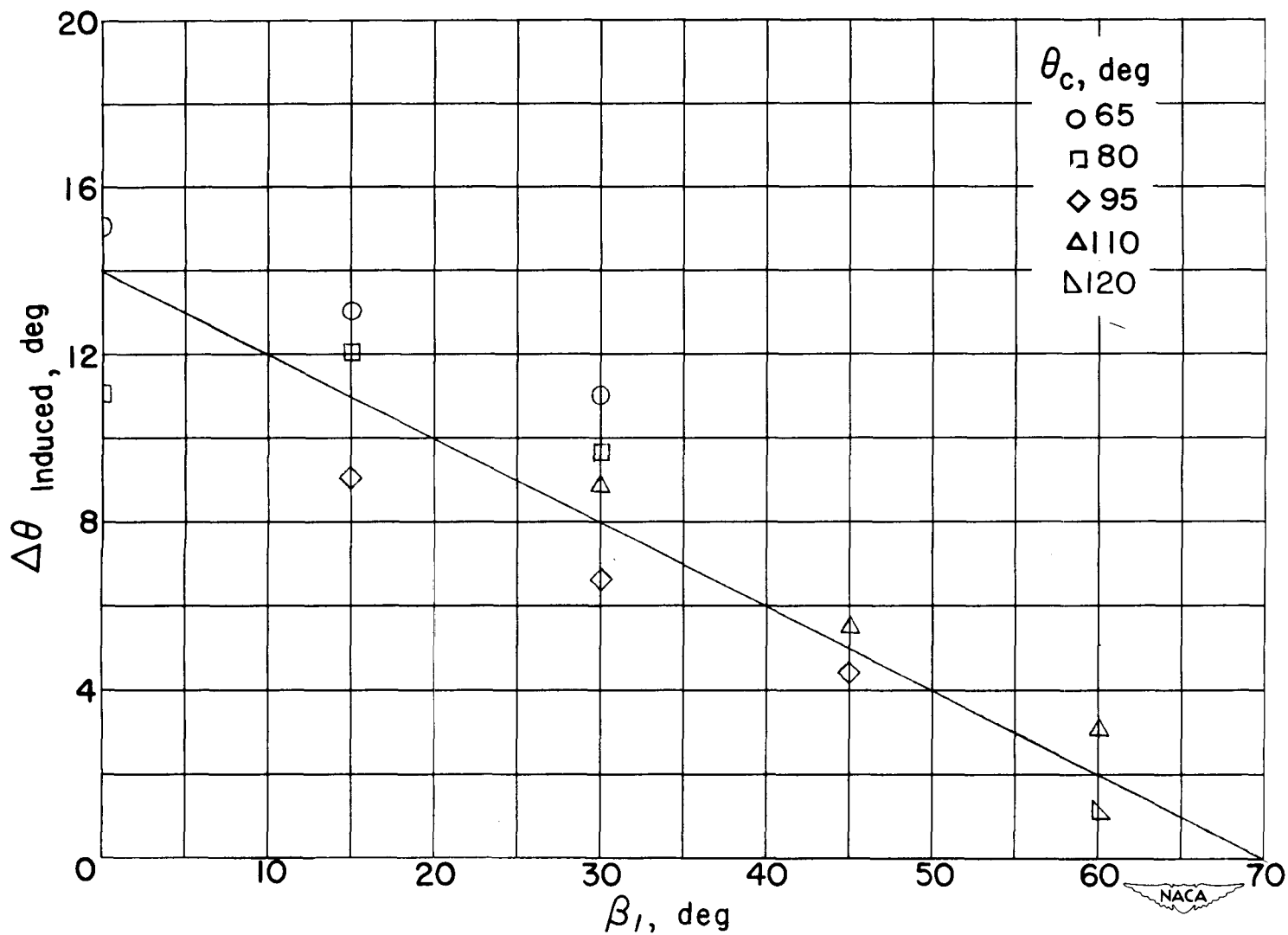


Figure 56.- Measured values of induced angle at low speed and mean induced angle for solidity of 1.8.